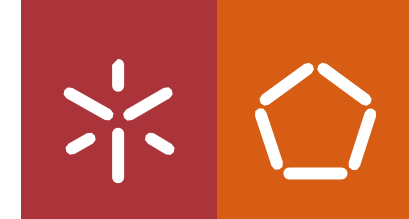


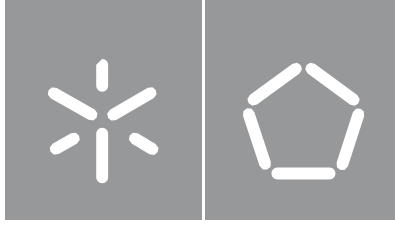


Catarina Rafaela da Silva Rebelo

**Development of antibacterial
surfaces by deposition of Zinc
nanoparticles by magnetron
sputtering on Ta₂O₅
nanostructured surfaces**

Universidade do Minho
Escola de Engenharia





Universidade do Minho
Escola de Engenharia

Catarina Rafaela da Silva Rebelo

**Development of antibacterial
surfaces by deposition of Zinc
nanoparticles by magnetron
sputtering on Ta₂O₅ nanostructured
surfaces**

Dissertação de Mestrado
Mestrado Integrado em Engenharia
de Materiais

Trabalho realizado sob a orientação da
**Professora Doutora Sandra Maria Fernandes
Carvalho**
e da
Doutora Luísa Isabel Serra da Glória Fialho

DIREITOS DE AUTOR E CONDIÇÕES DE UTILIZAÇÃO POR TERCEIROS

Este é um trabalho académico que pode ser utilizado por terceiros desde que respeitadas as regras e boas práticas internacionalmente aceites, no que concerne aos direitos de autor e direitos conexos.

Assim, o presente trabalho pode ser utilizado nos termos previstos na licença abaixo indicada.

Caso o utilizador necessite de permissão para poder fazer um uso do trabalho em condições não previstas no licenciamento indicado, deverá contactar o autor, através do RepositóriUM da Universidade do Minho.

Licença concedida aos utilizadores deste trabalho



Atribuição-NãoComercial-SemDerivações

CC BY-NC-ND

<https://creativecommons.org/licenses/by-nc-nd/4.0/>

STATEMENT OF INTEGRITY

I hereby declare having conducted this academic work with integrity. I confirm that I have not used plagiarism or any form of undue use of information or falsification of results along the process leading to its elaboration.

I further declare that I have fully acknowledged the Code of Ethical Conduct of the University of Minho.

Acknowledgements

Porque sozinha nunca teria conseguido chegar ao final deste projeto, quero apresentar os meus mais sinceros agradecimentos a todos os que contribuíram para a realização deste trabalho.

Em primeiro lugar, quero agradecer à minha orientadora, Professora Sandra Carvalho, por me ter dado a oportunidade de realizar este trabalho. Agradeço pela confiança que depositou em mim e nas minhas capacidades, pela disponibilidade, pela orientação, pelos conhecimentos científicos e ainda pela compreensão, pelos conselhos e pelo apoio nesta jornada.

Quero agradecer à Luísa Fialho, que foi uma incrível coorientadora. Obrigada por toda a ajuda, partilha de conhecimento e paciência. Obrigada por toda a disponibilidade, mesmo quando isso implicava ir à universidade aos sábados, domingos e feriados. Agradeço pela orientação, mas, sobretudo, pela amizade, pelas boas conversas e pelo apoio nos momentos de maior pressão.

Agradeço também à Cristiana Alves pela ajuda, disponibilidade e partilha de conhecimento em diversas etapas da realização deste projeto, mas também pelas nossas boas conversas aleatórias.

Gostaria de agradecer a todos os elementos do grupo de trabalho na universidade do Minho, Mariana, Edgar, Maria José, Isabel, Kira e José David. Ao José David deixo um agradecimento especial pela paciência e toda a ajuda fundamental sempre que o assunto era corrosão.

Como não podia deixar de ser, quero agradecer aos meus amigos Aless, Rita, Pedro, Kikó, Carina, Cláudio, Diogo e Mariana, que conheci na universidade e que depressa se tornaram família. Um obrigada não chega para agradecer o carinho, as memórias e todos os momentos bons que passamos juntos. À minha amiga de todas as horas, Vieira, agradeço pela amizade incondicional, pelo carinho e pela força que sempre me deu ao longo de tantos anos de amizade.

Por fim, como não poderia deixar de ser, agradeço à minha família do fundo do meu coração. Aos meus avós, obrigada por serem um exemplo de força e perseverança e por me mostrarem todos os dias que a vida é bonita ao lado daqueles de quem se gosta. Ao meu irmão, agradeço por ser o meu melhor amigo, por ter sempre uma palavra de apoio e por me ensinar que nem tudo nesta vida precisa de ser levado a sério. Aos meus pais agradeço por serem os grandes impulsionadores de todos os meus sonhos, por todos os conselhos, pela compreensão, pelo apoio e pelo amor incondicional. Obrigada por me terem dado asas para voar!

A todos, muito obrigada!

Resumo

Atualmente, as principais causas para a rejeição de implantes dentários são a lenta osteointegração e consequente adesão e crescimento bacteriano, o que pode levar ao aparecimento de doença peri-implantar. A osteointegração e a inibição da adesão bacteriana podem ser melhoradas através da modificação das propriedades da superfície do implante.

Esta dissertação foca-se numa primeira fase na modificação de superfícies metálicas de tântalo (Ta), através de oxidação por plasma eletrolítico (PEO). A modificação por PEO, pretende promover a bioatividade da superfície e acelerar a osteointegração através da mimetização da morfologia e química do osso humano, com a formação de estruturas micro/nanoporosas e incorporação de elementos osteocondutores (cálcio (Ca) e o fósforo (P)). Numa segunda fase, sobre esta superfície bioativa, nanopartículas (NPs) de zinco (Zn), com e sem camada de carbono (C), são depositadas por pulverização catódica em magnetrão para dotar esta superfície com atividade antimicrobiana.

Foram testadas diferentes quantidades de NPs depositadas nas superfícies de Ta oxidadas por PEO. Aumentando o tempo de deposição e/ou diminuindo a pressão de trabalho, foi possível depositar maior quantidade de NPs de Zn com diferentes morfologias. A libertação de iões zinco aumentou com o aumento da quantidade de NPs e diminuiu com a deposição da camada de carbono. As superfícies otimizadas, a com maior e a com menor quantidade de NPs, foram estudadas quanto à atividade antimicrobiana e resistência à corrosão. A presença de NPs de Zn teve grande impacto na melhoria da atividade antimicrobiana, com a maior quantidade de NPs a mostrar maior inibição do crescimento de *C. Albicans* do que a superfície porosa de Ta₂O₅. Os resultados de corrosão revelaram que a formação de Ta₂O₅ promovida pela técnica de PEO conduziu à melhoria do comportamento à corrosão, em comparação com o Ta não modificado. Em contrapartida a incorporação das NPs metálicas de Zn promoveu uma degradação da resistência à corrosão das amostras, que foi melhorando com o aumento do tempo de imersão. Estes resultados demonstraram que a incorporação de NPs de Zn nas superfícies porosas de Ta₂O₅ inibiu eficazmente o crescimento microbiano. Assim, as técnicas de PEO e pulverização catódica de magnetrão são técnicas de modificação de superfícies promissoras para a funcionalização de superfícies de Ta para implantes dentários.

Palavras-chave — Tântalo; Nanopartículas de Zinco; Oxidação por Plasma Eletrolítico; Pulverização Catódica de Magnetrão; Resistência à Corrosão; Atividade Antimicrobiana

Abstract

Nowadays, the main causes of the rejection of dental implants are their poor osseointegration and the bacterial adhesion and growth, which may lead to peri-implantitis disease. The osseointegration and the bacteria adhesion inhibition can be enhanced by modifying implant surface properties.

This thesis is focused, in a first phase, on the surface modification of metallic tantalum (Ta), by plasma electrolytic oxidation (PEO). The modification by PEO intends to promote the surface bioactivity and accelerate the osseointegration by mimetic the morphology and chemical from the bone, with the formation of micro/nano-porous structures and the incorporation of osteoconductive elements (calcium (Ca) and phosphorus (P)). In a second phase, over these bioactive surfaces, zinc (Zn) nanoparticles (NPs) with and without a thin carbon (C) layer are deposited by magnetron sputtering to endow this surface with antimicrobial activity.

Different quantities of NPs deposited on the bioactive surfaces were tested. Increasing the deposition time and/or decreasing the working pressure, it was possible to deposit a higher amount of Zn NPs with different morphologies and sizes. The zinc ions release increased with the amount of the NPs and decreased when the carbon layer covered the NPs. The chosen optimized surfaces, the one with lower and the one with higher ionic release, were further studied regarding the antimicrobial activity and corrosion resistance. The presence of Zn NPs had a great impact on the improvement of the antimicrobial capacity, as the higher quantity of Zn NPs (and higher zinc ions release) showed the highest *C. albicans* growth inhibition compared to the porous Ta₂O₅ surface. The C layer did not reveal a significant difference when compared to the respective surface. The corrosion results revealed that the formation of Ta₂O₅ by the PEO lead to improvement of the corrosion behavior, compared to untreated Ta surfaces. On the other hand, the incorporation of metallic Zn NPs promoted the degradation of corrosion resistance, which improved as a function of immersion time and became closer to the porous Ta₂O₅ surface corrosion behavior. These results demonstrated that the deposition of Zn NPs onto porous Ta₂O₅ surfaces efficiently inhibits the microbial growth. Thus, the PEO and magnetron sputtering are promising surface modification techniques for functionalize Ta surfaces for dental implants.

Keywords — Tantalum; Zinc Nanoparticles; Plasma Electrolytic Oxidation; Magnetron Sputtering; Corrosion Resistance; Antimicrobial Activity.

Table of Contents

List of Figures	viii
List of Tables.....	xi
Introduction	1
Chapter 1 - State of Art	3
1.1. The tooth	4
1.2. Dental implants.....	5
1.2.1. Implant stabilization and interaction with bone tissue	6
1.2.2. Dental implants requirements	8
1.2.3. Dental implant biomaterials	8
1.2.4. Ti-based dental implants' main failures	9
1.2.4.1. Poor osseointegration and peri-implantitis disease	10
1.3. Biofunctionalization of metallic surfaces for dental implants	12
1.3.1. Plasma electrolytic oxidation	13
1.3.2. Magnetron sputtering.....	14
1.4. Tantalum and tantalum oxide.....	16
Chapter 2 - Sample Preparation and Characterization Techniques.....	18
2.1. Surface modification techniques.....	19
2.1.1. Plasma electrolytic oxidation for bioactive surfaces development.....	19
2.1.2. Magnetron Sputtering for antimicrobial NPs deposition	20
2.1.2.1. Target and sample holder cleaning.....	20
2.1.2.2. Optimization of the deposition of zinc nanoparticles.....	21
2.1.2.3. Deposition of zinc nanoparticles under optimized conditions	22
2.1.2.4. Deposition of a carbon layer over the Zn nanoparticles	22
2.2. Surface characterization techniques	23
2.2.1. Topographic and morphological characterization	23

2.2.1.1. Scanning electron microscopy - SEM	23
2.2.1.2. Scanning transmission electron microscopy- STEM.....	24
2.2.2. Chemical characterization.....	25
2.2.2.1. Energy Dispersive X-Ray Spectroscopy - EDS	25
2.2.2.2. Inductive Coupled Plasma Optical Emission Spectroscopy – ICP-OES	25
2.2.3. Functional characterization	26
2.2.3.1. Colony forming units - CFU	26
2.2.3.2. Corrosion resistance characterization	28
Chapter 3 - Results and Discussion	30
3.1. Preparation of micro/nano-porous Ta surfaces and incorporation of osteconductive elements	31
3.2. Optimization of Zinc nanoparticles deposition.....	32
3.3. Deposition of a carbon layer over the optimized surfaces	41
3.5. Antimicrobial behavior	43
3.6. Corrosion behavior	45
Chapter 4 - Conclusions e Future Work	66
References.....	69
Annex 1: EDS spectra.....	75
Annex 2: First Draft of Paper 1	76
Annex 3: First Draft of Paper 2	93

List of Figures

Figure 1 - Schematic representation of a human tooth. Adapted from [13].....	4
Figure 2 - Schematic representation of a complete dental prosthesis. Adapted from [16].	5
Figure 3 - Examples of commercially available dental implant geometries [18].....	5
Figure 4 - Behavior of the different types of stability over time after implant placement. Adapted from [21].....	7
Figure 5 - Different tissue interaction of dental implants. Adapted from [36].	10
Figure 6 - Schematic representation of A) island, B) layer and C) Stranski-Krastanov thin film growth mechanisms.	15
Figure 7 - A) Plasma electrochemical oxidation's anodization system. B) Electrochemical cell.	19
Figure 8 - Interior of the deposition chamber.....	20
Figure 9 - Interaction between the electron beam and the sample.	23
Figure 10 - ICP-OES calibration curve.	26
Figure 11 - Schematic representation of the used dilutions in CFU's technique.....	27
Figure 12 - A) 3-electrode electrochemical cell. B) Heating and circulation system of water....	28
Figure 13 - SEM micrographs of A) Ta and B) Ta ₂ O ₅	31
Figure 14 - EDS spectra of A) Ta and B) Ta ₂ O ₅ samples.....	32
Figure 15 - STEM micrographs of A) CD-P6.3_C0.5_t250, B) D1-P4.0_0.5_t250 and C) D2-P2.0_C0.5_t250 conditions: depositions with work pressure variation. Scale: 1 μ m on the left and 0.5 μ m on the right.	33
Figure 16 - STEM micrographs of A) D3-P6.3_C0.5_t500 and B) D4-P6.3_C0.5_t1000 conditions: depositions with deposition time variation. Scale: 1 μ m on the left and 0.5 μ m on the right.	34
Figure 17 - STEM micrographs of D5-P6.3_C1_t250 condition: deposition with current density variation. Scale: 1 μ m on the left and 0.5 μ m on the right.....	35
Figure 18 - STEM micrographs of D6-P2.0_C0.5_t500 condition: deposition with work pressure and deposition time variation. Scale: 1 μ m on the left and 0.5 μ m on the right.....	35
Figure 19 - STEM micrographs of D7-P2.0_C1_t500 condition: deposition with work pressure, deposition time and current density variation. Scale: 1 μ m on the left and 0.5 μ m on the right.	36

Figure 20 - STEM micrographs of D8-P2.0_C1_t500_T150 condition: deposition with work pressure, deposition time, current density, and temperature variation. Scale: 1 μm on the left and 0.5 μm on the right.	36
Figure 21 - Summary flowchart of the main conclusions drawn from the STEM micrographs.	37
Figure 22 - SEM micrographs of the Si substrate with Zn nanoparticles deposited under A) CD-P6.3_C0.5_t250, B) D2-P2.0_C0.5_t250, C) D4-P6.3_C0.5_t1000, D) D5-P6.3_C1_t250, E) D6-P2.0_C0.5_t500 and F) D7-P2.0_C1_t500 depositions. Scale: 0.4 μm	39
Figure 23 - Zn ²⁺ ion release profile for TaCaP_CD, TaCaP_Zn4, TaCaP_Zn6 and TaCaP_Zn7 samples.	40
Figure 24 - SEM micrographs of A) TaCaP_Zn4 and B) TaCaP_Zn7 samples.	41
Figure 25 - SEM micrographs of A) TaCaP_Zn4C and B) TaCaP_Zn7C samples. Scale: 5 μm on the left and 2 μm on the right.	42
Figure 26 - Zn ²⁺ ion release profile for TaCaP_Zn4, TaCaP_Zn4C, TaCaP_Zn7 and TaCaP_Zn7C samples.	43
Figure 27 - Cell viability of <i>Candida albicans</i> after 5 and 24 h of incubation on TaCaP (control), TaCaP-Zn4, TaCaP-Zn4C, TaCaP-Zn8 and TaCaP-Zn8C surfaces. Significant values as * $p \leq 0.05$, ** $p \leq 0.01$, *** $p \leq 0.001$ and **** $p \leq 0.0001$, significant reduction compared to control (TaCaP surface).	45
Figure 28 - OCP vs. SCE values for the 5 studied time-points.	46
Figure 29 – Potentiodynamic curves A) immediately after immersion (0h) and B) 14 days after immersion.	49
Figure 30 - Bode plot of A) Ta and B) TaCaP samples after 2, 24, and 48 hours, 7 and 14 days of immersion in artificial saliva at 37°C. (Measured (symbols) and fitted (lines) values of impedance modulus are related to the left axis while the measured (symbols) and fitted (lines) values of phase are related to the right axis).	50
Figure 31 - Bode plot of A) TaCaP_Zn4 and B) TaCaP_Zn4C samples after 2, 24, and 48 hours, 7 and 14 days of immersion in artificial saliva at 37°C. (Measured (symbols) and fitted (lines) values of impedance modulus are related to the left axis while the measured (symbols) and fitted (lines) values of phase are related to the right axis).	51
Figure 32 - Bode plot of A) TaCaP_Zn7 and B) TaCaP_Zn7C samples after 2, 24, and 48 hours, 7 and 14 days of immersion in artificial saliva at 37°C. (Measured (symbols) and fitted	

(lines) values of impedance modulus are related to the left axis while the measured (symbols) and fitted (lines) values of phase are related to the right axis).	52
Figure 33 - Nyquist plot of Ta, TaCaP, TaCaP_Zn4, TaCaP_Zn4C, TaCaP_Zn7 and TaCaP_CaP7C samples after A) 2 hours, B) 24 hours, C) 48 hours, D) 7 days, and E) 14 days of immersion in artificial saliva at 37°C.	55
Figure 34 - Equivalent circuit used to fit Ta sample's EIS values.	57
Figure 35 - Equivalent circuit used to fit EIS values of TaCaP sample and some time-points of TaCaP_Zn4, TaCaP_Zn4C and TaCaP_Zn7 samples.	57
Figure 36 - Equivalent circuit used to fit EIS values of TaCaP_Zn7C sample and some time-points of TaCaP_Zn4, TaCaP_Zn4C and TaCaP_Zn7 samples.	58
Figure 37 – A) SEM micrographs of TaCaP_Zn7 sample after the potentiodynamic test immediately after immersion (scale: 5 μm on the left and 2 μm on the right), and EDS spectra of B) Z1 and C) Z2.	63
Figure 38 - SEM micrographs of TaCaP_Zn7 sample after the potentiodynamic, OCP and EIS tests 14 days after immersion (scale: 5 μm on the left and 2 μm on the right).	64
Figure 39 - A) SEM micrographs of TaCaP_Zn7C sample after the potentiodynamic test immediately after immersion (scale: 5 μm on the left and 2 μm on the right), and EDS spectra of B) Z1 and C) Z2.	65
Figure 40 - SEM micrographs of TaCaP_Zn7C sample after the potentiodynamic, OCP and EIS tests 14 days after immersion (scale: 5 μm on the left and 2 μm on the right).	65
Figure 41 - EDS spectra of A) TaCaP_Zn4, B) TaCaP_Zn6 and C) TaCaP_Zn7 samples.	75

List of Tables

Table 1 - Target and sample holder cleaning conditions.....	21
Table 2 – Deposition parameters of Zn nanoparticles.....	22
Table 3 - EIS fitting parameters after 2 hours of immersion.	60
Table 4 - EIS fitting parameters after 24 hours of immersion.	60
Table 5 - EIS fitting parameters after 48 hours of immersion.	61
Table 6 - EIS fitting parameters after 7 days of immersion.	61
Table 7 - EIS fitting parameters after 14 days of immersion.	62

Symbols and Abbreviations

Ar – Argon

C₄H₆CaO₄ – Calcium acetate

Ca – Calcium

CaP – Calcium phosphate

CP – Commercially pure

DC – Direct current

EC – Equivalent circuit

EDS – Energy disperse X-ray spectroscopy

F⁻ – Fluoride ion

(Fe,Mn)O(Nb,Ta)₂O₄ – Columbite

(Fe,Mn)O Ta₂O₄ – Tantalite

HF – Hydrofluoric acid

(HOCH₂)₂CHOP(O)(ONa)₂·xH₂O – β-Glycerophosphate disodium salt hydrate

ICP - OES – Inductive coupled plasma optical emission spectroscopy

Na – Sodium

NH₄F – Ammonium fluoride

NPs – Nanoparticles

P – Phosphorus

PEO – Plasma electrolytic oxidation

SCE – Saturated calomel electrode

SEM – Scanning electron microscopy

Ta – Tantalum

Ta_{1-x}O_x – Tantalum oxide

Ta₂O₅ – Tantalum pentoxide

STEM – Scanning Transmission Electron Microscopy

XRD – X-ray diffraction

Zn – Zinc

ZnO – Zinc oxide

Introduction

Teeth are an important part of human anatomy, because of their role in chewing and their aesthetic. However, there are health problems, such as gingivitis, diabetes, caries, and poor diet which can lead to tooth loss. Consequently, arises the requirement to create implants capable to replace missing teeth [1]. In the long-term, implant failure due to biological complications is common. Particularly, peri-implantitis disease stands out, which can be generically defined as an infection in the implant adjacent tissues, caused by the accumulation of bacteria (biofilm) on the implant surface causing the regression of the bone tissue [2][3][4]. Moreover, another problem associated with the failure of dental implants is the degradation of the implant's metal, triggered by the corrosion of its surface in a physiological environment (e.g. saliva and blood) [5].

Nowadays, titanium-based (Ti) dental implants are the most commercialized. However, in some cases, their biocompatibility is not sufficient to guarantee the rapid osseointegration of the implant which increases the probability of entrance of microorganisms near the implant surface, that can initiate infection and, consequently, culminate in implant failure [6]. Thus, tantalum (Ta) has been studied as a viable option as a replacement for Ti. Ta and its oxides (Ta_xO_x) have shown to be promising since they are biocompatible and bioactive (both *in vivo* and *in vitro*), with high corrosion resistance [1][7][8].

Surface bioactivity can be enhanced by modulating its topographic and chemical properties through their modification by electrochemical and physical processes. Thus, the topographical modification of Ta surfaces, promoting micro/nano-porous structures, can improve osseointegration, since the micro/nano-pores bring to the surface a morphology similar to the human bone morphology, favoring cell adhesion [9]. The incorporation of constituent elements of bone (osteoconductive elements), like calcium (Ca) and phosphorus (P), also favors osseointegration, since it mimics the chemical composition of the bone [1][10]. Moreover, the presence of particles with antimicrobial properties, like zinc oxide (ZnO), reduces bacteria adhesion and, consequently, reduces the probability of infection and inflammation of the adjacent tissues to the implant [11][12].

In this regard, this work aims to develop innovative Ta surfaces that simultaneously promote osseointegration and prevent possible infections without compromising the corrosion resistance. For this purpose, antimicrobial surfaces were developed and optimized by deposition of zinc

nanoparticles by magnetron sputtering on micro/nano-structured surfaces of Ta₂O₅, doped with Ca and P obtained through plasma electrolytic oxidation (PEO).

This dissertation is organized into 4 chapters to provide a logical and sequential understanding of the developed work.:

Chapter 1 is dedicated to the review of literature of topics of interest for this dissertation.

Chapter 2 presents the materials and procedures used in each stage of this work, as well as a brief description of all the characterization techniques.

Chapter 3 is focused on the results obtained throughout the development of this work and their discussion.

Chapter 4 presents the overall conclusion of this dissertation, as well as the discussion of the future works.

Chapter 1

State of Art

This chapter presents a brief overview of the state of the art based on the bibliographic review of topics of interest to this dissertation, focusing on the tooth morphology, dental implants, their failures and the biofunctionalization of implant surfaces.

1.1. The tooth

Teeth are structures with hard consistency, with calcareous nature in white color, which play a key role in people's daily lives, such as chewing, speech, and facial aesthetics.[1][13]. Each tooth consists of the crown, the visible part above the gum, and the root, which is in the gum and connects the teeth to the jaw (Figure 1). Both the crown and the root are covered by a mineralized tissue, which in the case of the crown is extremely hard and it is called enamel, while in the case of the root it is called cementum. Inside the tooth, beneath the enamel, is the dentin, which delimits the pulp cavity, and is filled by a highly vascularized tissue called the dental pulp [13][14].

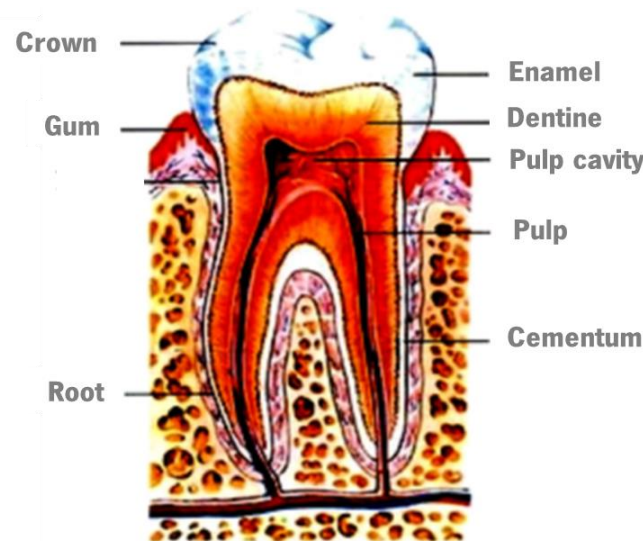


Figure 1 - Schematic representation of a human tooth. Adapted from [13].

Humans have two sets of teeth during life. The first set of teeth is called the primary set and consists of 20 teeth, developed by the age of 3. This set is later replaced during childhood by a second and final set of teeth, which consists of 32 teeth that can be divided into 4 structurally distinct groups: incisors, canines, premolars, and molars [14][15].

During human life, various pathological and traumatic factors occur, as well as dental injuries such as caries and partial or complete tissue loss. These problems can lead to partial or complete loss of dentition. For this reason, over the years, several materials have been studied and developed for the repair and replacement of human teeth [13].

1.2. Dental implants

Nowadays, missing teeth are replaced by dental prosthetics. A complete dental prosthesis consists of three different parts: the artificial crown, the attachment abutment, and the dental implant (Figure 2) [4]. The artificial crown is a ceramic material to mimic the natural crown, while the attachment abutment is a metallic material and it is responsible for connecting the artificial crown to the implant [1]. The dental implant is an artificial metal root, placed in the jaw or maxillary bone, under the gum, supporting the crown [16].

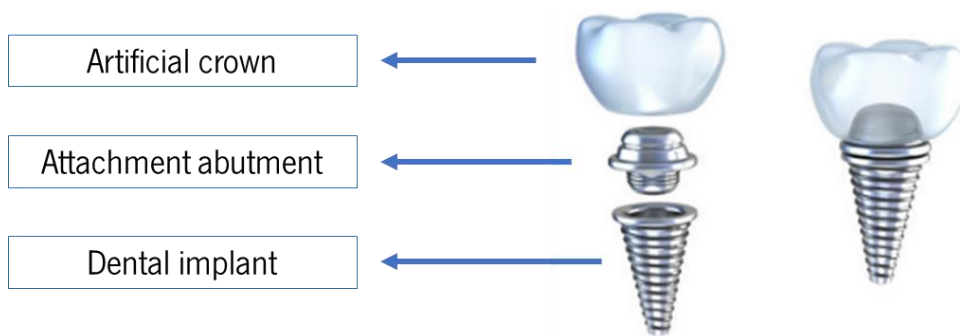


Figure 2 - Schematic representation of a complete dental prosthesis. Adapted from [16].

The geometry of the implant affects the success of it. Although there is no standardization of geometry for dental implants, the cylindrical screwed implant with an external hexagon is the most used geometry, since it promotes an immediate fixation. Therefore, this geometry has been clinically successful over 50 years [17][18]. Figure 3 shows examples of different dental implants geometries commercially available.



Figure 3 - Examples of commercially available dental implant geometries [18].

The history of the evolution of dental prostheses is extensive. Since the beginning of human history, mankind has used various objects and materials to replace missing teeth. The first dental implant was implanted by J. Maggiolo in 1809, which consisted of a gold tube to which was added a crown after concretization of the adjacent tissues [19]. After the First World War, science began to intensify the study and development of biocompatible materials, especially metallic ones, because of the mutilations increasing [17]. Thus, in 1938 an important step in the evolution of dental implants was taken when Dr. P.B. Adams patented an internally and externally threaded cylindrical endosseous implant. In the '40s, Formiggini and Zepponi developed a screw-shaped stainless steel endosseous implant, whose spiral design allowed the bone to grow on the metal [17][19]. This concept of bone growing on metal was defined by Dr. Brånemark in 1952 as osseointegration, which corresponds to the phenomenon of “direct structural and functional bonding between the bone and the surface of the implant”. Brånemark was also responsible for introducing a threaded Ti implant in 1978. This implant developed by Brånemark is considered the first well-documented and successful Ti implant in the history of implantology [19][20].

Up to nowadays, new ways of improving dental implants have been explored. Chemical composition, morphological, topographical, and physical properties of the implant's surface can be modified to improve the dental implant surface biocompatibility and, consequently, to promote osseointegration.

1.2.1. Implant stabilization and interaction with bone tissue

The healing process of the tissues damaged during surgery begins immediately after the implant is placed. Thus, a set of mechanical and biological interactions for implant stabilization begins, being essential to successfully achieve implant osseointegration. Then, Brånemark's definition of osseointegration was redefined as “a time-dependent healing process whereby clinical asymptomatic rigid fixation of alloplastic materials is achieved and maintained in bone during functional loading” [21][22][23]. There are two types of dental implant stability: primary and secondary. Primary stability also referred to as mechanical stability, can be described as the interaction between the bone and the implant surface without biological interaction and it is crucial for the long-term success of the implant. Secondary stability is promoted by biological phenomena of interaction between the implant and the newly formed bone throughout the bone regeneration

and remodeling processes. Over time, primary stability decreases, while secondary stability increases, as shown in Figure 4 [21]. Multiple factors are influencing primary and secondary stability, which will affect the osseointegration process. The factors that affect primary stability are the implant design/geometry, host bone quantity and quality, and surgical protocol, while the secondary stability is related to the primary stability, implant surface properties, and loading conditions [21][24]. Thus, the general stability of the implant is affected by all these factors.

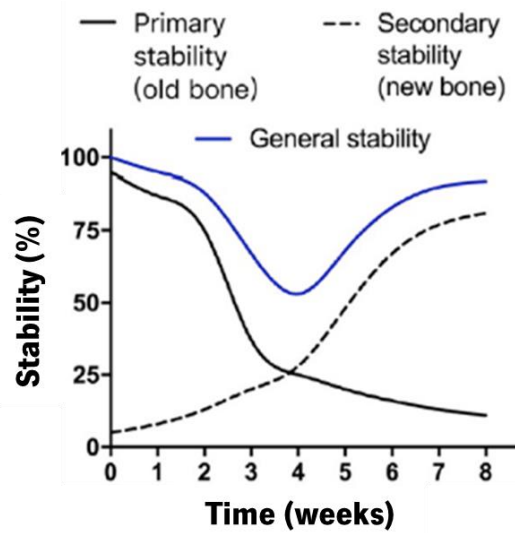


Figure 4 - Behavior of the different types of stability over time after implant placement. Adapted from [21].

The osseointegration process can be divided into several stages. Firstly, the tissues' inflammatory reaction takes place around the implant, that leads to the formation of a hematoma, making blood the first biological component to come in contact with the implant. The angiogenesis process starts, leading to the formation of a network of capillaries that is responsible for the vascularization of bone growth. The cells capable of performing debridement are recruited on the previously formed network of capillaries, and then mesenchymal stem cells are attracted. These mesenchymal stem cells migrate to the implant surface, where they differentiate into osteoblasts, inducing osteogenesis (growth of new bone), and establishing a connection between the implant and the adjacent bone. This formed new bone does not yet possess the required strength to support chewing efforts. This bone is remodelled and a new stronger and less flexible bone is formed, strengthening the connection between the implant and the bone [21][22][25][26]. Thus, an implant is considered successfully osseointegrated when there is no evolution of the relative movement between the functional implant and the bone with which it is in direct contact [25].

1.2.2. Dental implants requirements

A dental implant is a biomaterial that must provide the same functionality as the natural root. A biomaterial was defined in 1991, at the Chester conference, as being a “material intended to contact with biological systems to access, treat, augment, or replace any tissue, organ or function of the organism” [27]. Thus, for a dental implant to be considered a good biomaterial, its surface must be:

- **Biocompatible:** good interaction between the implant and the surrounding tissues [17].
- **Bioactive** ability to form chemical bonds with the surrounding tissues [17][27].
- **Mechanical resistant:** reveal mechanical properties, such as adequate strength and toughness, capable of withstanding the efforts of chewing, wear, and fatigue to which the implant is subjected throughout its life cycle [17].
- **Corrosion resistant :** capacity to avoid the release of corrosion products that are toxic to humans [13][17], since the human organism is a chemically aggressive environment, especially the mouth.
- **Sterilization resistant:** ability to avoid its degradation during sterilization process [17].

1.2.3. Dental implant biomaterials

Through the years, multiple materials were used in the production of dental implants, however, metallic materials have been the most used, since they present suitable biomechanical properties. At the beginning of the XX century, gold, lead, and iridium implants were produced. However, these metals became obsolete due to their toxicity to the human body and low success rate [28].

For many years, stainless steel (SAE 316L) was considered a good material for dental implants due to its mechanical properties, such as ductility and elasticity, as well as its easy production and low cost. However, its corrosion resistance is low when compared with other metals, such as Ti. Also, it has nickel (Ni) in its composition, which may lead to allergic reactions. Thus, stainless steel implants are no longer used as permanent implants. Another material that was used as a dental implant was the cobalt-chrome alloy (CoCr), because of its galvanic and mechanical properties.

However, due to its lower biocompatibility and osseointegration capacity when compared with other metals like Ti, it fell also into disuse [26].

Nowadays, Ti and its alloys (mainly the Ti-6Al-4V alloy) have become the materials of choice in the production of dental implants due to their excellent biocompatibility and favorable mechanical properties. However, these biomaterials show some limitations regarding their tribocorrosion resistance and bioactivity when compared to other metals [26][28]. Although these implants are the most commercialized, a fraction of them fails and are mostly lost in the initial process of healing [17][29], or ultimately fail after 10-15 years of implantation [30].

1.2.4. Ti-based dental implants' main failures

The criterion for the success of an implant is essentially clinical and is related to aspects as the implant's functional capacity, the absence of pain in the patient, and mobility [31]. Hence, implants are not always successful and may fail. Thus, the failure of a dental implant depends on several factors [32].

According to Esposito *et al.* [33], dental implants failures can be divided into 4 main groups: biological, mechanical, iatrogenic, and inadequate patient adaptation failures. Biological failures may also be subdivided into early failures when osseointegration is not achieved due to the non-occurrence of initial bone consolidation, and later failures when the maintenance of initial osseointegration is lost over time. Regarding mechanical failures, these are essentially due to fracture of the implant. Iatrogenic failures are associated with the wrong alignment of the implant and possible nerve damage, while failures due to inadequate patient adaptation are associated with patient dissatisfaction with the aesthetics of the implant and phonetical and psychological problems [32].

Ti-based dental implants show biological failures related to insufficient early osseointegration and high probability to occur a bacterial infection; mechanical failures concerning corrosion wear particles release; and surgical trauma, premature overloading, improper surgical placement, inadequate quantity and quality of host bone that can cause an iatrogenic failure [30][34].

1.2.4.1. Poor osseointegration and peri-implantitis disease

When Ti-based implants are placed, interactions between their surface and human biological fluids and tissues occur. After implantation, two different responses may happen (Figure 5). In the first scenery, direct bone-implant contact is established, thus osseointegration is achieved. In the second scenery, fibrous soft tissue is formed around the implant, encapsulating it, which compromises proper biochemical fixation and further leads to implant failure. The surface properties (i.e., surface composition, roughness, and hydrophilicity) have an important role in implant-tissue interaction and, consequently, in proper osseointegration [35][36]. Furthermore, implant micromotions also play a key role in osseointegration and implant failure. These have a negative influence on osseointegration and bone remodeling by allowing the formation of fibrous tissues on the resulting gap between the implant and the bone, inducing bone resorption [34].

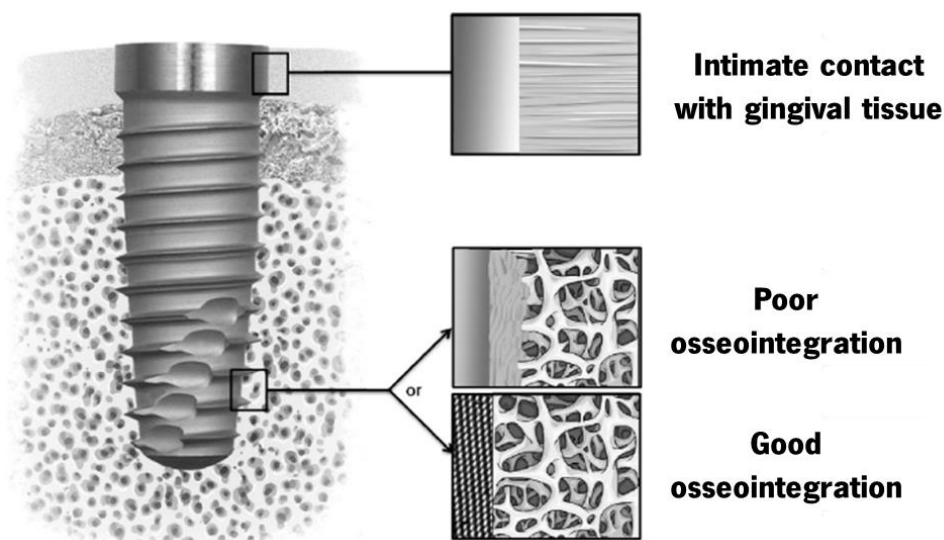


Figure 5 - Different tissue interaction of dental implants. Adapted from [36].

Another main cause of dental implants failure is the development of infections as a response to microbial (e.g., bacterial or fungal) colonization onto the implant surface, that can take place during and/or after surgery [37][38]. The first and the most critical step leading to infection is microbial adhesion. Microbial colonization and biofilm formation on the implant surface may result in peri-implantitis disease, which can be characterized as an infection on the bone tissue. The infected tissues can trigger an immune response that can lead to bone resorption which may compromise the implant's anchorage leading to its loss [4][17][37].

1.2.4.2. Corrosion resistance

The corrosion of a material consists of its gradual and spontaneous degradation when exposed to a hostile environment, occurring chemical oxidation/reduction reactions on the surface. This phenomenon occurs frequently in metallic implants placed in the human body since the environment in which they are placed, such as blood and saliva, can be corrosive [37][39]. In metals, the presence of an oxide film, spontaneously formed (passivation oxide), works as self-protection against corrosion, forming a barrier (just with few nanometers thick) between the metal and the surrounding environment. The degree of protection of the film is determined by the amount of metal ions transferred through it and its stability against dissolution [40].

Although Ti and its alloys are considered corrosion-resistant materials due to the stability of the passive titanium oxide (TiO_2) film, this oxide can be degraded when put under particularly aggressive *in vivo* conditions. When it is in contact with plasma from the blood due to chloride ions (Cl^-), local corrosion is induced and metallic ions from the passive film are released, being more dangerous and harder to predict than uniform corrosion [37][39][40]. Regarding dental implants, the corrosion of the metallic implants is exponentiated not only by Cl^- ions but also by fluoride and hydrogen ions (F^- e H^+), all of them present in saliva. Furthermore, fluoride ions are used very frequently to prevent caries, which may induce the degradation of Ti (and its alloys) dental implants [41].

The corrosion of materials used in implants is affected by several different factors, such as the material itself (chemical composition, microstructure, and surface features) and the pH of the surrounding environment. Regarding pH of the dental implant's surrounding environment, it varies between 5.3 and 5.6 right after surgery, stabilizing at 7 afterward. However, due to several factors such as tobacco, food, and oral hygiene, the pH near the implant can vary between 3 and 9 significantly influencing the corrosion behavior of Ti implants [39][40][42]. Furthermore, regarding the microstructure and surface features of the material, it is reported that Ti corrosion behavior is directly associated with the existence of pores and their size and morphology, the oxide thickness, and the Ti ability to self-heal or passivate [43].

Corrosion and degradation of dental implants can lead to the release and accumulation of corrosion products in the peri-implant tissues which can trigger inflammatory reactions and can induce and/or promote the occurrence of peri-implantitis disease, culminating in the loss of bone tissue

adjacent to the implant [37][41]. Thus, the corrosion resistance of dental implants directly dictates its failure or its success.

To solve these limitations associated with the commercialized Ti-based implants, processes of surface modification of Ti are being reported. Another strategy being studied is the replacement of Ti implants by other biocompatible metals, such as Ta, since this metal is very resistant to the ions responsible for the corrosion of Ti dental implants, specially to the F ion [9][44][45].

1.3. Biofunctionalization of metallic surfaces for dental implants

The surface modification of the biomaterial allows to tailor the surface properties (roughness, porosity, and chemistry) achieving the desired functionalities. This biofunctionalization aims to promote the ability to form a stronger bond between the bone tissue and the implant surface accelerating the osseointegration process [1][46]. Moreover, currently, the highest challenge in dentistry is the development of dental implant surfaces with antimicrobial activity, which is defined as the surface ability to inhibit the microorganisms' (bacteria, fungi, viruses) growth or to kill them [10][35].

The topographic/morphological modification of surfaces is based on roughness through the formation of micro/nano-porosities. The chemical composition of the implant surface is also an important feature in its biofunctionalization since it has an impact on the surface performance regarding osseointegration, antimicrobial activity, and corrosion resistance. Thus, topographic/morphological, and chemical composition modifications on the implant surfaces can be used to functionalize it. The biofunctionalization of metallic surfaces can be achieved by the application of several different surface modification techniques, such as electrochemical processes, and physical vapor deposition techniques (PVD). Electrochemical techniques, as anodization and plasma electrolytic oxidation (PEO), are frequently used to modify metallic surfaces properties through the formation of micro/nano-porous structures, altering the surfaces roughness, wettability, free energy, crystallinity, and chemical composition, thus modeling the surfaces properties to mimic the bone's properties [47]. Furthermore, regarding the biofunctionalization

provided by PVD techniques, the magnetron sputtering process is strongly used in industry to develop mostly thin films, but also the deposition of metallic nanoparticles [48].

1.3.1. Plasma electrolytic oxidation

Plasma electrolytic oxidation (PEO) is an electrochemical surface modification technique used on metals. It is characterized by being a versatile, harmless, and economically viable technique, already being used in industry, that allows the formation of oxides with different morphologies [49][50]. These oxide layers tend to possess good durability and strongly adhere to the surface on which it is formed [47].

PEO, also known as micro-arc oxidation (MAO), is a process derived from anodization and the main difference between them is the fact that PEO operates at high potentials while anodization operates with low potentials. In electric field-assisted anodizing, the formation of porous oxide results from the balance between the oxidation and dissolution reactions of the oxide. Whereas in PEO the formation of pores results from intense electric discharges that create a plasma that expands, releases heat, and collapses. Thus, it is necessary to use a potential above the breakdown potential of the oxide to be formed so that the formation of the micro-arc (plasma) occurs [1][51]. Therefore, this technique consists in the application of a potential between the anode (metallic sample to modify) and the cathode (for example, platinum, lead, or carbon) immersed in an electrolytic solution. As the oxide is formed in the first stage of the process, the high resistance to current flow induces accumulation of charges on the surface of the material, leading to rupture and collapse of the anodic layer, causing the formation of micro/nano-pores [1]. PEO also allows the incorporation of chemical elements from the electrolyte [51][52]. Thus, the morphological and chemical properties of the achieved oxides are affected by the anodizing parameters: the electrolyte composition and its concentration, the applied electrical parameters (potential or current density), and the time and temperature of the process [53]. The PEO process allows the biofunctionalization of Ta surfaces, developing porous structures (morphological functionalization), and by the incorporation of osteoconductive elements (chemical functionalization) mimicking the morphology and chemical of the bone tissue.

The modification at the micro/nanometric level leads to an increase in the contact area between the implant and surrounding tissues, promoting a faster anchorage of the implant to the bone since

the micro and nanostructures play an important role in the cell growth [10][17][54]. Furthermore, it is reported in the literature that the morphological modification of surfaces with the creation of porous structures has an impact on the corrosion behavior of the surfaces: porous materials can present different corrosion behavior from dense materials. However, as the corrosion behavior of porous material depends on several factors, such as amount of pores and pore size, more studies need to be conducted in order to better access how porous structures affect the corrosion behavior of the surfaces [43][55]. Also, the incorporation of osteoconductive elements, like Ca and P, has been widely studied in surface biofunctionalization since calcium (Ca^{2+}) and phosphate (PO_4^{3-}) ions are the main constituents of hydroxyapatite ($\text{Ca}_{10}(\text{PO}_4)_6(\text{OH})_2$), which is the dominant mineral phase in the bone structure. The incorporation of Ca and P mimics the bone composition, resulting in calcium phosphates, with a Ca/P ratio close to the theoretical hydroxyapatite ratio value (about 1.67) [1][10][37][56][57].

1.3.2. Magnetron sputtering

Magnetron sputtering (MS) is a physical deposition technique derived from sputtering. The sputtering process consists of the deposition of particles from a surface (target), which is being sputtered by ions from an inert gas (usual argon), on a substrate. This technique is based on the formation of plasma on a complex atmosphere through the application of a potential between the cathode (target) and an anode (sample-holder) in a deposition chamber. The applied potential difference causes an electrical discharge between the cathode and the anode, ionizing the inert gas in the atmosphere of the sputtering chamber, forming ions that are accelerated and collide with the target, ejecting atoms. This dynamic between the ions is responsible for plasma maintenance. Briefly, the sputtering technique can be described in three main phases. In the first phase occurs the production of the species to be deposited, which undergo from a condensed phase to vapor phase through the collision of inert gas ions with the target. In the second phase, the transport of these species takes place through moment transfer. Finally, in the last phase, the species reach the substrate (sample surface) and condense, forming nucleus that grow, forming a coating on the substrate surface [4]. However, sputtering has not high deposition rates. Thus, in MS technique, a magnetron is placed in the sputtering system and used to create a magnetic field that imprisons electrons near the target, augmenting the number of collisions between the

electrons and atoms from the inert gas, leading to the increase of the ionization process, and therefore, achieve higher deposition rates [4][58].

The formation of a thin film may occur by three different nucleation and growth models (Figure 6), i) island, ii) layer, and iii) Stranski-Krastanov which influence the structure of the obtained thin film. Regarding the island growth mechanism (Figure 6 A), the condensed adatoms have more affinity with each other rather than with the substrate. Thus, the adatoms encounter each other, nucleating small stable clusters. In an initial phase, metals and semiconductors deposited on oxides normally present this type of growth. On the other hand, the layer growth mechanism (Figure 6 B) occurs when the atoms have more affinity to bound with the substrate. Hence, the atoms that arrive on the surface are not reevaporated, building a linear layer. The layers are deposited one after the other above the previous layer, with the top layer being less strongly connected than its previous one. Finally, the Stranski-Krastanov growth mechanism (Figure 6 C) is a combination of the two previously described mechanisms. After an initial layer growth, the formation of islands starts to occur on top of the layers [59].

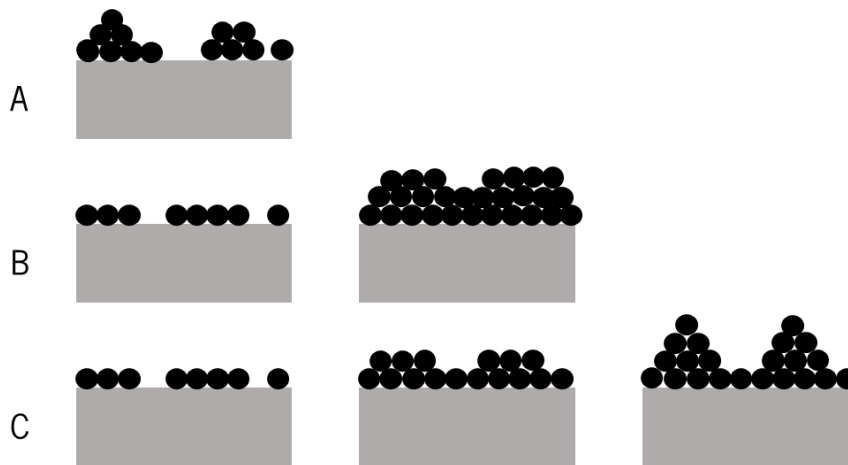


Figure 6 - Schematic representation of A) island, B) layer and C) Stranski-Krastanov thin film growth mechanisms.

Although the MS technique is widely used in the production of thin films, it can also be used in the deposition of nanoparticles, by controlling several deposition parameters like the working pressure, DC voltage, substrates temperature and substrates holder rotation, distance between the target and the substrates and deposition time [60][61].

The incorporation of metallic nanoparticles (NPs) with antimicrobial properties, such as silver oxide, titanium dioxide, silicon, copper oxide, gold, magnesium oxide and zinc oxide (ZnO), has been studied to prevent post-operative infections. In the particular case of Zn, due to its antimicrobial properties, Zn has been added to mouth rinses and toothpaste to control dental plaque and inhibit calculus formation. However, because its NPs form is more toxic to bacteria, Zn/ZnO NPs have been used as antibacterial agents. The antimicrobial activity of ZnO nanoparticles is related to their ability to inhibit bacterial adhesion and biofilm formation by releasing Zn^{2+} ions [4][12][62]. The antimicrobial properties of ZnO NPs are also associated with other molecular mechanisms: loss of membrane integrity and reactive oxygen species (ROS) generation. The damage of the cell membrane is caused by the intracellular accumulation of ZnO NPs. When inside the cells, the metallic ions release, generating ROS that can induce cellular stress and may lead to bacterial death. Antibacterial activity by ZnO NPs is also achieved by the membrane permeability and internalization of NPs [63].

1.4. Tantalum and tantalum oxide

Despite the surface modification of metallic surfaces, another sustainable alternative is the replacement of Ti-based implants by tantalum, since this is a very promising metal in terms of biocompatibility, bioactivity, and corrosion resistance. Tantalum is a metallic element found in low concentration in the earth's crust, in the tantalite $((\text{Fe,Mn})\text{O Ta}_2\text{O}_4)$, and columbite $((\text{Fe,Mn})\text{O}(\text{Nb,Ta})_2\text{O}_4)$ minerals [64]. It is a transition metal from group 5 of the periodic table, with a body-centered cubic structure (bcc). It has a silver color, and it has a high fusion point (about 2980 °C) that stands out from other metals. Tantalum affinity with oxygen leads to the formation of a passive film (oxide layer) on its surface, making this a corrosion-resistant metal. From all the Ta oxides ($\text{Ta}_{1-x}\text{O}_x$), tantalum pentoxide (Ta_2O_5) stands out because it is in the thermodynamic equilibrium [1][64]. This oxide also highlights its thermal stability, high chemical resistance, and high Gibbs energy, characteristics that theoretically indicate the surface has a high capacity to promote osseointegration [1]. In fact, it was demonstrated that Ta_2O_5 is more bioactive than commercialized Ti [6]. Furthermore, Ta reveals to be more resistant to fluoride ions than Ti, under the same anodizing conditions [45].

Due to its outstanding properties, Ta is used in several areas, like electronics for the manufacture of capacitors; medical industry, namely in the manufacture of fracture repair plates, screws to fixate bones, and stents; and dentistry, in the manufacture of dental implants, which is the case of the Ta-based dental implant named Trabecular Metal Implant commercialized by Zimmer [64][46][65].

In this perspective, Fialho *et al.* [66] developed CaP-enriched porous surfaces of Ta₂O₅ doped with Zn/ZnO nanoparticles (deposited on the surfaces) to study the effect of these NPs on the antibacterial activity of these surfaces. It was found that the presence of Zn/ZnO NPs ensures a reduction in the viability of *S. aureus* bacteria after 24 hours of culture. This study also reports the kinetics of zinc ions released from the samples, for 4 hours and 1, 3, and 7 days, noticing that the greatest amount of ions was released in the first 24 hours of immersion. To try to control and prolong the ion release over the first 24 hours, the authors deposited a thin carbon layer over the previously deposited nanoparticles. Although the carbon layer served its purpose of controlling the ion release, it caused a decrease in the antimicrobial activity of the surfaces. Thus, despite the promising results demonstrated by these surfaces that showed interesting properties for use in dental implants, it is still necessary to optimize the modification of Ta surfaces to obtain clinically significant antimicrobial activity.

Chapter 2

Sample Preparation and Characterization Techniques

In this chapter, the materials and procedures used at each stage of the development and characterization of this work are presented. A brief theoretical description of the characterization techniques is provided.

2.1. Surface modification techniques

2.1.1. Plasma electrolytic oxidation for bioactive surfaces development

Plasma electrolytic oxidation (PEO), briefly described in 1.3.1, was performed on an anodization system (Figure 7 A), consisting of a DC power supply (Agilent N5751A), a multimeter (Agilent 34450A 5 1/2 Digit), and an electrochemical cell. Tantalum square samples (99,95% purity, Testbourne) measuring 20x20 mm² were used as the substrate for the PEO process. The samples were first ultrasonically cleaned for 5 minutes in ethanol and in distilled water and air-dried at room temperature. Then, the PEO technique was performed on the samples in potentiostatic mode at 200 V, using an electrolyte composed of 0,35 M of calcium acetate (C₄H₆CaO₄, 99%, Biochem, Chemopharma) and 0,12 M of β-glycerol phosphate pentahydrate salt disodium ((HOCH₂)₂CHOP(O)(ONa)₂·xH₂O, 98%, Sigma-Aldrich), in agitation during 30 minutes at room temperature. In the electrochemical cell (Figure 7 B), the anode, corresponding to the Ta sample, and the cathode, corresponding to a graphite rod, were kept at a constant distance of 30 mm. After treatment, the samples were washed in distilled water and dried at room temperature. These samples were called TaCaP.

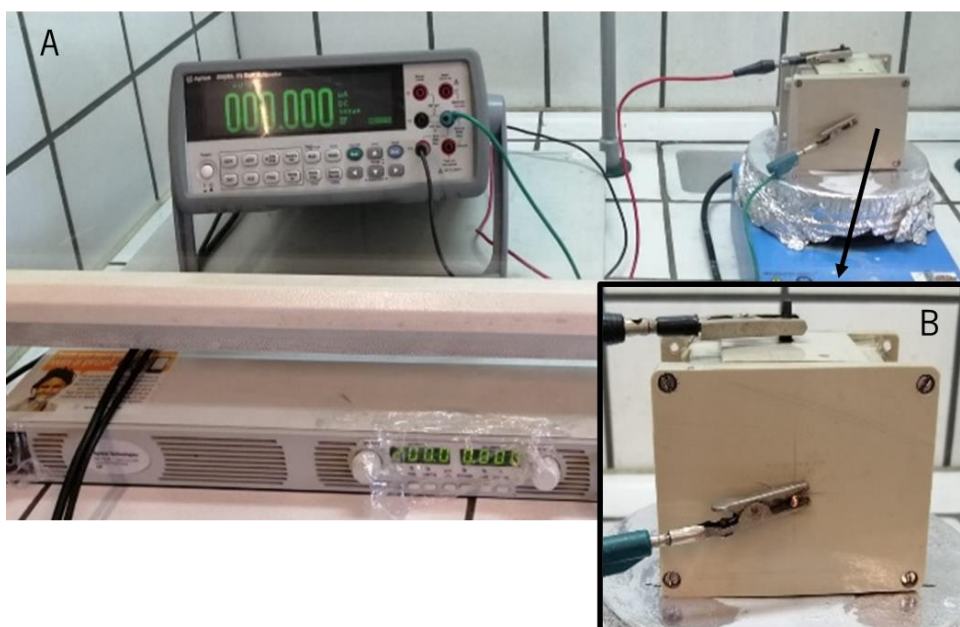


Figure 7 - A) Plasma electrochemical oxidation's anodization system. B) Electrochemical cell.

2.1.2. Magnetron Sputtering for antimicrobial NPs deposition

For the deposition of zinc nanoparticles on the substrates prepared by the PEO process (TaCaP samples), the magnetron sputtering technique (described in 1.3.2) was used in non-reactive mode. The deposition equipment at the Functional Coatings Laboratory II, located at the Physics Department of the University of Minho (Campus of Azurém), was used to perform the depositions.

The deposition system consists of two chambers: the pre-chamber, where the substrate holder is placed before being transferred to the deposition chamber, and the deposition chamber, where the depositions take place. The main chamber has a rotary pump responsible for the primary vacuum, and a turbomolecular pump that generates the secondary vacuum. Power sources, responsible for plasma production, and other elements (pressure sensors, gas flow controllers, and cooling systems) are also connected to the deposition system. The deposition chamber (Figure 8) contains two targets (100x200x6 mm³), 180° apart, the rotational support for the sample holder, and an electrical resistor.

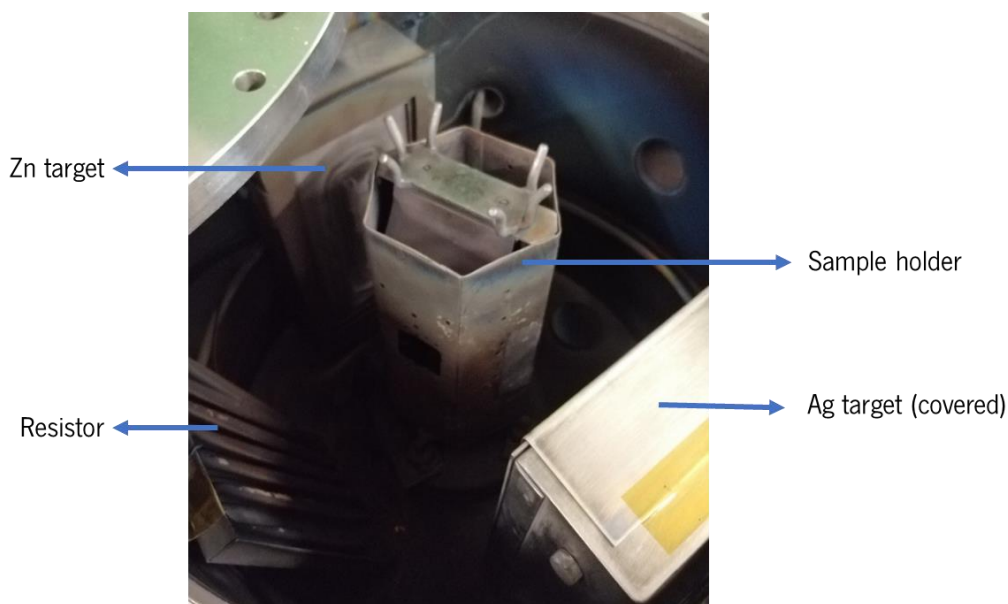


Figure 8 - Interior of the deposition chamber.

2.1.2.1. Target and sample holder cleaning

Before any deposition, it is crucial to clean the target and the sample holder to remove any contaminants that may be on their surfaces. This cleaning is essential between all depositions. The

cleaning conditions used for the target (*etching*) and the sample holder are listed in Table 1, respectively.

Table 1 - Target and sample holder cleaning conditions.

	Target cleaning	Sample holder cleaning
Ar flow	150 sccm	150 sccm
Current in the pulsed source	0.4 A	0.25 A
Pulse duration	1536 ns	-
Frequency	200 Hz	-
DC current density	0.5 mA/cm ²	5 mA/cm ²
Bias	-	-75 V
Work pressure	7 Pa	7 Pa
Time	900s	900s

2.1.2.2. Optimization of the deposition of zinc nanoparticles

To optimize the deposition process of Zn nanoparticles on the TaCaP surfaces, different deposition conditions were tested, starting from the condition reported by Fialho *et al.* [66], used as control (designated CD - P6.3_C0.5_t250 – control deposition). The parameters used in each deposition condition are presented in Table 2. The deposition conditions were designated after the order they were tested (Dx), followed by the working pressure (Px), current density (Cx), deposition time (t) and temperature (T) used. The modification of the deposition parameters aimed to obtain higher amounts of Zn nanoparticles. For each deposition, an argon (Ar) flow of 80 sccm was used and the sample holder was kept at a constant clockwise rotation of 7 rotations per minute (rpm) to obtain a homogeneous distribution of the deposited nanoparticles. A Zn target (99.99%, Testbourne) at the 315° position was used.

Studies from other authors [67] proved that the Zn NPs tend to passivate, creating an oxide outer layer, assuming a Zn core and ZnO shell structure. However, this core-shell morphology was not accessed in this work.

Table 2 – Deposition parameters of Zn nanoparticles.

DESIGNATION	Pressure (Pa)	Current density (mA/cm ²)	Time (s)	Temperature (°C)
CD-P6.3_C0.5_t250	6.3	0.5	250	-
D1-P4.0_C0.5_t250	4.0	0.5	250	-
D2-P2.0_C0.5_t250	2.0	0.5	250	-
D3-P6.3_C0.5_t500	6.3	0.5	500	-
D4-P6.3_C0.5_t1000	6.3	0.5	1000	-
D5-P6.3_C1_t250	6.3	1	250	-
D6-P2.0_C0.5_t500	2.0	0.5	500	-
D7-P2.0_C1_t500	2.0	1	500	-
D8-P2.0_C1_t500_T150	2.0	1	500	150

2.1.2.3. Deposition of zinc nanoparticles under optimized conditions

Following the analysis of the samples prepared in 2.1.2.2., based on the number of nanoparticles, and consequently, their changes in morphology and size, deposition conditions D4-P6.3_C0.5_t1000 and D7-P2.0_C1_t500 were selected to be further investigated. The samples prepared under these conditions were redesignated as TaCaP_Zn4 and TaCaP_Zn7 and stored in the desiccator.

2.1.2.4. Deposition of a carbon layer over the Zn nanoparticles

An additional thin carbon layer was deposited over the optimized Zn nanoparticles (TaCaP_Zn4 and TaCaP_Zn7), to control the Zn²⁺ ion release kinetics and consequently antimicrobial activity through the time. For that, C₂H₂ gas was used as a carbon precursor. The deposition chamber was connected to a DC power source to dissociate the C₂H₂. The carbon layer was deposited using a current of 0.4 A and a pressure of 3 Pa at a frequency of 200 kHz for 60 seconds. The atmosphere in the chamber was formed by a flow of 80 sccm of Ar and 20 sccm of C₂H₂. The carbon layer samples with nanoparticles deposited under D4-P6.3_C0.5_t1000 and D7-P2.0_C1_t500

conditions were referred to as TaCaP_Zn4C and TaCaP_Zn7C, respectively. The produced samples were stored in the desiccator.

2.2. Surface characterization techniques

2.2.1. Topographic and morphological characterization

2.2.1.1. Scanning electron microscopy - SEM

The Scanning Electron Microscopy technique (SEM) is one of the most used techniques to characterize surfaces since it provides a large amount of information and makes it possible to obtain highly magnified images of the surfaces. A high-energy electron beam is focused on the surface (Figure 9), and these electrons penetrate the surface, creating interactions that result in the emission of electrons or photons from the surface. The SEM micrographs result from the detection of the secondary electrons (SE) and the backscattered electrons (BSE). A SE is a low-energy electron that has been ripped out of a surface's atom by the interaction with a high-energy primary electron from the beam. Due to their low energy, SE comes from the most superficial zone of the surface (up to about 10 nm in-depth), providing information about the morphology and topography of the samples' surface. BSE, on the other hand, results from the interaction of the beam's electrons with the electrons closer to the atom's core. The probability of their emission increases with the increase of the atomic mass. Those electrons provide less topographic information of the sample, but more atomic contrast information [58][67][68].

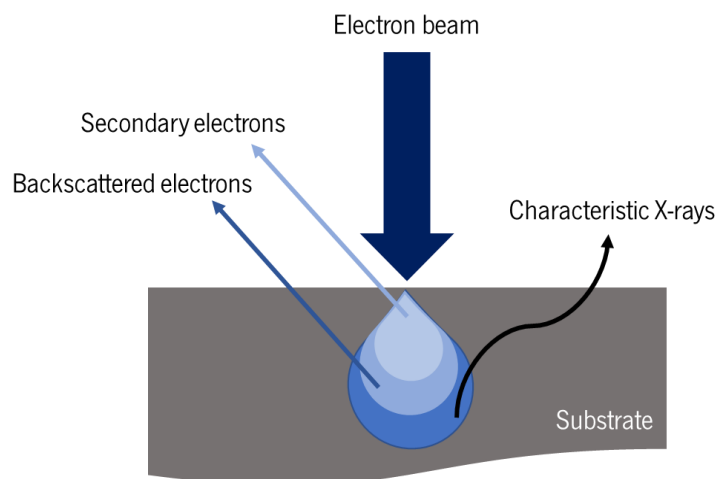


Figure 9 - Interaction between the electron beam and the sample.

In this work, the morphology of the surfaces was analyzed by SEM, using an ultrahigh-resolution scanning electron microscope (Nova NanoSEM 200 microscope, FEI), at SEMAT, in the University of Minho, at 5 kV in secondary mode. In the particular case of the samples with a carbon layer, the analysis was performed at 10 kV in secondary mode.

2.2.1.2. Scanning transmission electron microscopy - STEM

Scanning Transmission Electron Microscopy (STEM) technique uses, as in SEM, a high-energy electron beam to create images of surfaces, but also to obtain images of the internal microstructure of thin specimens [68]. Thus, this high-resolution technique is used to characterize nanoparticles, regarding size, core/shell structure, and agglomeration [67]. In this technique, an electron beam focuses on a solid thin specimen, creating a signal point-to-point of the detected specimen. The created images may be obtained utilizing two types of detectors: bright-field detectors (BF) or annular dark-field detectors (ADF). When the image is obtained using a BF detector, only the direct transmitted beam from the diffraction pattern is detected, producing bright-field images in which the lighter areas correspond to regions where the specimen has suffered little or no interaction with the beam of electrons. On the other hand, dark-field images can be obtained using a BF detector, in which only a single diffracted beam is collected, or using an ADF detector, in which every diffracted or scattered electron beyond a certain minimum angle are collected [67][68]. The images obtained by the ADF detector are of high resolution and contrast, being sensitive to the thickness of the specimen and to the atomic number variation, which is why the light areas in dark-field images correspond to thicker, highly diffracting, or high atomic number areas of the specimen [68].

In this study, STEM technique was used to characterize the morphology of zinc nanoparticles deposited onto carbon lacey TEM grids, using the detector scanning transmission electron microscopy coupled with SEM (SEM/STEM, Nova NanoSEM 200 microscope, FEI), at SEMAT, in the University of Minho, operating at 15 kV in A+B (dark and bright fields) mode.

2.2.2. Chemical characterization

2.2.2.1. Energy Dispersive X-Ray Spectroscopy - EDS

The Energy Dispersive X-Ray Spectroscopy (EDS) technique is used in chemical characterizations. This technique is based on the energy dispersion of characteristic X-rays of each element. X-rays are produced as a result of the ionization of the sample's atoms by the action of a high-energy electron beam. The X-ray emission occurs when an electron from an outer shell fills the space in the inner shell caused by the ejected electron, releasing an amount of energy equal to the difference of energy between the two shells. This released energy is characteristic and different for every atomic transition [68]. Typically, EDS spectrometers are coupled to SEM, TEM, or STEM equipment. The EDS analysis results in an X-ray energy histogram composed of peaks, which represents the type and relative amount of each chemical element present in the sample [67].

To prove the incorporation of Ca and P elements by PEO, as well as the presence of Zn nanoparticles after MS, the samples were analyzed by EDS. The EDAX- Pegasus X4M (EDS/EBSD) spectrometer, at SEMAT, in the University of Minho, operating at 10kV was used to study the qualitative chemical composition of the samples.

2.2.2.2. Inductive Coupled Plasma Optical Emission Spectroscopy – ICP-OES

Inductive Coupled Plasma Optical Emission Spectroscopy (ICP-OES) is a technique that provides quantitative information about the chemical elements present in sample solutions. In this technique, the solution is vaporized, atomized, and ionized, so that the atoms and ions produced in the plasma are excited and produce light in the ultraviolet and visible light regions. The intensity of the emitted light, at characteristic wavelengths, by the element under analysis is measured and related to the concentration of each chemical element present in the sample, thus obtaining the elemental concentration. This intensity is proportional to the concentration of the element under study. The elements present in the sample are detected and quantified using an optical emission spectrometer [68].

In this work, the ICP-OES technique was used to estimate the amount of zinc ions (Zn^{2+}) released, firstly from selected surfaces with Zn nanoparticles and, then from optimized surfaces with the Zn nanoparticles covered or not by the carbon layer. The deposited samples were immersed in 50 mL

of phosphate-buffered saline (PBS) solution for 2, 24, and 48 hours, and 7, 14, and 30 days. The amount of Zn^{2+} ions leached into the PBS was diluted in HNO_3 (2%), in a ratio of 1:3 and measured 3 times for each time-point by ICP-OES (ICP PerkinElmer spectrometer model Optima 8000, at the Biological Engineering Department, in the University of Minho). The calibration curve (Figure 10) was performed using a Zn standard solution (Sigma-Aldrich, 1000 mg/L) prepared in different concentrations of HNO_3 (2%).

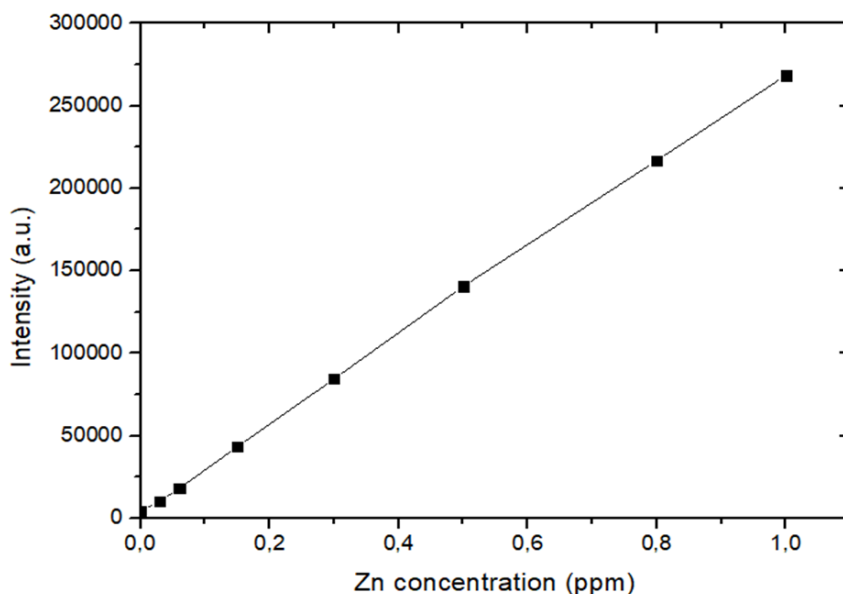


Figure 10 - ICP-OES calibration curve.

2.2.3. Functional characterization

2.2.3.1. Colony forming units - CFU

Determination of bacterial cell numbers is one of the most important procedures in microbiology. Colony forming units (CFU) technique is the widely gold standard method used to assess microbial viability. The two main advantages of the CFU technique are the capacity for counts of any number of microorganisms using dilutions or concentrations, if too many or too few, respectively, and the fact only viable bacteria are counted (excluding dead bacteria and debris). However, CFU presents the disadvantage of clumps of microbial cells being miscounted as single colonies sometimes. Furthermore, CFU results need at least 24 hours to be obtained, making this a time-consuming technique [69]. The inoculum is diluted several times to ensure that the counts are only 25 to 250 colonies per plate [67].

The antimicrobial activity of the surfaces was evaluated through incubation with the pathogenic opportunistic fungus *Candida albicans* SC5314 present in the oral cavity. Firstly, the samples were sterilized in dry heat (180 °C) for 2 h and a pre-inoculum (pre-culture) of *Candida albicans* cells was prepared by picking a colony and inoculating in 10 mL of YPD (1% w/v yeast extract, 1% w/v peptone, and 2% w/v glucose, Formedium). The pre-inoculum was incubated at 30 °C with 120 rpm in orbital agitation overnight (Benchtop Shaking Incubator 222DS). After the growth of the pre-inoculum, *Candida albicans* cells were transferred to a new culture tube, at an optical density ($O.D_{600nm}$) of 0.2, with 20 mL of YPD. This inoculum (cell culture) was incubated in 120 rpm orbital agitation at 30 °C and the cell growth was monitored until reached an $O.D_{600nm}$ of 0.5 (that translated that the *Candida albicans* cells are in the exponential growth phase). At this point, 200 μ L of the inoculum was added to the sterilized sample surfaces and incubated at 30 °C for 5 h and 24 h (cell viability time-points).

To determine the colony counts (CFU/mL), a serial dilution (from 10^{-1} to 10^{-5}) of *Candida albicans* cultures was performed for each time-point. For the first dilution (10^{-1}), 20 μ L of the cell culture on each surface sample is diluted in 180 μ L of deionized water, from where, after resuspension, 50 μ L were pipetted to 450 μ L of deionized water (second dilution - 10^{-2}), and so on (Figure 11). After all the dilutions were prepared, 50 μ L of the latest three dilutions were pipetted five times onto the nutrient agar plates (YPD and agar, Labchem). This method was applied to the optimized surfaces with the Zn nanoparticles covered or not by the carbon layer. The TaCaP sample was used as a control. The experiment was performed in quadruplicate for each sample group.

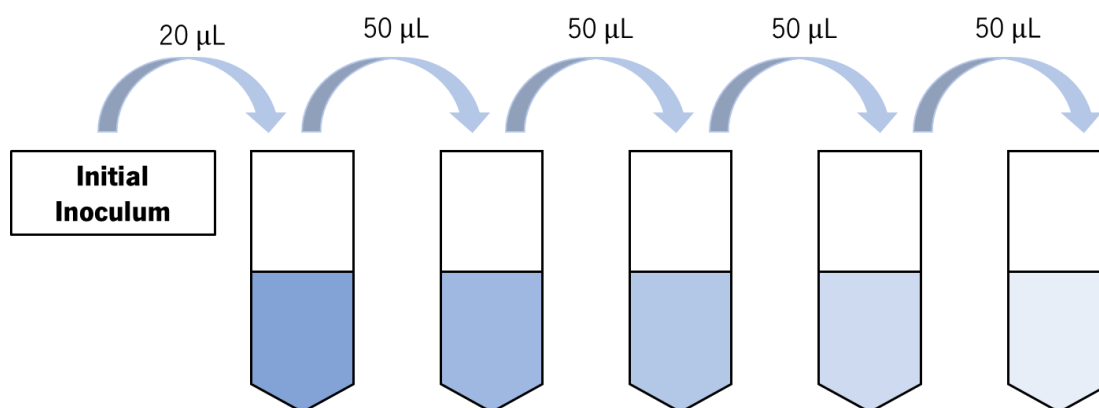


Figure 11 - Schematic representation of the used dilutions in CFU's technique.

Statistically significant differences between the sample groups were measured using one-way ANOVA and Tukey's multiple comparison tests. All statistical analyses were carried out using GraphPad Prism6 statistical software package. All the data are expressed as mean \pm standard deviation.

2.2.3.2. Corrosion resistance characterization

To access the corrosion behavior of the different samples produced, each group of samples was subjected to open circuit potential (OCP), electrochemical impedance spectroscopy (EIS), and potentiodynamic polarization tests. A potentiostat (Gamry Instruments REF600) controlled by software (Gamry Instruments Framework REF14048) was used for this purpose. Samples were set up on a standard 3-electrode electrochemical cell (Figure 12 A) with an exposed sample area of 0.20 cm². In each test, a saturated calomel electrode (SCE) was used as the reference electrode, while a platinum electrode served as the counter electrode and the sample under study as the working electrode. Thus, the untreated Ta samples (used as control) and the samples from the 5 groups of modified Ta surface (TaCaP, TaCaP_Zn4, TaCaP_Zn7, TaCaP_Zn4C, TaCaP_Zn7C) were immersed in 200 mL of modified artificial saliva prepared according to Fusayama [70]: (0.4g/L NaCl, 0.4g/L KCl, 0.795 g/L CaCl₂·2H₂O, 0.005g/L Na₂S·9H₂O, 0.69g/L NaH₂PO₄·2H₂O e 1g/L urea) with a pH of 5.50. The artificial saliva was maintained at 37 °C using a heating and circulation system of water on the outside of the electrochemical cell (Figure 12 B) and its pH was kept using buffer solutions.

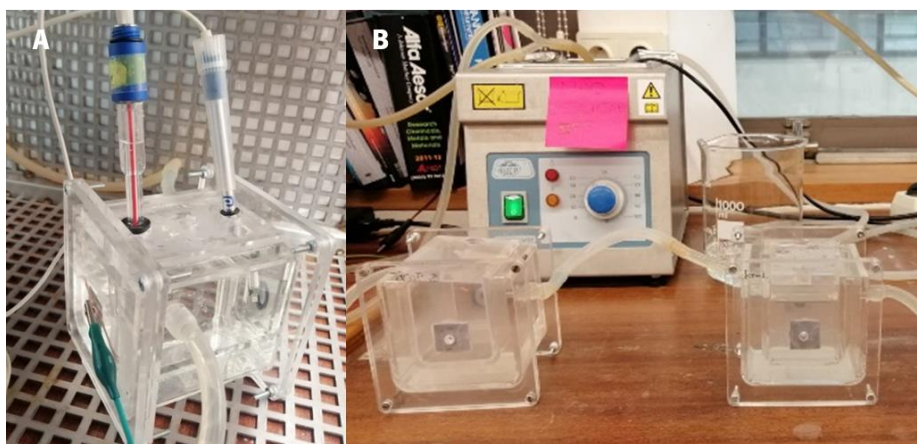


Figure 12 - A) 3-electrode electrochemical cell. B) Heating and circulation system of water.

Each sample was tested after 2, 24, and 48 hours, 7 and 14 days of immersion in artificial saliva. Firstly, OCP was measured and allowed to stabilize for 1 hour at the first time point (2 hours of immersion) and for 30 minutes at the other time points. Therefore, EIS measurements were performed in a frequency range from 0.01 Hz to 10^5 Hz, with an AC sinusoidal perturbation with an amplitude of 10 mV (rsm), relative to the OCP applied to the electrode. In addition, after both 14 days of immersion and immediately after immersion (0 hours), potentiodynamic tests were performed, using a scan rate of 60 mV/min, from -3 V vs. OCP to +1.2 V vs. OCP. Every analysis was performed in triplicate.

Chapter 3

Results and Discussion

In this chapter, the results of the various surface modifications and respective characterizations are analyzed and discussed in detail.

3.1. Preparation of micro/nano-porous Ta surfaces and incorporation of osteoconductive elements

The PEO technique is used to obtain micro/nano-porous Ta surfaces with the incorporation of the osteoconductive elements (Ca and P). The aim is to obtain surfaces morphologically and chemically closer to human bone. As already mentioned, experimental parameters reported by Fialho *et al.* [66] to obtain CaP-enriched porous Ta surfaces with a biomimetic Ca/P ratio were successful. Thus, in this study, the same experimental parameters are used to obtain similar surfaces. As expected, SEM micrographs of a Ta sample (without any treatment) (Figure 13 A) and micrographs from the functionalized PEO sample (TaCaP, Figure 13 B) show that the PEO technique results in the formation of pores of different sizes and diameters on the treated Ta surface (TaCaP), which approximates the surface morphology of this sample to that of human bone [66]. Moreover, the comparison between both Ta and TaCaP EDS spectra (Figure 14) proves the incorporation of Ca and P into the oxide layer.

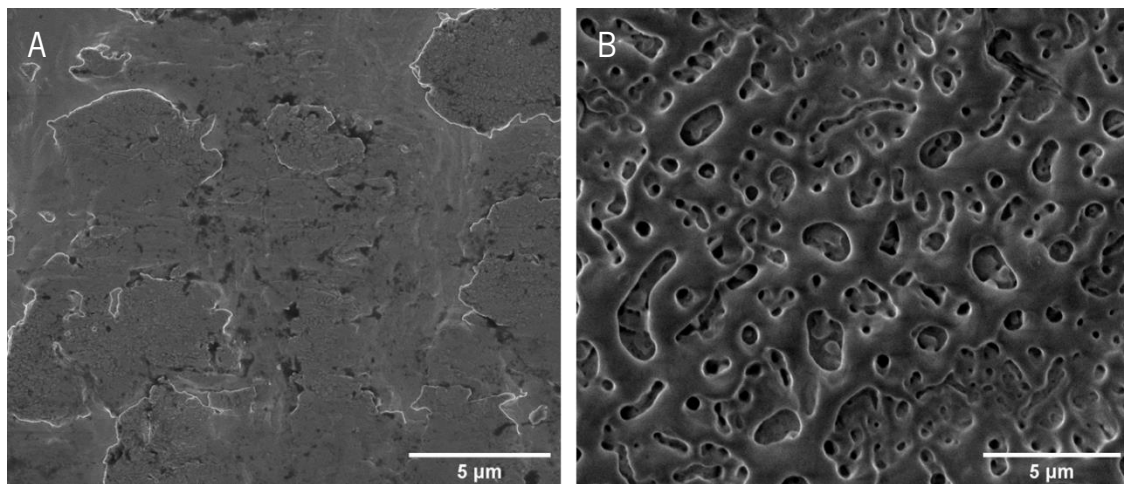


Figure 13 - SEM micrographs of A) Ta and B) Ta_CaP.

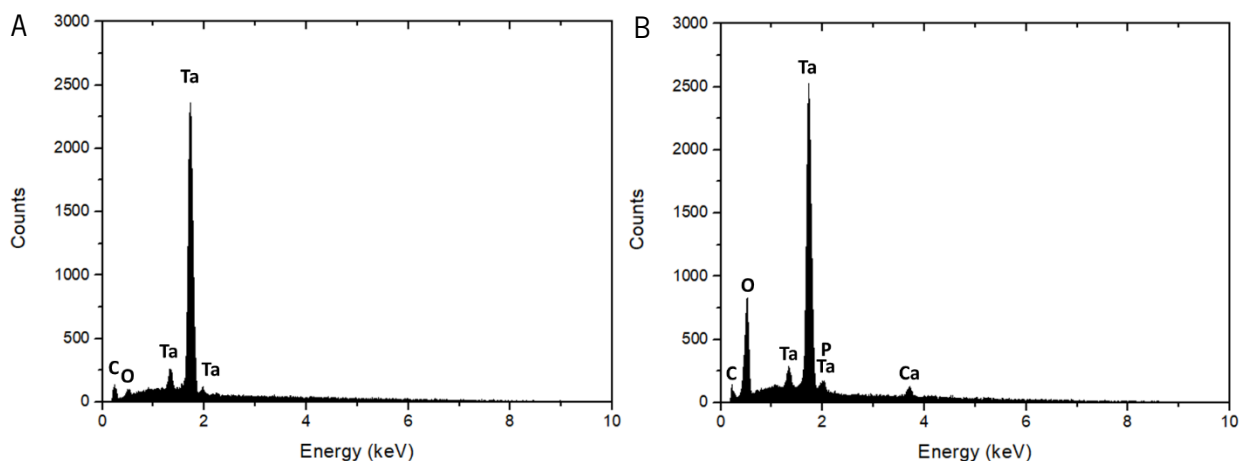


Figure 14 - EDS spectra of A) Ta and B) TaCaP samples.

3.2. Optimization of Zinc nanoparticles deposition

To deposit zinc nanoparticles on the TaCaP surface, the MS technique is used. Starting from the deposition conditions reported by Fialho *et al.* [66], defined as control (CD), new deposition conditions are tested by changing the deposition parameters (Table 2). These new deposition parameters aim to increase the number of nanoparticles (not attaining a thin film) to promote significant antimicrobial activity, not reached in the referred study. Figure 15 to Figure 20 show STEM micrographs of TEM grids used for each of the deposition conditions.

First of all, the effect of working pressure is evaluated on the nanoparticles deposition. The working pressure is reduced from 6.3 Pa (pressure used on the control deposition - CD-**P6.3**_C0.5_t250), to 4 and 2 Pa on D1-**P4.0**_0.5_t250 and D2-**P2.0**_C0.5_t250 conditions, respectively. From the STEM images of CD-P6.3_C0.5_t250, D1-P4.0_0.5_t250, and D2-P2.0_C0.5_t250 (Figure 15), it is possible to observe that the D1-P4.0_0.5_t250 NPs (Figure 15 B) are similar in size and morphology to the ones in CD-P6.3_C0.5_t250 (Figure 15 A). However, the NPs on D2-P2.0_C0.5_t250 (Figure 15 C) look slightly larger and less regularly shaped than the NPs on CD-P6.3_C0.5_t250 and D1-P4.0_0.5_t250 (Figure 15 A and B). Furthermore, for this condition, it seems that a larger number of NPs is deposited on the grid.

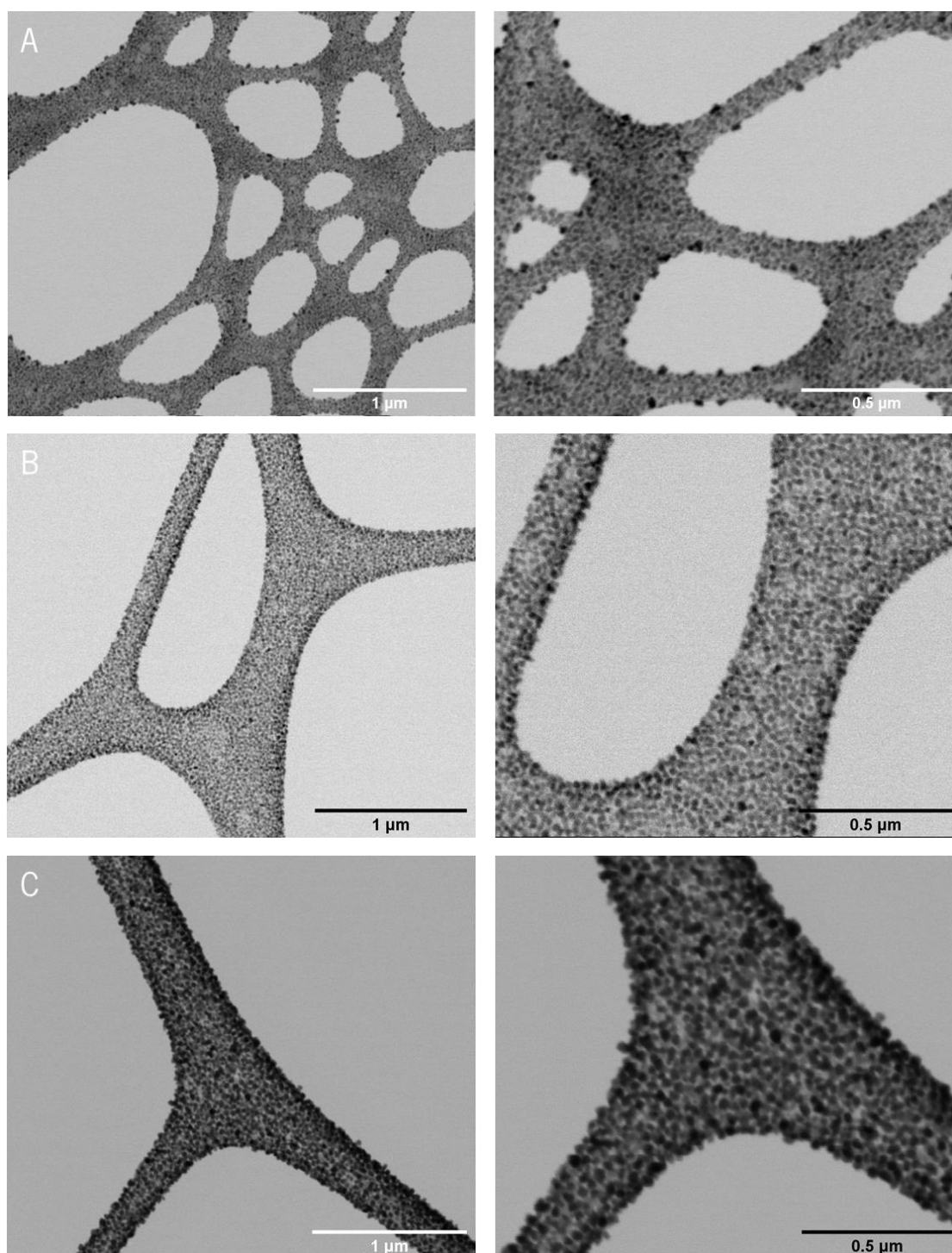


Figure 15 - STEM micrographs of A) CD-P6.3_C0.5_t250, B) D1-P4.0_0.5_t250 and C) D2-P2.0_C0.5_t250 conditions: depositions with work pressure variation. Scale: 1 μm on the left and 0.5 μm on the right.

The second parameter studied is the deposition time. STEM micrographs show that increasing the deposition time from 250 s (CD-P6.3_C0.5_t**250** condition) to 500 s (D3-P6.3_C0.5_t**500** condition) results in Zn NPs (Figure 16 A) with similar size and shape to those in CD-P6.3_C0.5_t250 and D1-P4.0_0.5_t250 (Figure 15 A and B). On the other hand, quadrupling the

CD-P6.3_C0.5_t250 deposition time (D4-P6.3_C0.5_**t1000** condition), results in larger and more irregular NPs (Figure 16 B).

To this point, the NPs obtained under the D4-P6.3_C0.5_t1000 condition parameters are the ones showing more differences from the control's NPs (CD-P6.3_C0.5_t250 - Figure 15 A).

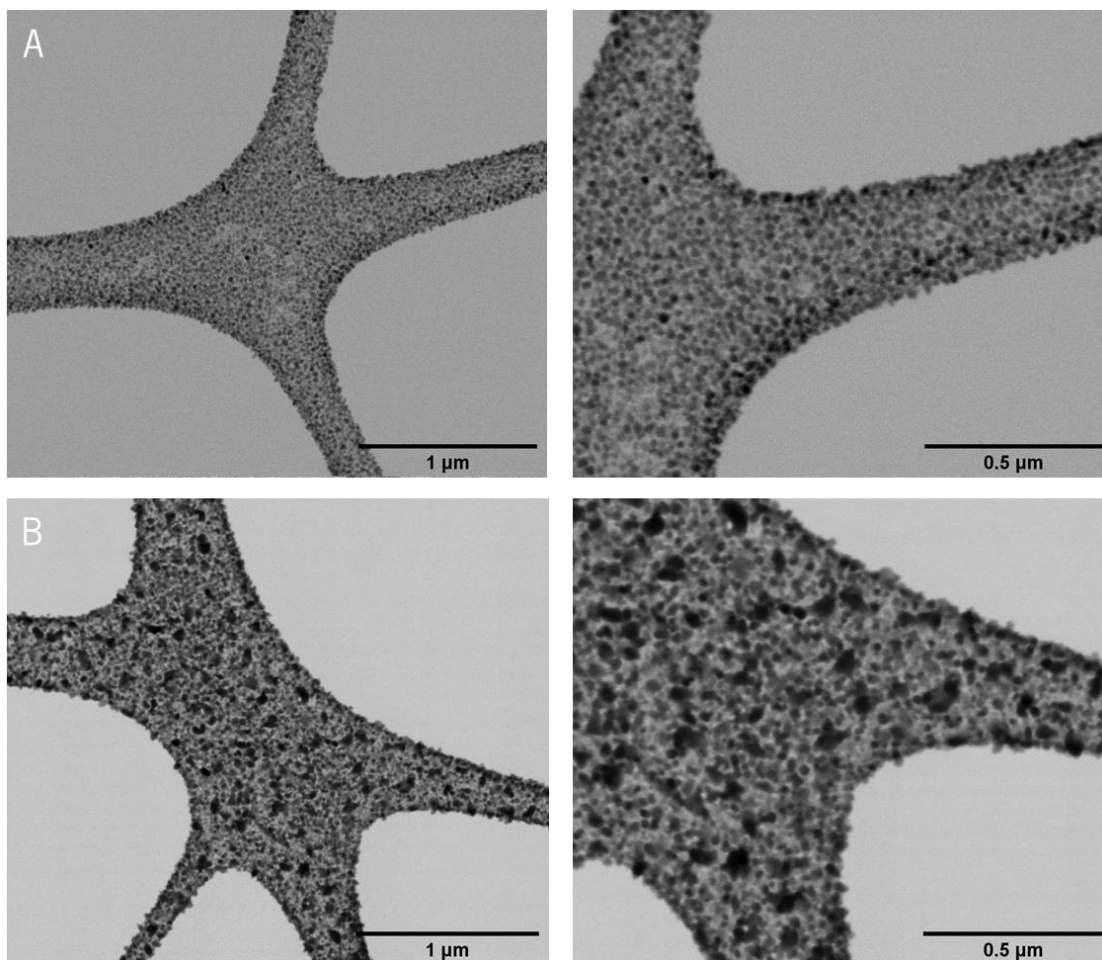


Figure 16 - STEM micrographs of A) D3-P6.3_C0.5_t500 and B) D4-P6.3_C0.5_t1000 conditions: depositions with deposition time variation. Scale: 1 μm on the left and 0.5 μm on the right.

Another deposition parameter tested is the current density, which is increased from 0.5 mA/cm² (CD-P6.3_**C0.5**_t250 condition) to 1 mA/cm² (D5-P6.3_**C1**_t250 condition). This change does not result in significant changes in the size or morphology of the NPs (Figure 17), although a larger amount of NPs seems to be deposited in this TEM grid comparing to CD-P6.3_C0.5_t250's grid (Figure 15 A).

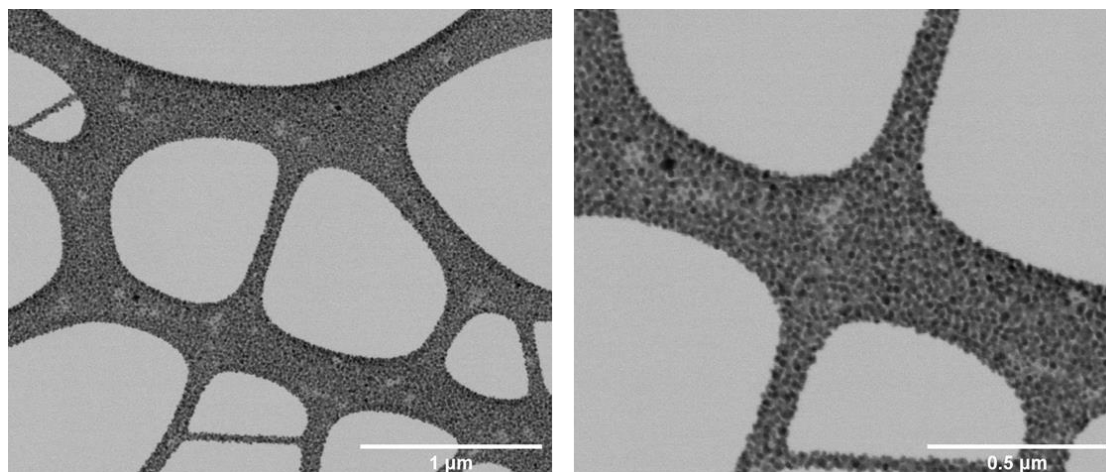


Figure 17 - STEM micrographs of D5-P6.3_C1_t250 condition: deposition with current density variation. Scale: 1 μm on the left and 0.5 μm on the right.

As in terms of working pressure the deposition condition that leads to better results is the D2-P2.0_C0.5_t250, the deposition time used in this deposition is increased to 500s (D6-P2.0_C0.5_t500 condition) to obtain even more improved results in terms of size and morphology of the NPs. SEM micrographs (Figure 18) show that the combination of these two parameters (pressure and time) results in the deposition of larger NPs than the ones in CD-P6.3_C0.5_t250 and D2-P2.0_C0.5_t250 (Figure 15 A and C), due to de agglomeration of some NPs. Moreover, the NPs morphology become more irregular and elongated.

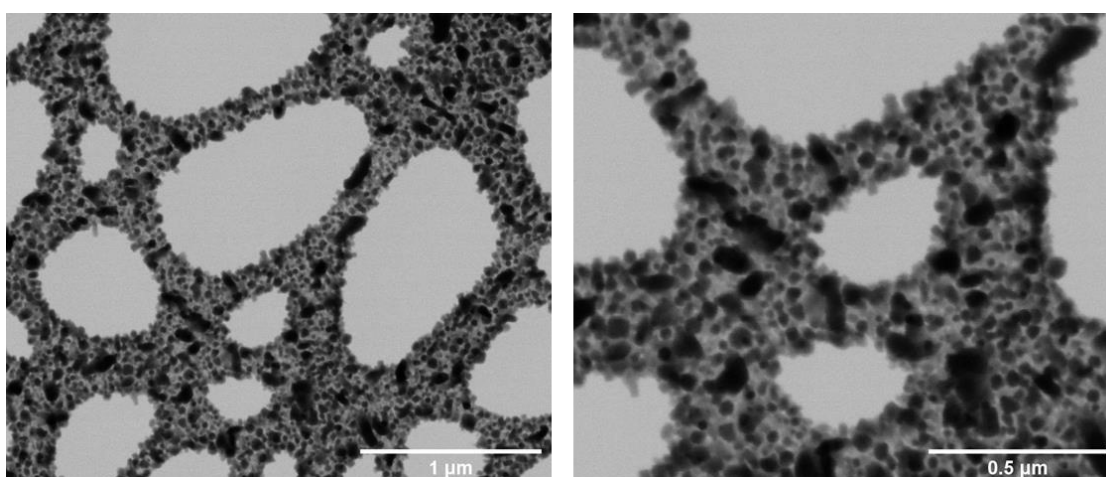


Figure 18 - STEM micrographs of D6-P2.0_C0.5_t500 condition: deposition with work pressure and deposition time variation. Scale: 1 μm on the left and 0.5 μm on the right.

Under the same parameters of D6-P2.0_C0.5_t500 deposition, but with a current density of 1 mA/cm^2 (D7-P2.0_C1_t500 condition) the NPs obtained (Figure 19) are, as expected, much larger

than the NPs deposited under the CD-P6.3_C0.5_t250 condition (Figure 15 A). However, when compared to the NPs from the D6-P2.0_**C0.5**_t500 condition (Figure 18), the NPs from the D7-P2.0_C1_t500 are less irregular, rounder, and have a more homogeneous size distribution.

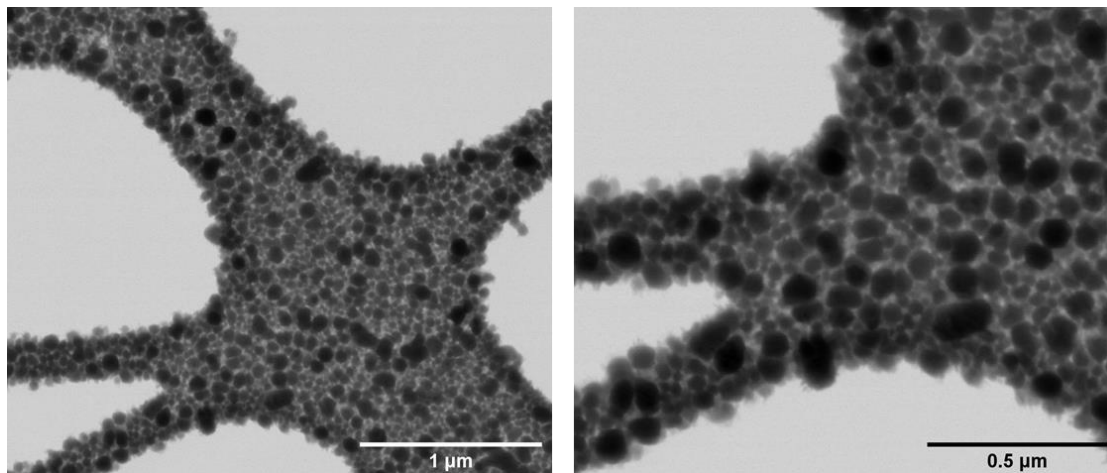


Figure 19 - STEM micrographs of D7-P2.0_C1_t500 condition: deposition with work pressure, deposition time and current density variation. Scale: 1 μm on the left and 0.5 μm on the right.

The same parameters of D7-P2.0_C1_t500 condition, but with the deposition chamber at 150 °C (D8-P2.0_C1_t500_**T150** condition) are used to access the effect of the temperature. STEM micrographs (Figure 20) show that increase the temperature leads to a notorious effect on the morphology of the NPs, as they are elongated, compromising the nanoparticles' rounded shape.

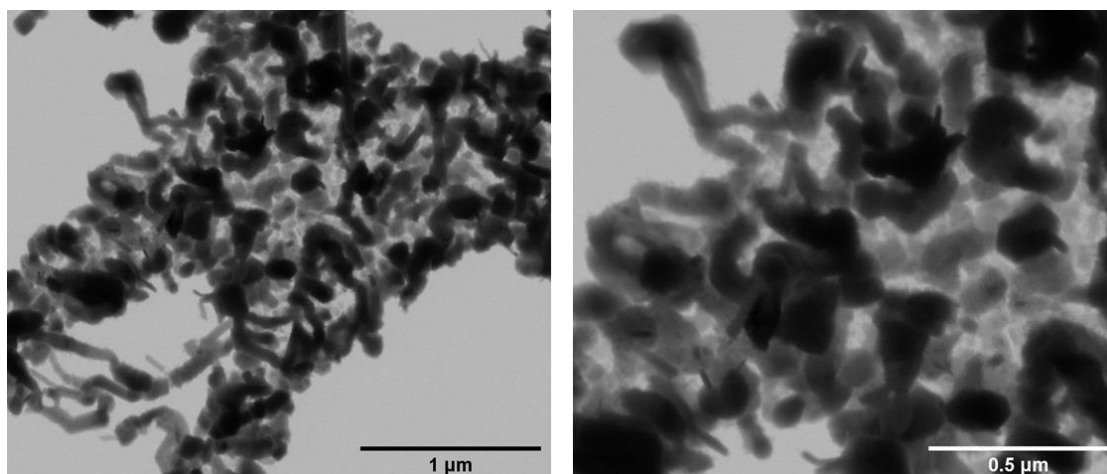


Figure 20 - STEM micrographs of D8-P2.0_C1_t500_T150 condition: deposition with work pressure, deposition time, current density, and temperature variation. Scale: 1 μm on the left and 0.5 μm on the right.

The flowchart from Figure 21 presents the main tendencies observed in the alteration of the amount, size, and morphology of the deposited NPs, resultant from the alteration of the deposition parameters. Generally, the results reveal that decreasing the working pressure (D2-**P2.0**_C0.5_t250 condition - Figure 15-B), increasing the deposition time (D4-P6.3_C0.5_**t1000** condition - Figure 16 B) and the current density (D5-P6.3_**C1**_t250 condition - Figure 17) result in higher amounts of nanoparticles. Furthermore, results prove that combining the referred parameters (D6-**P2.0**_C0.5_**t500** and D7-**P2.0**_C1_**t500** conditions - Figure 18 and Figure 19, respectively) lead to the increase of the nanoparticles' size. Thus, these five deposition conditions are selected to be further analyzed in the next step.

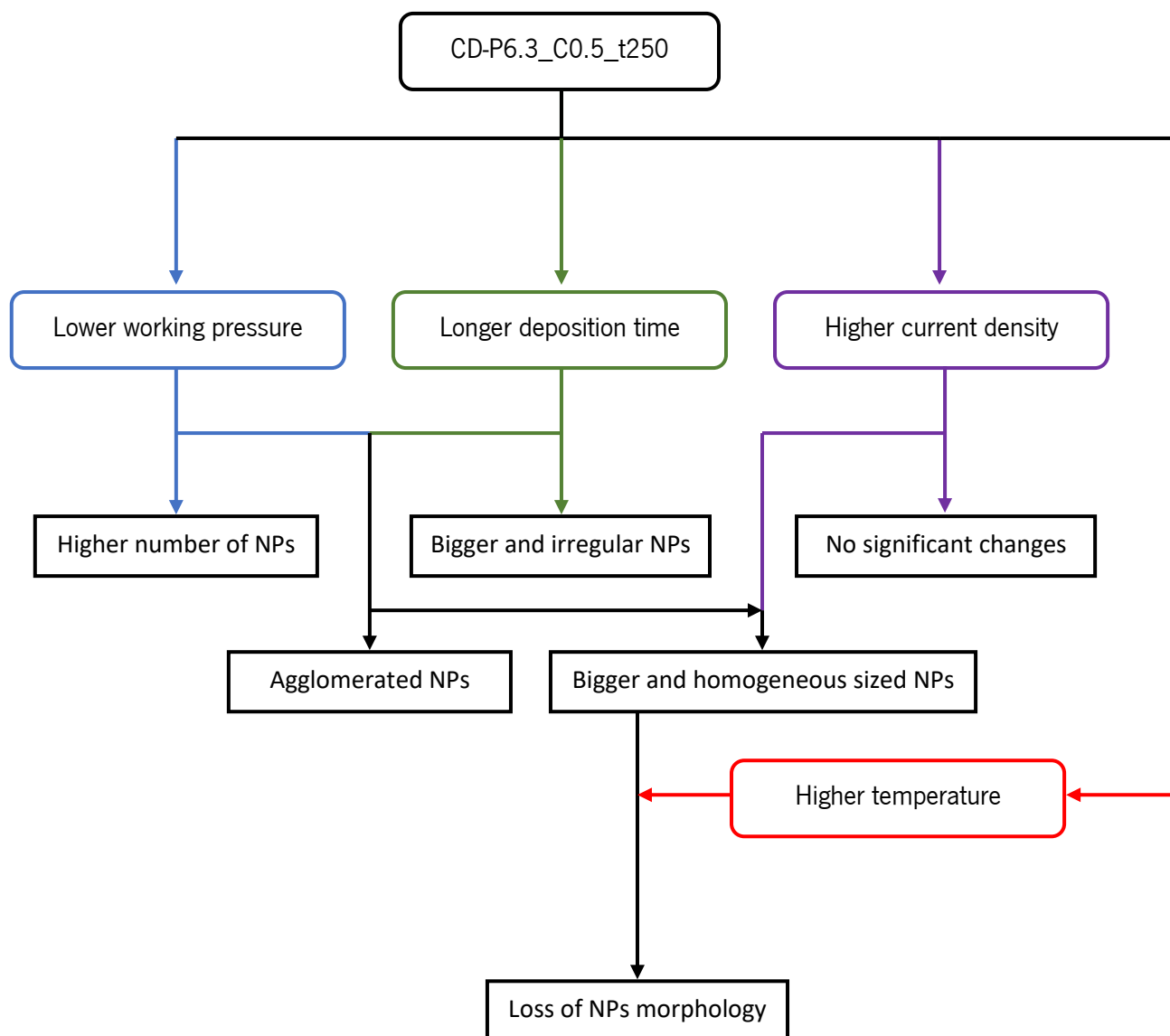


Figure 21 - Summary flowchart of the main conclusions drawn from the STEM micrographs.

SEM analyzes of the silicon used as substrate for the five deposition conditions selected above, as well as in the CD-P6.3_C0.5_t250 deposition (as control), are presented to verify and complement the observations made through the STEM analyses of the TEM grids.

Through the micrographs represented in Figure 22, it is possible to verify that all depositions achieve a good distribution of Zn NPs through the silicon surface, covering the surfaces completely. In the CD-P6.3_C0.5_t250 condition (Figure 22 A), it is possible to observe that the deposited NPs are small and round, in comparison with the ones deposited by the other deposition conditions. On the other hand, in D2-P2.0_C0.5_t250 and D4-P6.3_C0.5_t1000 conditions (Figure 22 B and C, respectively), there is noticed an increment in the size of the NPs, followed by a morphological change, with a mix of smaller (like in CD-P6.3_C0.5_t250 condition - Figure 22 A), larger and irregular NPs being observed. Figure 22 C makes it clear that in the D4-P6.3_C0.5_t1000 condition there is a greater amount of larger and more irregular nanoparticles compared to the D2-P2.0_C0.5_t250 condition (Figure 22 B). The D5-P6.3_C1_t250 condition (Figure 22 D) allows the deposition of Zn NPs extremely similar to the ones in CD-P6.3_C0.5_t250, although few larger NPs are observed. In the D6-P2.0_C0.5_t500 condition (Figure 22 E), as observed through the STEM images (Figure 18), it is visible an increase in the NPs size, as well as a more irregularity in their shape. D7-P2.0_C1_t500 condition (Figure 22 F) leads to the deposition of big Zn NPs with a very different morphology from all the other NPs achieved with the other conditions, with the NPs seeming to be more of agglomerations of smaller NPs, rather than isolated NPs.

Regarding these results, as the number of Zn nanoparticles deposited using the D5-P6.3_C1_t250 condition seems to be too similar to the number obtained using the CD-P6.3_C0.5_t250 condition, the D4-P6.3_C0.5_t1000, D6-P2.0_C0.5_t500, and D7-P2.0_C1_t500 conditions are chosen for further evaluation. This selection aims to analyze the influence of the size (D4-P6.3_C0.5_t1000 condition with smaller NPs and D6-P2.0_C0.5_t500 sample with larger NPs), and morphology (D7-P2.0_C1_t500 condition) of the deposited NPs on the antimicrobial activity and corrosion behavior of the surfaces.

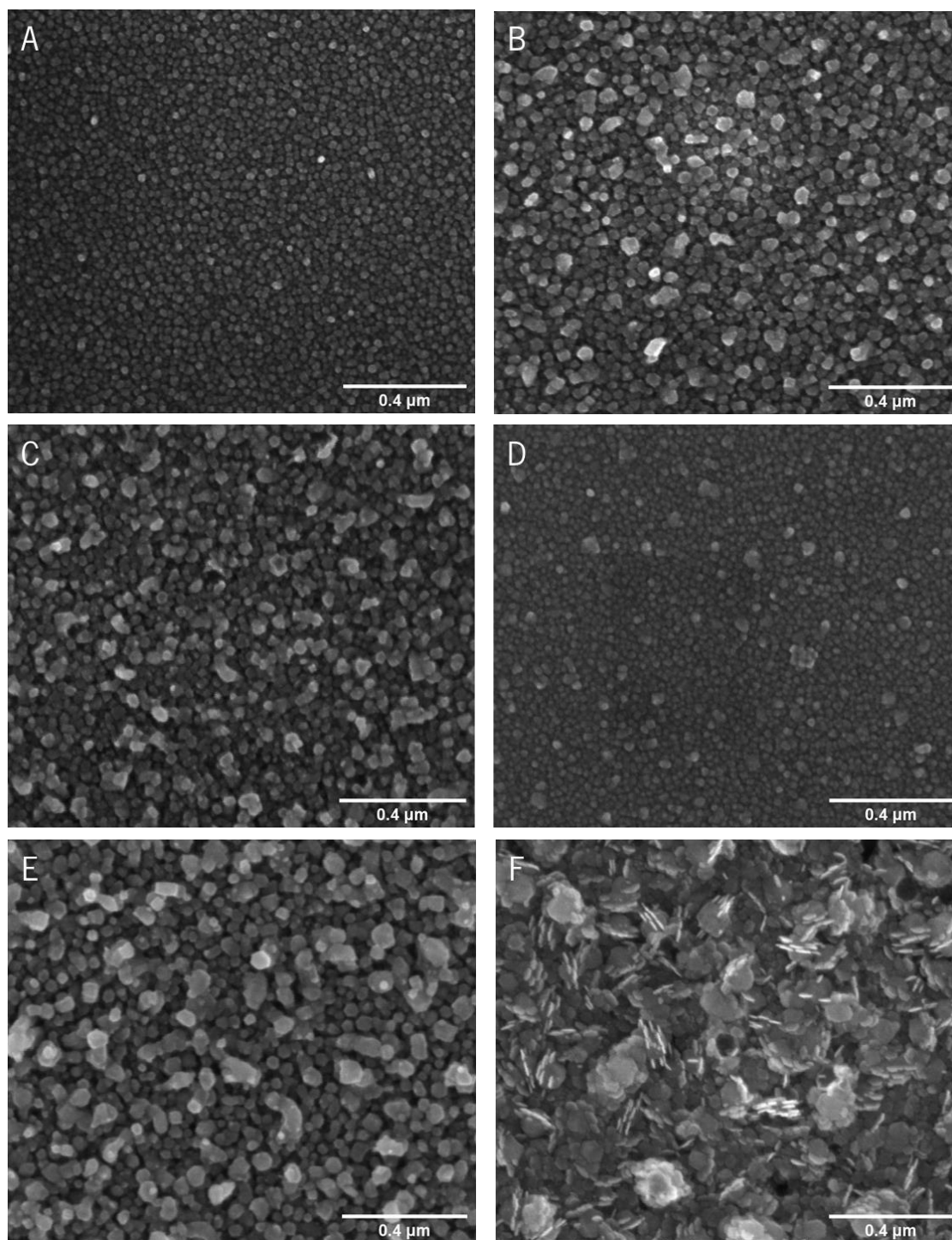


Figure 22 - SEM micrographs of the Si substrate with Zn nanoparticles deposited under A) CD-P6.3_C0.5_t250, B) D2-P2.0_C0.5_t250, C) D4-P6.3_C0.5_t1000, D) D5-P6.3_C1_t250, E) D6-P2.0_C0.5_t500 and F) D7-P2.0_C1_t500 depositions. Scale: 0.4 μm .

Although the STEM and SEM images presented above allow to take some conclusions about the amount, size, and morphology of the deposited NPs, these conclusions are only qualitative, since the obtained NPs do not allow a proper quantification, due to the reduced size of some of the nanoparticles and the coalescence of the bigger ones. Furthermore, EDS analyses of the selected

samples (now redenominated TaCaP_Zn4, TaCaP_Zn6, and TaCaP_Zn7), presented in Annex 1: EDS spectra also do not allow to make any conclusion about the quantity of Zn present in each sample since this is a qualitative technique. Thus, the selected samples, as well as a TaCaP_CD sample serving as control, are analyzed by ICP-OES to study the release of Zn^{2+} ions from the surfaces.

Figure 23 shows the Zn^{2+} ions profile of each surface group after 2, 24, and 48 hours and 7, 14, and 30 days of immersion in PBS.

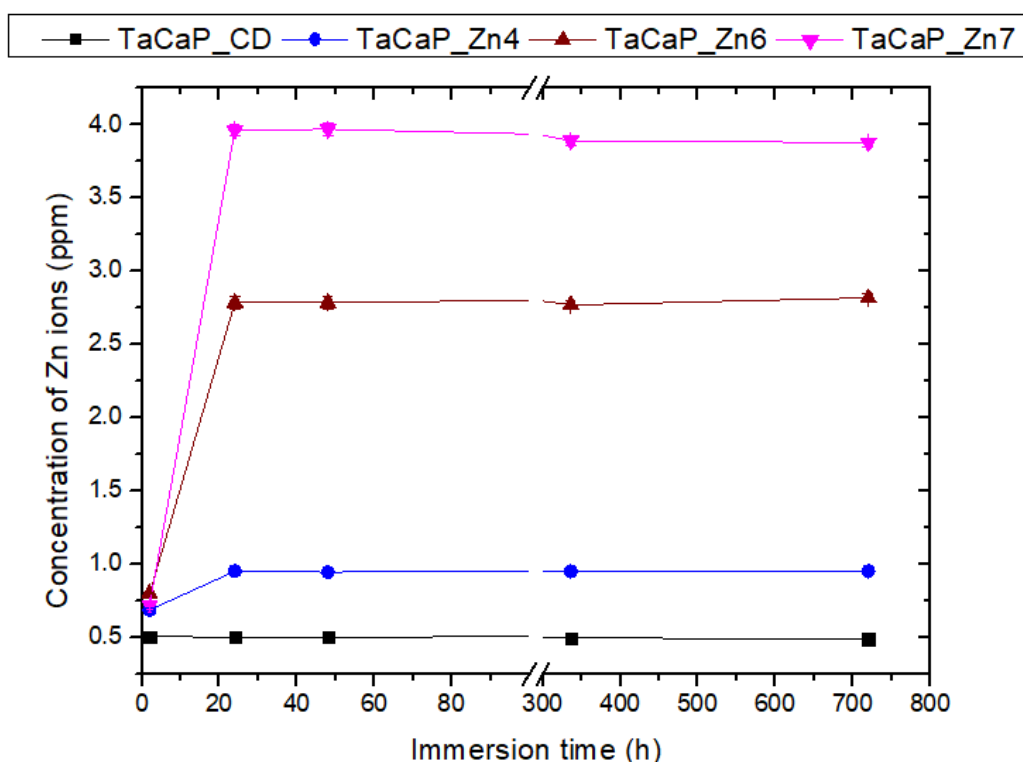


Figure 23 - Zn^{2+} ion release profile for TaCaP_CD, TaCaP_Zn4, TaCaP_Zn6 and TaCaP_Zn7 samples.

All Zn-containing samples show higher ionic release than the overall profile of the TaCaP_CD sample, which shows a maximum concentration of Zn^{2+} ions release of 0.49 ± 0.01 ppm. Between 2 and 24 hours of immersion, all samples reveal similar Zn^{2+} ions release kinetics, achieving the maximum ionic release after 24 hours of immersion, remaining constant afterward. The sample that presents higher concentration of Zn^{2+} ions release is TaCaP_Zn7 (3.96 ± 0.04 ppm), followed by TaCaP_Zn6 (2.79 ± 0.01 ppm) and TaCaP_Zn4 (0.95 ± 0.01 ppm). Thus, it is possible to conclude that the samples with a higher concentration of Zn^{2+} ions release, TaCaP_Zn6, and TaCaP_Zn7 samples, are the ones with more quantity of Zn NPs deposited, which comes in agreement with what is observed in the morphological analyses.

An important fact to take into consideration is that none of the Zn-containing samples exceeds the limit of toxicity of Zn^{2+} ions in the human body, which according to the literature corresponds to 10 $\mu\text{g}/\text{mL}$ (approximately 10 ppm) [12].

Considering the Zn^{2+} ions release profiles, as well as the NPs morphology, TaCaP_Zn4 and TaCaP_Zn7 samples are the samples selected to be further studied in order to understand the effect of the amount of Zn^{2+} ions released from the surfaces and the effect of the Zn nanoparticles' sizes and shapes on the surfaces' functional performance, since these are the samples with the lowest and the highest quantity of Zn NPs, as well as the more and the less homogeneous shaped NPs, comparing to the control.

Figure 24 presents SEM micrographs of the TaCaP_Zn4 and TaCaP_Zn7 samples. Through the observation of the micrographs, it is possible to observe that in both samples, the nanoparticles are present in the surface of the samples, as well as in the interior of the pores, without compromising the porous morphology achieved by the PEO technique (Figure 13 B).

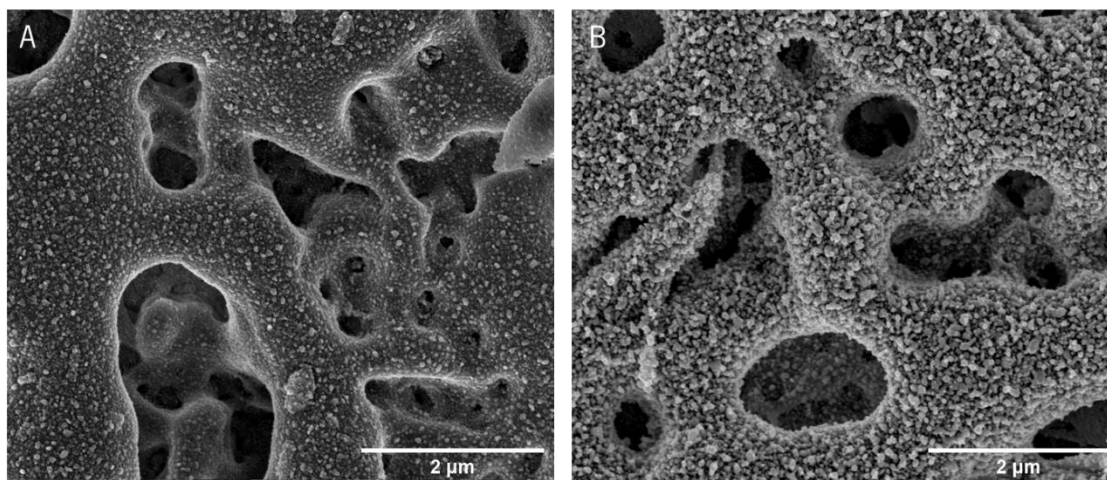


Figure 24 - SEM micrographs of A) TaCaP_Zn4 and B) TaCaP_Zn7 samples.

3.3. Deposition of a carbon layer over the optimized surfaces

As all the Zn-containing surfaces have the burst ion release in the first 24 h of immersion, a carbon layer is deposited over the Zn NPs of the selected samples (TaCaP_Zn4 and TaCaP_Zn7) to try to control and prolong the ionic release over the first 24 hours of immersion. The samples resulting from this process are named TaCaP_Zn4C and TaCaP_Zn7C.

To assess the impact of the carbon layer deposition on the porous morphology, SEM micrographs (Figure 25) of TaCaP_Zn4C, and TaCaP_Zn7C samples is presented below. It is possible to observe that the carbon layer encapsulates the NPs when compared with the TaCaP_Zn4 and TaCaP_Zn7 samples (Figure 24), without compromising their micro/nano-porous structure.

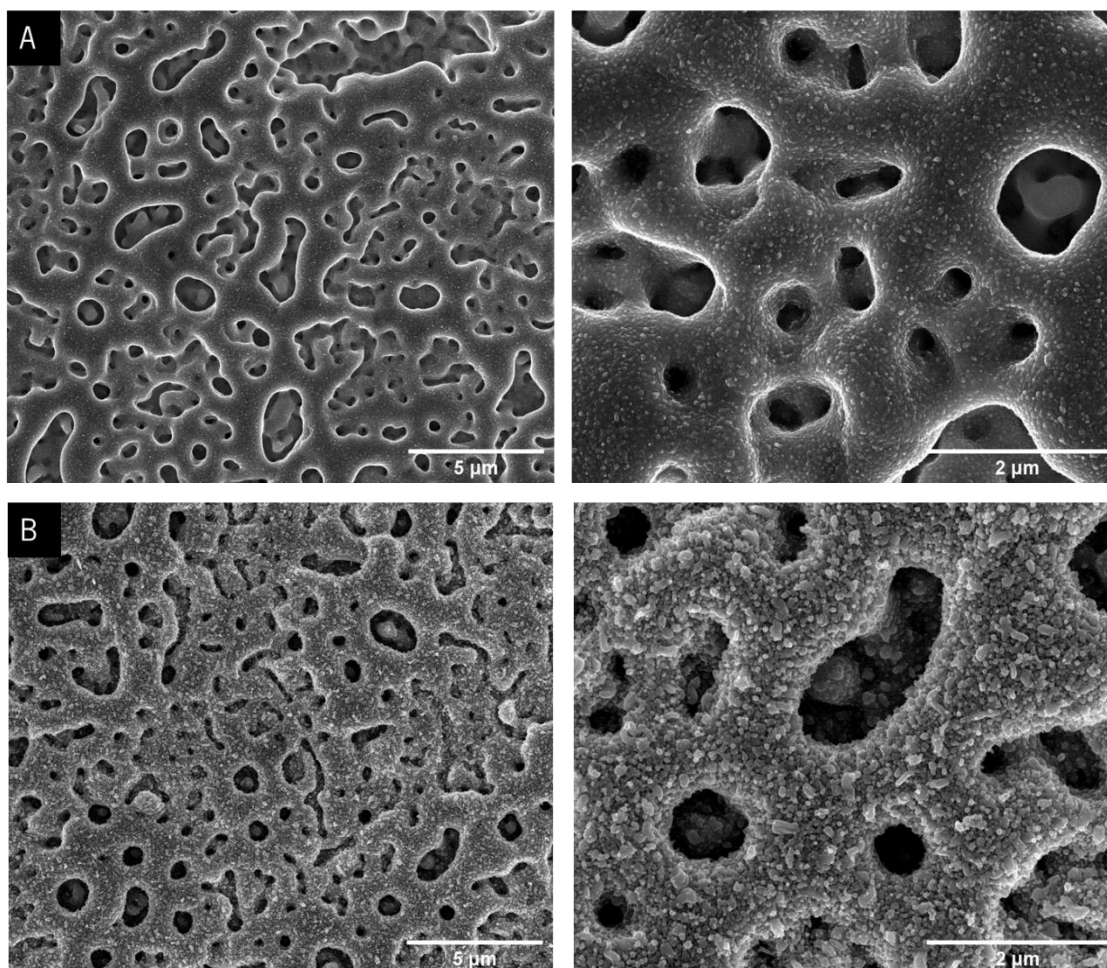


Figure 25 - SEM micrographs of A) TaCaP_Zn4C and B) TaCaP_Zn7C samples. Scale: 5 μm on the left and 2 μm on the right.

As the aim of the carbon layer deposited over the Zn NPs is to control the kinetics of Zn^{2+} release in the first hours of immersion, the ion release profiles of the carbon layered samples, evaluated by ICP-OES (Figure 26), is also analyzed.

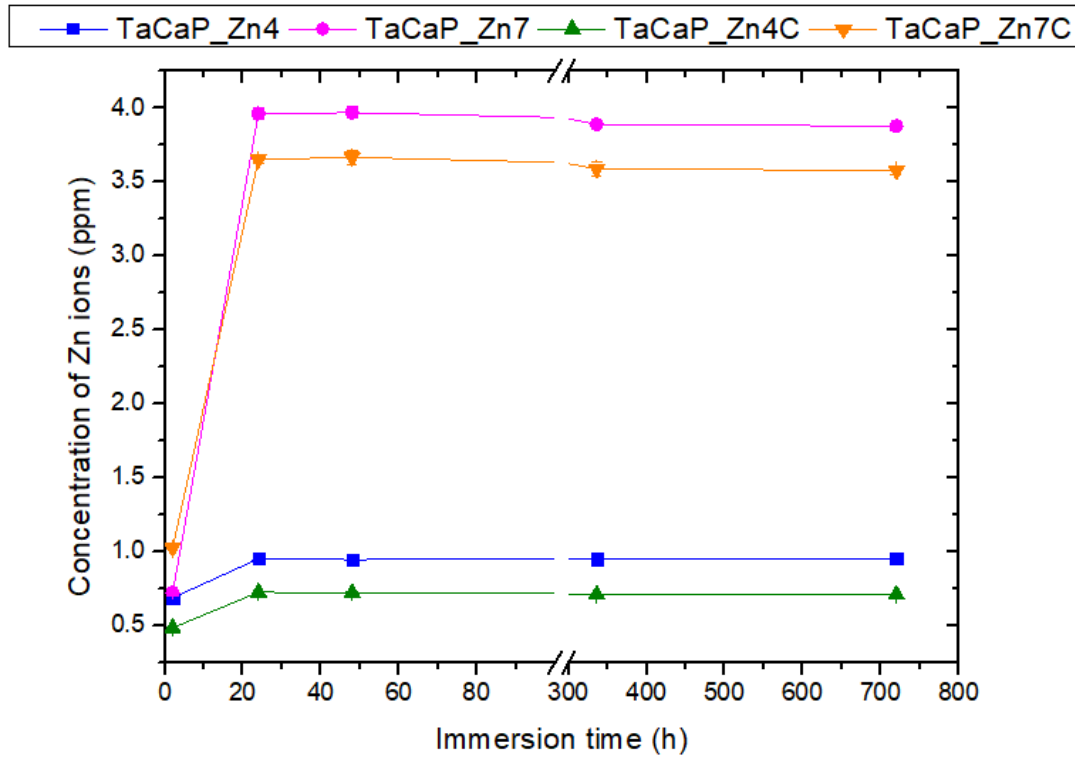


Figure 26 - Zn^{2+} ion release profile for TaCaP_Zn4, TaCaP_Zn4C, TaCaP_Zn7 and TaCaP_Zn7C samples.

Both the samples with (TaCaP_Zn4C and TaCaP_Zn7C) and without (TaCaP_Zn4 and TaCaP_Zn7) carbon layer show the same trend of Zn^{2+} ion release profile, with the largest amount of ions being released between the first 2 and 24 hours of immersion and no significant Zn^{2+} release being observed thereafter. The results also indicate that the carbon layer presence results in a decrease in the Zn^{2+} ions release, as the released zinc ions concentration is lower for Ta_CaP_D4C and Ta_CaP_Zn7C than for Ta_CaP_D4 and Ta_CaP_Zn7 samples, respectively, in every studied time-point during the 30 days of immersion in PBS. Thus, it suggests that some of the Zn NPs are still encapsulated by the C layer, however they not have mobility on the carbon layer meaning that they cannot be released.

3.5. Antimicrobial behavior

To access the antimicrobial capacity of the Zn-containing porous Ta_2O_5 surfaces, CFU technique, performed with *Candida albicans* fungus, is used. The study is performed using *Candida albicans* fungus since it is reported in the literature [71] that this fungus is commonly present in the oral

cavity and can trigger mucosa infections associated with the maintenance of peri-implantitis disease. Pereira-Silva *et al.* [72] studied the antifungal activity of ZnO thin films against *Candida albicans*, obtaining values of inhibition of viable cell growth of 58% and 68% compared to the glass lamella used as control, after 8h and 25h of incubation, respectively.

Figure 27 shows the cell viability of the Zn-containing surfaces at 5 and 24 hours of culture, and the TaCaP sample as control. The results reveal a significant reduction in the quantity of viable fungus in Zn-containing sample, compared to the control (TaCaP), both at 5 and 24 hours. At 5 hours of culture, the results reveal similar cell viability for all the Zn-containing samples, with a significant reduction in the number of viable cells when compared to the control. Regarding the results at 24 hours, it is verified a clear influence of the quantity of NPs in the reduction of the number of viable cells, with the TaCaP_Zn7 sample showing a lower quantity of viable cells compared with TaCaP_Zn4 sample's quantity, which is in agreement with the obtained results for the ionic release of Zn^{2+} ions in the ICP-OES (Figure 23 and Figure 26). Although there is no statistically significant difference between the respective surfaces, the carbon layered samples seem to demonstrate a slightly better antimicrobial behavior when compared with their equivalent sample without carbon layer, even though these samples have a lower quantity of Zn^{2+} ions released in the ICP-OES (Figure 26). Thus, the ionic release from the TaCaP-Zn7C is sufficient to guarantee a significant inhibition of the fungi growth. As it is well known, the chemical composition and the surface morphology have a strong influence on cell responses. Thus, a possible explanation for these results may be the fact that the carbon layer leads to partial mitigation of the pores at the nanoscale (Figure 25), which are preferential spots for cell growth, thus making it more difficult for the *C. albicans* to adhere and proliferate.

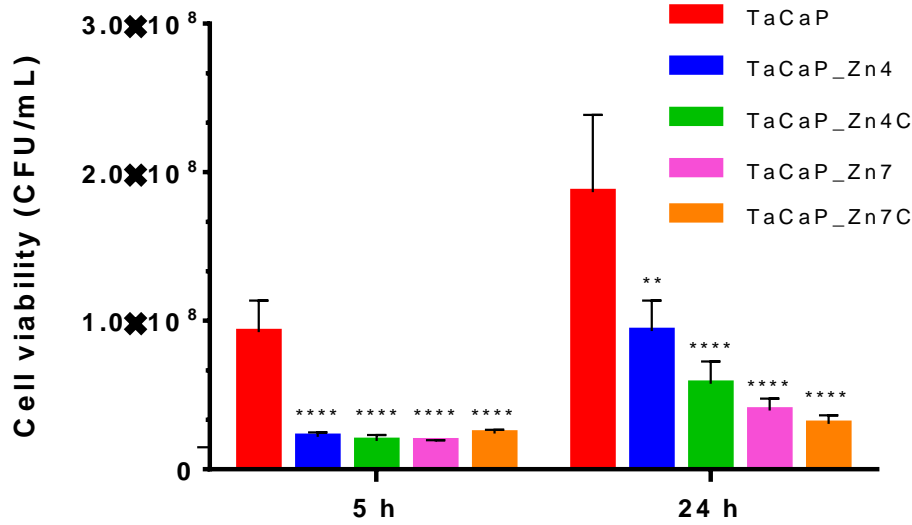


Figure 27 - Cell viability of *Candida albicans* after 5 and 24 h of incubation on TaCaP (control), TaCaP_Zn4, TaCaP_Zn4C, TaCaP_Zn8 and TaCaP_Zn8C surfaces. Significant values as * $p \leq 0.05$, ** $p \leq 0.01$, *** $p \leq 0.001$ and **** $p \leq 0.0001$, significant reduction compared to control (TaCaP surface).

To sum up, the results clearly demonstrate that the presence of the Zn NPs prevent the *Candida albicans* growth, which means that these samples are fungistatic. By increasing the amount of Zn NPs deposited onto the TaCaP surface the reduction of metabolic viable cells increases, which indicates that the higher Zn^{2+} ions release can be a possible antimicrobial mechanism. However, other mechanisms may also be responsible for the antimicrobial activity of the developed samples.

3.6. Corrosion behavior

Dental implants are subject to corrosion since the saliva can be a corrosive environment. Thus, selected samples (TaCaP, TaCaP_Zn4, TaCaP_Zn7, TaCaP_Zn4C, TaCaP_Zn7C), and untreated Ta sample (as a control), are subjected to potentiodynamic, open circuit potential (OCP) and electrochemical impedance spectroscopy (EIS) tests in artificial saliva for several time-points.

After the modification treatments that the Ta sheet suffers, the achieved surfaces exhibit changes that can be crucial for the OCP behavior. These changes are: the oxide formation, incorporation of Ca and P by the PEO functionalization; the amount and size of Zn NPs deposited on the surfaces of the samples, and finally the roughness achieved with the formation of micro/nano-porosity during the PEO process and by the deposition of Zn NPs and carbon layer. Figure 28 shows the

OCP value for each sample as a function of immersion time in artificial saliva, at 37 °C, after 2, 24, and 48 hours, 7 and 14 days.

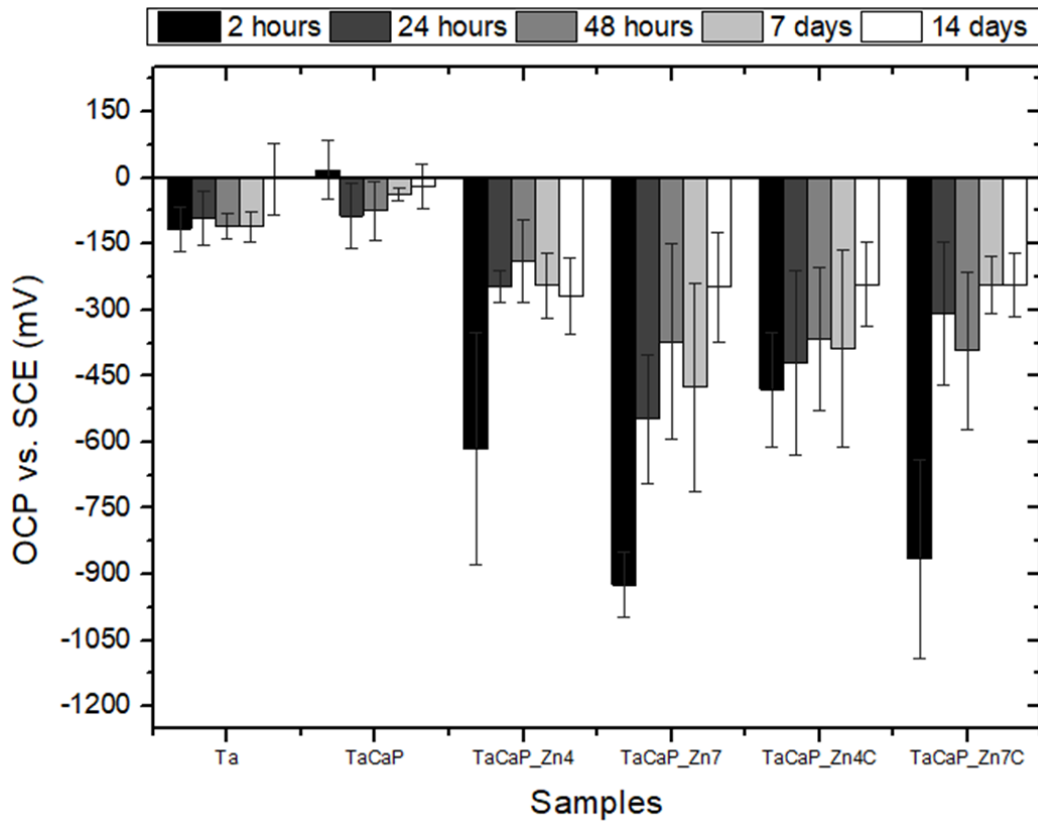


Figure 28 - OCP vs. SCE values for the 5 studied time-points.

Generally, all the samples exhibit a negative OCP. The Ta control sample reveals a constant OCP value between 2 hours and 7 days of immersion. At 14 days of immersion, a slight increase in OCP value is recorded, suggesting slight passivation of the surface. On the other hand, a decrease in OCP behavior is observed in the TaCaP sample between 2 and 24 hours of immersion, possibly related to the reactivity of the Ca^{2+} and PO_4^{3-} ions resulting from the Ca and P embedded into the oxide layer with the artificial saliva solution. From 24 hours to 14 days, the OCP value slightly increase and stabilize, indicating a slight improvement in the corrosion behavior of this sample. Generally, the addition of Zn NPs to the samples' surface leads to a clear decrease in the OCP values, meaning a worst corrosion behavior, which was expected as the Zn NPs are metallic elements. In the particular case of the TaCaP_Zn4 sample, a significant increase in OCP value is observed between 2 and 24 hours after immersion. Thereafter, the sample shows a tendency to stabilize the OCP values without showing significant differences in the remaining time-points. The

same tendency is observed for TaCaP_Zn7 and TaCaP_Zn7C samples. The increase in OCP values observed in these 3 samples between 2 and 24 hours after immersion could be attributed to the release of Zn NPs from the surface in this time interval with the electrolyte, as the largest amount of Zn^{2+} ions released from these surfaces, determined by ICP, occurs in this time interval (Figure 26). Therefore, the samples become less active. In opposite, TaCaP_Zn4C sample reveals a different corrosion behavior since the OCP value at 2 hours of immersion is higher than all the other Zn-containing samples and the increase in OCP value between 2 and 24 hours after immersion is much less significant than the other Zn-containing samples. This can be explained by the fact that, in this case, the carbon layer deposited over the Zn NPs may reduce the interaction between the NPs and the electrolyte, inhibiting the Zn^{2+} release, making the surface more inert due to the inert character of C. Although C is inert, the same effect is not verified in the TaCaP_Zn7C sample, where the effect of the interaction between the Zn NPs with the electrolyte is dominant and outweighs the effect of the C layer. This behavior may be related to the size and morphology of this sample's NPs (Figure 25 B), which are much larger and more irregular than those in the TaCaP_Zn4C sample (Figure 25 A).

As observed in Figure 13 B, the PEO treatment induces a porous structure with non-homogeneous distribution and dimension. Consequently, due to substrate heterogeneity, the deposition of the nanoparticles occurs in preferential nucleation points (Figure 24 A and B). Therefore, the heterogeneity of the surface explains the error values associated with the experimentally determined OCP values.

Figure 29 shows the plotted potentiodynamic curves of the analyzed samples immediately after immersion (0h) and after 14 days of immersion. Immediately after immersion (Figure 29 A), it is visible that the sample with the lowest current density rate (i_{corr}) is the TaCaP sample (red line), indicating that corrosion occurs at a lower rate on this surface when compared with the others. On the other hand, TaCaP_Zn7 is the sample that shows the highest current density (pink line), meaning that the corrosion rate is faster, probably due to the higher amount of Zn NPs in this samples when compared with the TaCaP_Zn4 sample. Comparing all the samples with the Ta control, it seems like the surface modification by PEO slows down the corrosion rate, while the deposition of NPs leads to an increase in the system electrochemical reactivity. The presence of the carbon layer slightly decreases the current densities of the coated samples in comparison with

the non-coated ones, which comes in agreement with the fact that the more inert C layer covers the NPs, observed by SEM (Figure 25). Regarding the corrosion resistance, estimated by the E_{corr} value of the potential *vs.* SCE, Ta and TaCaP samples are the ones with the best behavior, showing the higher values, which is expected and in agreement with the OCP behavior, since those are the only samples without metallic NPs on their surfaces. The potentiodynamic curves at 0 hours also reveal the existence of pitting corrosion on the TaCaP_Zn4, TaCaP_Zn7, and TaCaP_Zn7C samples.

After 14 days of immersion (Figure 29 B), Ta sample shows a slight improvement in the corrosion behavior, presenting a higher E_{corr} value and no significant change in the corrosion rate. On the other hand, TaCaP sample does not show significant changes in the corrosion rate, presenting nearly the same current density as at 0 hours of immersion, nor in the corrosion resistance, which may indicate that this sample is stable throughout the time. Furthermore, the potentiodynamic curves reveal clear changes either in terms of corrosion rate (I_{corr}), either in terms of corrosion resistance (E_{corr}) of the Zn-containing surfaces (TaCaP_Zn4, TaCaP_Zn7, TaCaP_Zn4C, and TaCaP_Zn7C). Indeed, after 14 days, Zn-containing surfaces present a more passive behavior (higher E_{corr} value) and a lower corrosion rate (lower I_{corr}) compared to the immediately after immersion curves (Figure 29 A). These results show that after 14 days of immersion, the Zn-containing samples tend to approximate their behavior to the behavior exhibited by the TaCaP sample, due to the loss of the Zn NPs throughout the immersion time, becoming less active. Moreover, the deposition of the C layer leads to a more significant improvement in the corrosion resistance of the TaCaP_Zn4C and TaCaP_Zn7C samples after 14 days of immersion, when compared to the improvement achieved by the TaCaP_Zn4 and TaCaP_Zn7 samples.

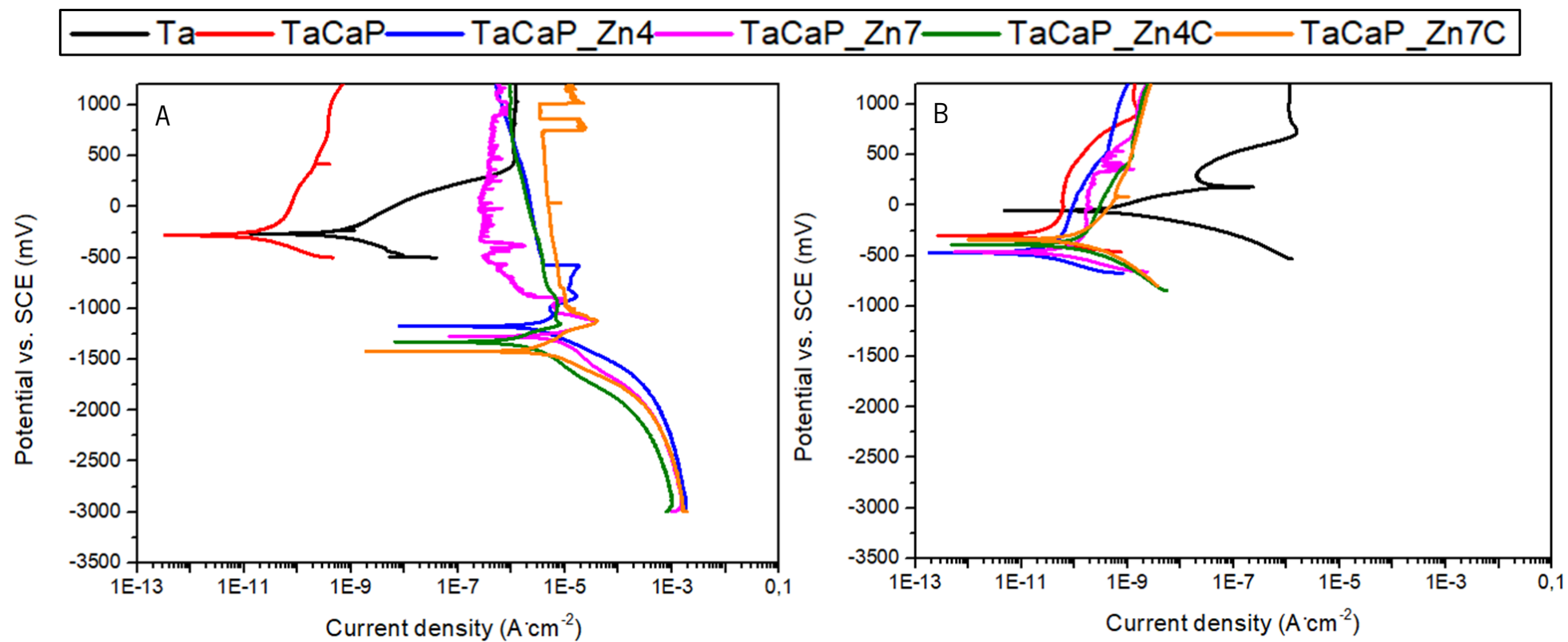


Figure 29 – Potentiodynamic curves A) immediately after immersion (0h) and B) 14 days after immersion.

To characterize in detail the corrosion performance of the samples, electrochemical impedance spectroscopy is performed. Bode and Nyquist plots for all the developed samples, as well as a Ta control sample, after 2, 24 and 48 hours, 7 and 14 days of immersion in artificial saliva are presented from Figure 30 to Figure 32 and in Figure 33, respectively. It is important to notice that for the first 2 hours of test, the TaCaP_Zn7 and TaCaP_Zn7C samples are not represented, because, in all the 3 replicas tested, for that time of test the system is not capable to reach a stabilized point to take any conclusion on the corrosion behavior of these samples.

Generally, Ta control sample shows a capacitive behavior with a single time constant while TaCaP sample shows 2-time constants through all the studied immersion times, as it is possible to see in the Bode plots from Figure 30. Furthermore, it is possible to observe that both samples do not suffer much significant changes on their impedance modulus ($|Z|$) as the immersion time increases, indicating that these samples are already electrochemically stable before the EIS experiment starts, specially the TaCaP sample, which presents higher values of impedance modulus, thus indicating a better electrochemical response from this sample. Such fact may be explained by the formation of the oxide layer promoted by the PEO technique.

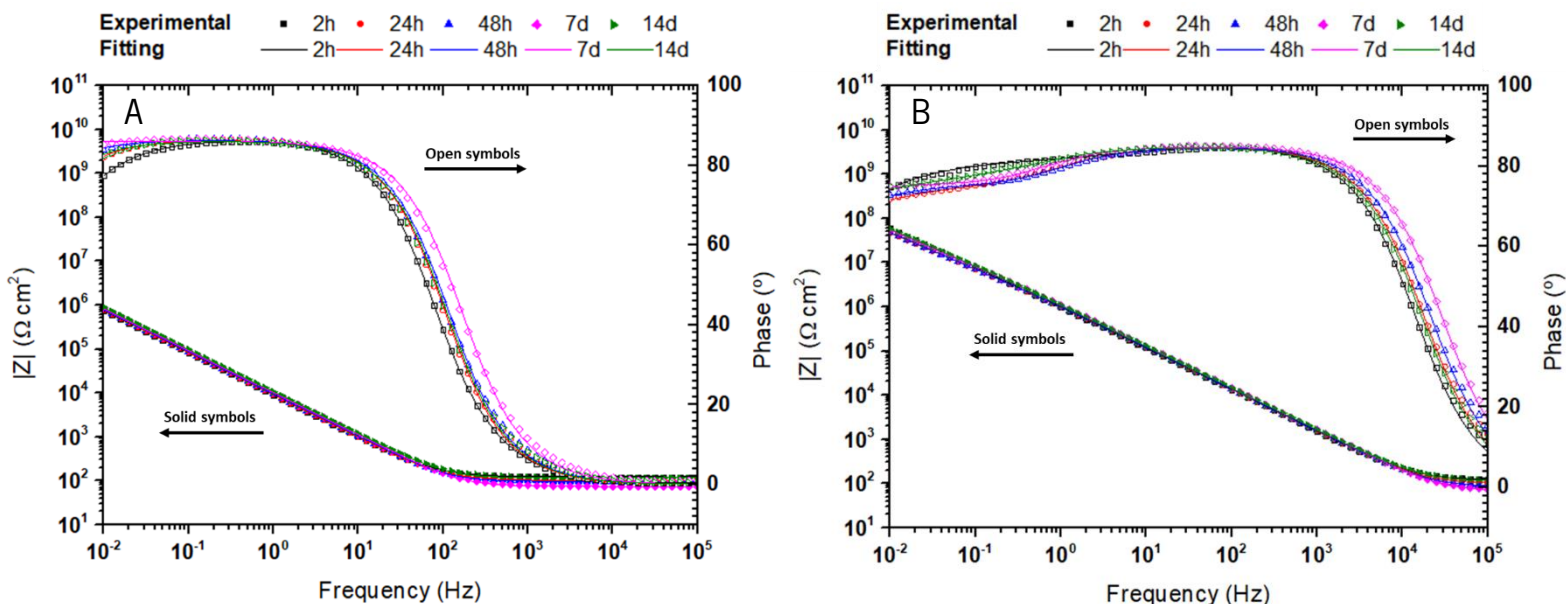


Figure 30 - Bode plot of A) Ta and B) TaCaP samples after 2, 24, and 48 hours, 7 and 14 days of immersion in artificial saliva at 37°C. (Measured (symbols) and fitted (lines) values of impedance modulus are related to the left axis while the measured (symbols) and fitted (lines) values of phase are related to the right axis).

Analyzing the Bode graphs from Figure 31 and Figure 32 is possible to see that the samples with Zn NPs and the samples with Zn NPs and carbon layer show different behaviors compared with

the Ta control and TaCaP samples, as well as along the immersion time. For the 2 and 24 hours of immersion, TaCaP_Zn4 sample (Figure 31 A) shows a diffusional behavior and after 48h of immersion, shows a 2-time constants behavior until the 14 days of immersion. This transitional behavior after the first 24 hours of immersion in saliva can be related with the results obtained in the ICP-OES (Figure 26), once after the first 24 hours of immersion in PBS there is no more significant release of Zn^{2+} ions from this surface, indicating that after those 24 hours of immersion this sample returns to its ground state (TaCaP). This results also confirm the conclusions taken by the potentiodynamic curves analysis for this sample. On the other hand, although TaCaP_Zn4C sample (Figure 31 B) shows a similar kinetics of Zn^{2+} ion releasing as the TaCaP_Zn4 sample in the ICP-OES (Figure 26), this sample only shows diffusional behavior in the first 2 hours of immersion, becoming represented by 2-time constants afterwards. The faster release of Zn NPs in this case may be due to the fact that the ICP and the corrosion tests are performed using two different solutions, which, combined with the encapsulation of the NPs by the carbon layer, can affect the kinetics of ions releasing. Regarding the electrochemical response of these two samples, an improvement is achieved as a function of the immersion time, with $|Z|$ values increasing throughout the immersion time. After 14 days of immersion the electrochemical response of these two samples achieves values close to the ones of TaCaP sample, thus indicating once again the approximation of these surfaces to their ground state as the NPs were being released from their surface.

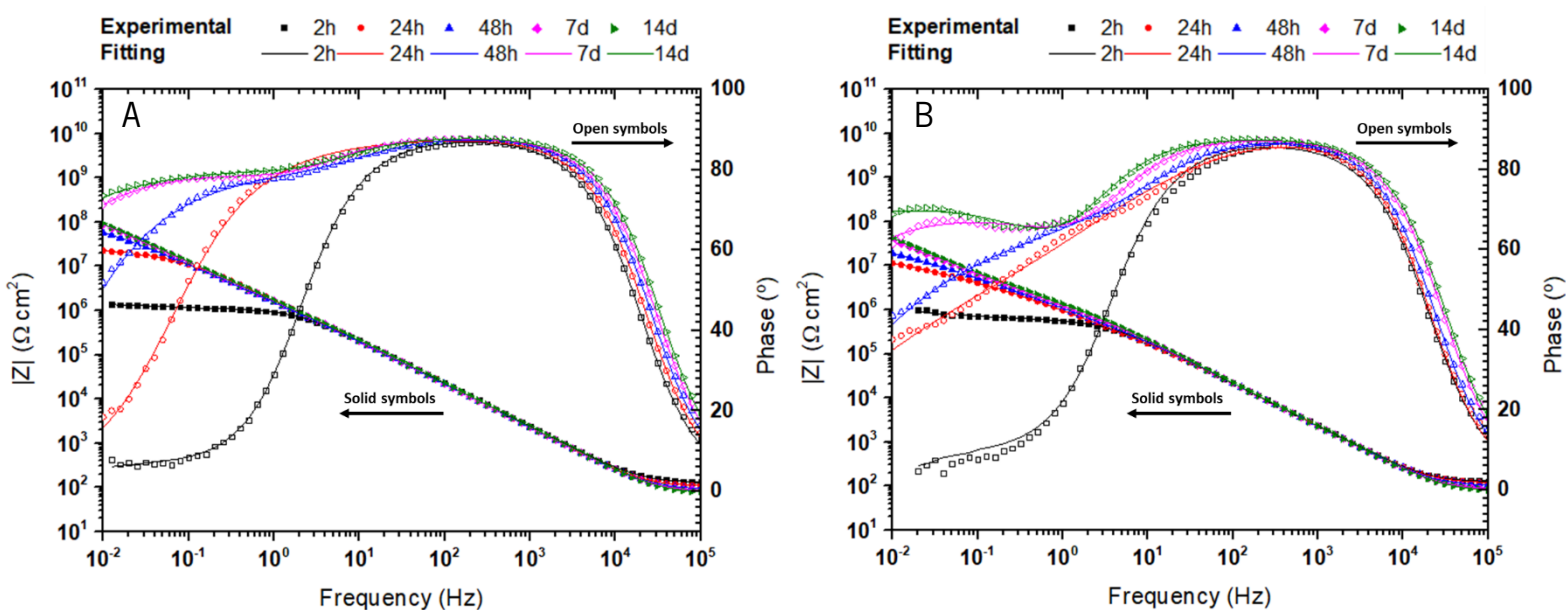


Figure 31 - Bode plot of A) TaCaP_Zn4 and B) TaCaP_Zn4C samples after 2, 24, and 48 hours, 7 and 14 days of immersion in artificial saliva at 37°C. (Measured (symbols) and fitted (lines) values of impedance modulus are related to the left axis while the measured (symbols) and fitted (lines) values of phase are related to the right axis).

TaCaP_Zn7 (Figure 32 A) sample also presents diffusion at 24 hours of immersion and 2-time constants afterwards, like the TaCaP_Zn4 sample. Despite the 7 days of immersion curve (pink curve) seems to show diffusional behavior, the high α_2 value (0.86 ± 0.10) presented on Table 6, indicates that there is no need to fit this curve using a W component, since the α_2 is high enough to not consider the effect of diffusion (normally considered for $\alpha_2 \approx 0.6$) in this time point. On the other hand, TaCaP_Zn7C (Figure 32 B) sample shows diffusion along all the immersion time, which somehow suggests that some Zn NPs remain in the surface after 14 days of immersion. Such theory can be confirmed by this sample's SEM micrographs (Figure 40). In terms of impedance modulus, firstly at 24 hours of immersion, TaCaP_Zn7 and TaCaP_Zn7C samples show similar electrochemical behaviors between themselves, secondly, generally, their impedance modulus values increase throughout the immersion time. These results indicate a clear improvement on the corrosion behavior of the samples with NPs (TaCaP_Zn4 and TaCaP_Zn7) and with NPs and C layer (TaCaP_Zn4C and TaCaP_Zn7C) as a function of immersion time, with their behavior becoming more capacitive throughout the immersion time due to the Zn NPs release.

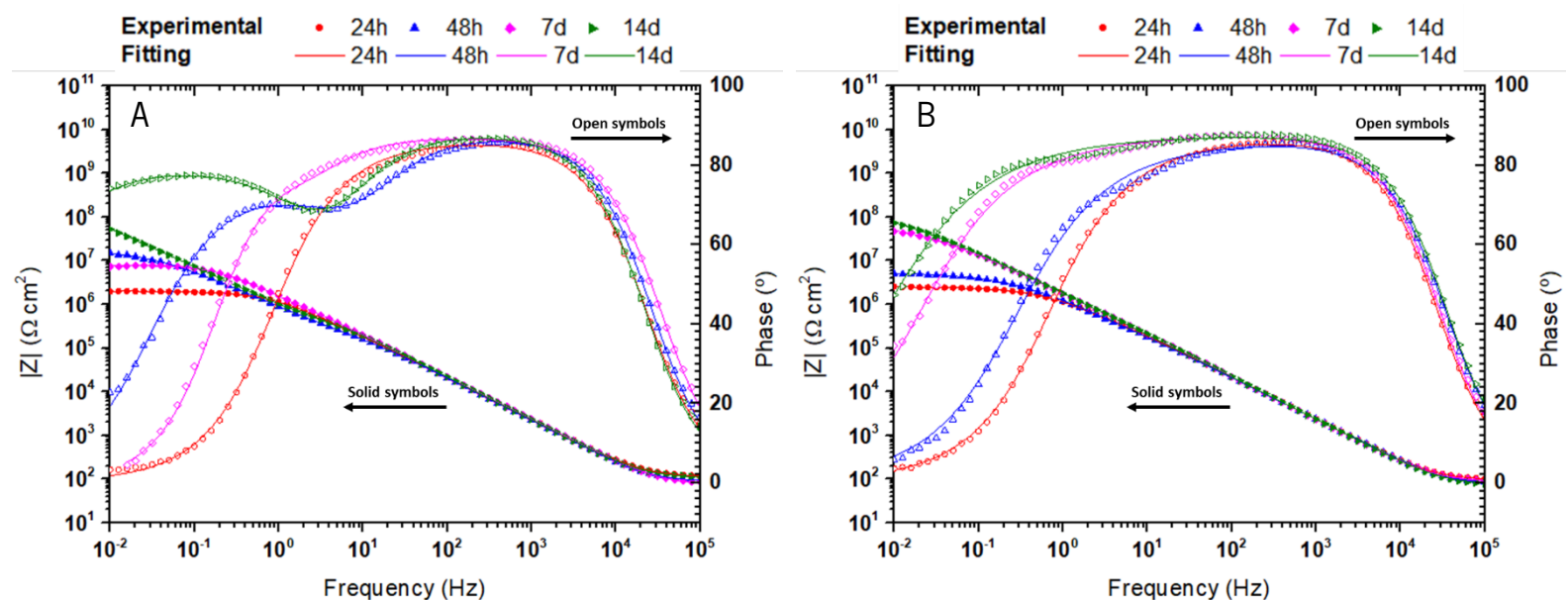


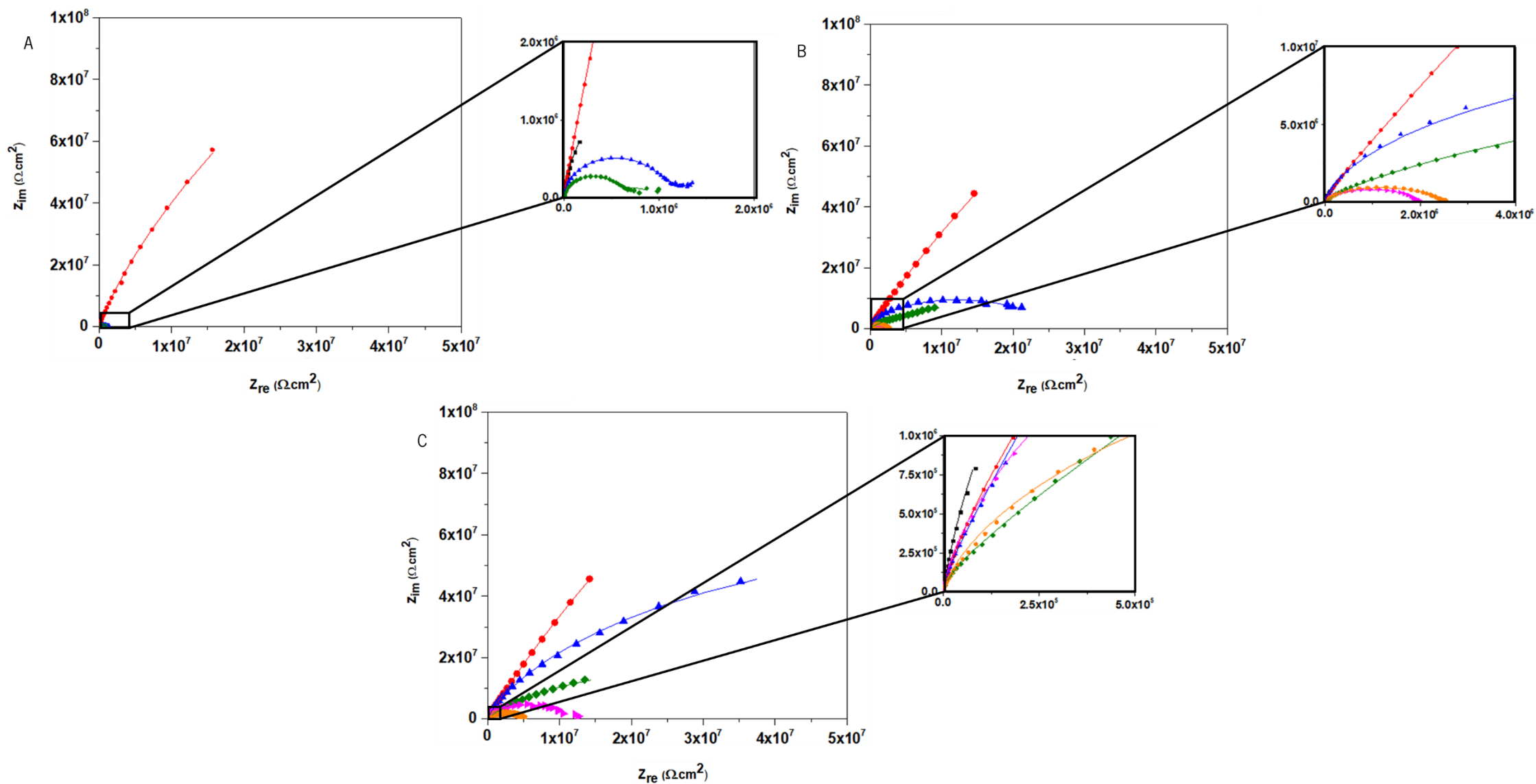
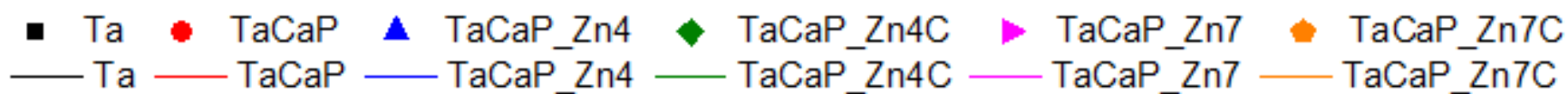
Figure 32 - Bode plot of A) TaCaP_Zn7 and B) TaCaP_Zn7C samples after 2, 24, and 48 hours, 7 and 14 days of immersion in artificial saliva at 37°C. (Measured (symbols) and fitted (lines) values of impedance modulus are related to the left axis while the measured (symbols) and fitted (lines) values of phase are related to the right axis).

Regarding the impedance, in particular after the first 2 hours of immersion, Nyquist plot (Figure 33 A) reveals that the sample with the largest impedance is the TaCaP sample, proving the surface treatment benefit in corrosion enhancement, since the non-treated Ta control sample shows lower

impedance values. On the other hand, the samples with lower impedance values are the TaCaP_Zn4 and TaCaP_Zn4C samples, which is somehow expected as the NPs are electrochemical active metallic elements even though they have a pristine passive oxide layer. In good agreement, after 24 hours of immersion (Figure 33 B), TaCaP_Zn7 and TaCaP_Zn7C samples are the ones that show lower values of impedance thus, being the samples less resistant to corrosion. Such fact may be explained by the largest amount of Zn NPs present in these surfaces. On the other hand, as the immersion time increases (Figure 33 C to E), it is possible to see a stable behavior on the TaCaP sample impedance values, and an improvement on the corrosion resistance of the Zn-containing and the Zn-containing with C layer samples. TaCaP_Zn4 sample shows the greatest improvement of all samples, presenting much higher values of impedance from 48h of immersion to 14 days, when compared with the values at 2 and 24 hours of immersion.

As it was explained before, the Zn NPs are deposited on the surfaces to enhance their antimicrobial response. Such objective is achieved, with the samples with more quantity of Zn²⁺ NPs (TaCaP_Zn7 and TaCaP_Zn7C) being the ones showing greater antimicrobial activity (Figure 27). However, as it is accessed by the different corrosion tests performed, the introduction of Zn NPs on the surfaces leads to a worst corrosion behavior immediately after immersion, with their corrosion behavior improving as a function of the immersion time, which is related with the release of the NPs from the surfaces. Thus, it is possible to conclude that, if on one hand the introduction of Zn NPs has a positive influence on the antimicrobial behavior of the developed surfaces, on the other hand it has a negative influence on the surfaces' corrosion behavior. With that said, it is important to find a balance between the antimicrobial capacity and corrosion response of the surfaces, in order to try to assure a good performance of the surfaces either in biological behavior, either in corrosion resistance.

Experimental
Fitting



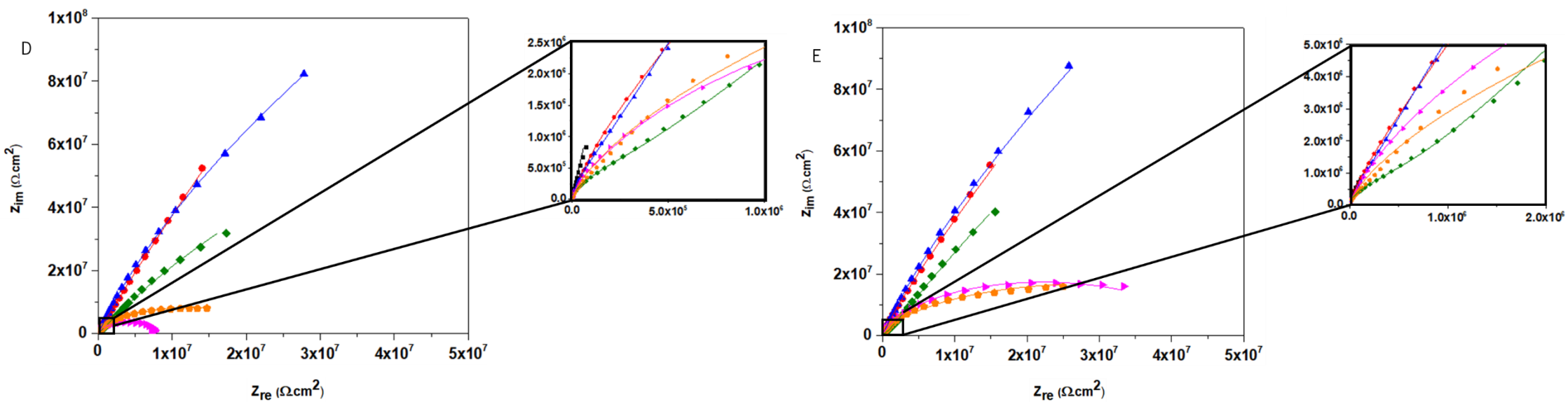


Figure 33 - Nyquist plot of Ta, TaCaP, TaCaP_Zn4, TaCaP_Zn4C, TaCaP_Zn7 and TaCaP_CaP7C samples after A) 2 hours, B) 24 hours, C) 48 hours, D) 7 days, and E) 14 days of immersion in artificial saliva at 37°C.

Figure 34 to Figure 36 show the equivalent circuits (EC) used to fit the EIS results. Figure 34 represents the circuit used to fit the Ta control sample. In this circuit, already reported in the literature by other authors that study tantalum corrosion [73][74], a constant phase element (CPE) is used instead of a capacitance element to consider the roughness and heterogeneities of the surface. In the used EC, the R_{sol} element represents the resistance of the electrolyte, while the polarization resistance element, R_i , represents the charge transfer resistance. Thus, the parallel connection between the CPE and the R_p elements represents the resistance and capacitance of the passive oxide film formed on the Ta surface. To fit the EIS results of the TaCaP sample, a circuit traditionally used by other authors to model porous surfaces [55][73][75] (Figure 35) is used. In this case, the R_1 and Q_1 elements in parallel represent the interaction of the oxide layer formed by PEO with the electrolyte, while the R_2 and Q_2 elements, also placed in parallel, illustrate the substrate (Ta sheet). As Zn NPs and the carbon layer are added, it becomes more difficult to represent the behavior of such complex systems, as well as the circuits used to fit results within the same sample that also change throughout the different time-points studied due to the Zn NPs release. Regarding the TaCaP_Zn4 sample, for 2 and 24 hours of immersion, the used circuit (Figure 36) has a Warburg element (W) substituting the second CPE (Q_2) element present in the previously described circuit (Figure 35) to model the diffusion that occurs between the Zn NPs and the electrolyte. Afterwards, the EIS results are fitted using the same circuit as the TaCaP sample, because the diffusion effect of the NPs is no longer determinant, which may indicate that after the first 24 hours of immersion, the surface no longer releases NPs in significant quantities. The adopted approach of two different circuits before and after the first 24 hours of immersion is in good agreement with the ICP-OES results (Figure 26). When the carbon layer is added over the NPs (sample TaCaP_Zn4C), the same two circuits are used to fit the EIS results. However, the circuit from Figure 36 is only used to model the results from the first 2 hours of immersion because the effect of the diffusion between the NPs and the electrolyte is only observed at this time-point, afterwards the circuit used to fit the results is the same as TaCaP sample. EIS results for the first 2 hours of immersion from TaCaP_Zn7 and TaCaP_Zn7C samples are not possible to fit since any of the 3 replicas analyzed shown a constant behavior, indicating that for these two samples, at this time-point, the system is not stable yet. Regarding the results for the remaining time-points, TaCaP_Zn7 sample shows a similar response as the TaCaP_Zn4 sample's response, with the circuit from Figure 36 being used to model this sample's behavior at 24 hours and the circuit from Figure 35 being used model the remaining time-points. On the other hand, all the EIS results from

TaCaP_Zn7C samples are fitted using Figure 36 circuit, once the diffusional effect is observed along every time-point. This behavior indicates again that after 14 days of immersion this sample's surface still has nanoparticles. Thus, the SEM results (Figure 40) prove that after 14 days of immersion the carbon layer is still encapsulating some Zn NPs, controlling its release, which is a possible explanation why this sample shows a lower release of Zn^{2+} ions than the TaCaP_Zn7 sample after 14 days of immersion in PBS on the ICP-OES analysis.

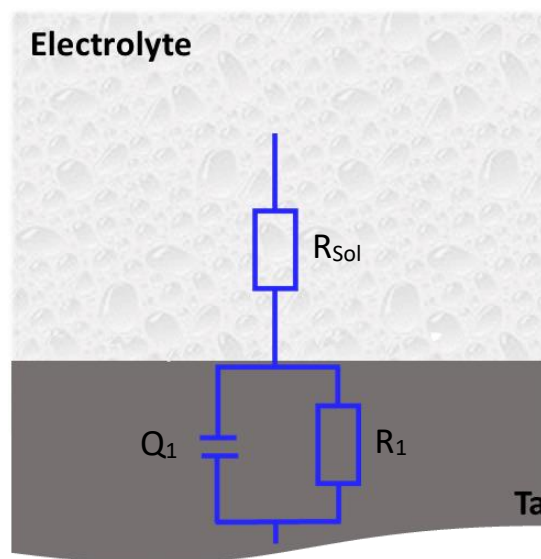


Figure 34 - Equivalent circuit used to fit Ta sample's EIS values.

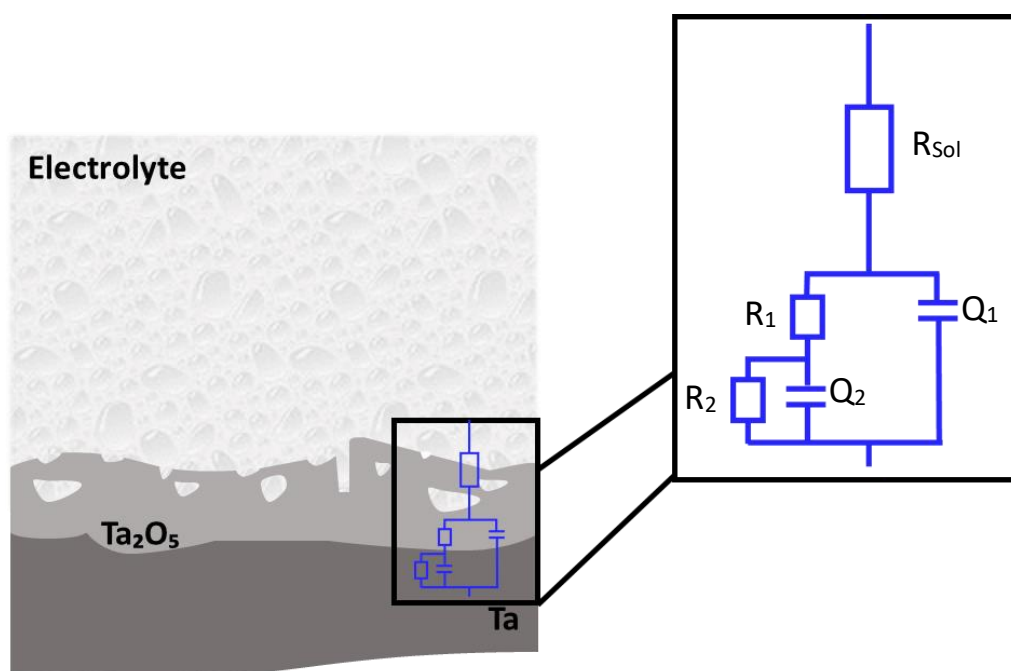


Figure 35 - Equivalent circuit used to fit EIS values of TaCaP sample and some time-points of TaCaP_Zn4, TaCaP_Zn4C and TaCaP_Zn7 samples.

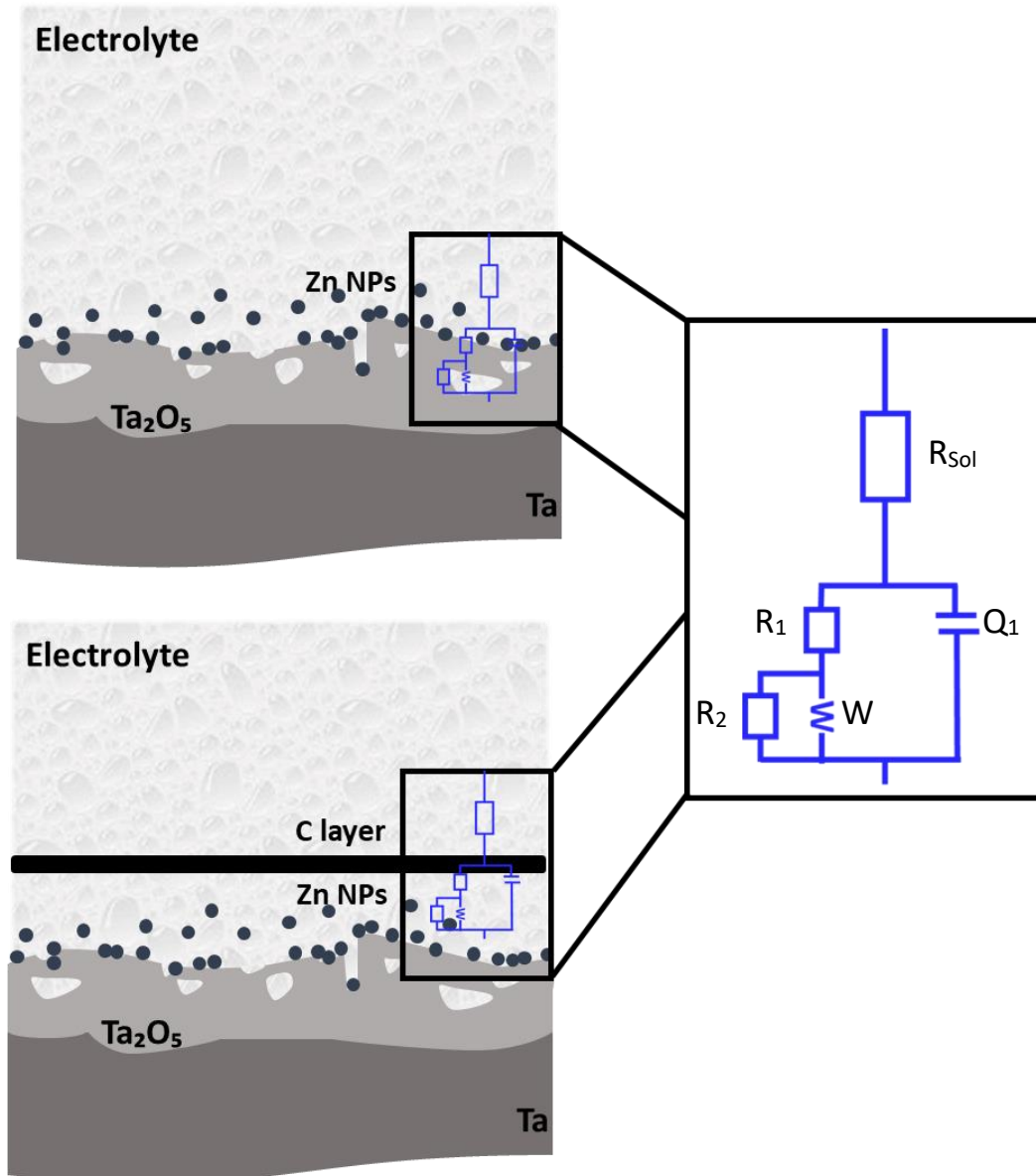


Figure 36 - Equivalent circuit used to fit EIS values of TaCaP_Zn7C sample and some time-points of TaCaP_Zn4, TaCaP_Zn4C and TaCaP_Zn7 samples.

Table 3 to Table 7 present the EIS data fitting results for every time-point studied. All the samples, for every time-point, present a goodness of fit in the order of 10^{-4} , except for the TaCaP_Zn7C sample at 24 hours and 14 days of immersion, which presents values of 2.28×10^{-3} and 1.33×10^{-3} respectively, which are still considered good fitting values. Regarding the resistance of the electrolyte, represented by R_{sol} , it is possible to observe on the tables that, generally, it has the tendency to decrease as the immersion time increases for every studied sample. On the other hand, the polarization resistance (R_p), given by the value of R_1 for the Ta control sample, and by the sum of R_1 with R_2 for all the other samples, shows a tendency to increase as a function of the

immersion time, with R_p values from the TaCaP sample standing out when compared to all the other samples' values. This indicates the tendency for the samples' corrosion resistance to improve as a function of the immersion time. Thus, this behavior comes in agreement with what was concluded with the potentiodynamic curves analysis (Figure 29), where the sample with better corrosion behavior is the TaCaP and the Zn-containing and C layered samples improve their behavior after 14 days of immersion.

Table 3 - EIS fitting parameters after 2 hours of immersion.

	Ta	TaCaP	TaCaP_Zn4	TaCaP_Zn4C
R_{sol} ($\Omega \cdot \text{cm}^2$)	120 ± 2	122 ± 1	125 ± 3	126 ± 4
R₁ ($M\Omega \cdot \text{cm}^2$)	10.5 ± 4.4	8.3 ± 4.4	0.6 ± 0.4	0.7 ± 0.2
Q₁ ($\text{nF}/\text{s}\alpha \cdot \text{cm}^2$)	17 ± 1	132 ± 37	86 ± 5	93 ± 3
α	0.96 ± 0.00	0.96 ± 0.02	0.97 ± 0.01	0.97 ± 0.00
R₂ ($G\Omega \cdot \text{cm}^2$)	-	1.02 ± 0.18	0.0005 ± 0.0001	0.0008 ± 0.0003
Q₂ ($\text{nF}/\text{s}\alpha \cdot \text{cm}^2$)	-	22 ± 9	-	-
α^2	-	0.71 ± 0.03	-	-
W ($M\Omega \cdot \text{cm}^2/\text{s}^{0.5}$)	-	-	0.26 ± 0.12	0.13 ± 0.05
$< \chi^2 \times 10^{-4}$	1.54	1.47	8.56	9.16
R_p ($M\Omega \cdot \text{cm}^2$)	10.5	1028.3	1.1	1.5

Table 4 - EIS fitting parameters after 24 hours of immersion.

	Ta	TaCaP	TaCaP_Zn4	TaCaP_Zn4C	TaCaP_Zn7	TaCaP_Zn7C
R_{sol} ($\Omega \cdot \text{cm}^2$)	105 ± 3	103 ± 2	100 ± 5	113 ± 4	109 ± 2	105 ± 9
R₁ ($M\Omega \cdot \text{cm}^2$)	12.2 ± 1.9	3.9 ± 2.4	0.9 ± 0.3	0.6 ± 0.4	0.2 ± 0.1	0.2 ± 0.1
Q₁ ($\text{nF}/\text{s}\alpha \cdot \text{cm}^2$)	18 ± 1	138 ± 29	95 ± 11	85 ± 4	92 ± 4	93 ± 6
α	0.96 ± 0.00	0.95 ± 0.01	0.97 ± 0.01	0.98 ± 0.00	0.97 ± 0.01	0.98 ± 0.01
R₂ ($G\Omega \cdot \text{cm}^2$)	-	1.30 ± 0.54	0.028 ± 0.001	0.023 ± 0.014	0.003 ± 0.001	1.00 ± 1.00
Q₂ ($\text{nF}/\text{s}\alpha \cdot \text{cm}^2$)	-	79 ± 16	-	170 ± 84	-	-
α^2	-	0.69 ± 0.02	-	0.66 ± 0.15	-	-
W ($M\Omega \cdot \text{cm}^2/\text{s}^{0.5}$)	-	-	10.71 ± 7.45	-	5.29 ± 5.25	4.10 ± 3.56
$< \chi^2 \times 10^{-4}$	2.57	1.09	5.49	4.03	8.25	22.8
R_p ($M\Omega \cdot \text{cm}^2$)	12.2	1303.9	28.9	23.6	3.2	1000.2

Table 5 - EIS fitting parameters after 48 hours of immersion.

	Ta	TaCaP	TaCaP_Zn4	TaCaP_Zn4C	TaCaP_Zn7	TaCaP_Zn7C
R_{sol} ($\Omega \cdot \text{cm}^2$)	98 ± 2	85 ± 1	85 ± 6	98 ± 4	63 ± 27	89 ± 11
R₁ ($M\Omega \cdot \text{cm}^2$)	25.5 ± 3.6	4.4 ± 2.1	0.8 ± 0.3	0.8 ± 0.4	0.2 ± 0.2	0.6 ± 0.4
Q₁ (nF/s$\alpha \cdot \text{cm}^2$)	18 ± 1	139 ± 27	90 ± 9	86 ± 4	70 ± 20	92 ± 5
α	0.96 ± 0.01	0.95 ± 0.01	0.97 ± 0.01	0.98 ± 0.00	0.81 ± 0.17	0.97 ± 0.01
R₂ ($G\Omega \cdot \text{cm}^2$)	-	1.81 ± 0.12	0.11 ± 0.05	0.057 ± 0.002	0.014 ± 0.002	0.014 ± 0.008
Q₂ (nF/s$\alpha \cdot \text{cm}^2$)	-	73 ± 9	-	141 ± 53	115 ± 46	-
α^2	-	0.69 ± 0.00	-	0.72 ± 0.13	0.89 ± 0.11	-
W ($M\Omega \cdot \text{cm}^2/\text{s}^{-0.5}$)	-	-	-	-	-	14.11 ± 6.92
$< \chi^2 \times 10^{-4}$	2.75	1.67	1.26	1.65	5.40	7.67
R_p ($M\Omega \cdot \text{cm}^2$)	25.5	1814.4	110.8	57.8	14.2	14.6

Table 6 - EIS fitting parameters after 7 days of immersion.

	Ta	TaCaP	TaCaP_Zn4	TaCaP_Zn4C	TaCaP_Zn7	TaCaP_Zn7C
R_{sol} ($\Omega \cdot \text{cm}^2$)	86 ± 4	68 ± 1	101 ± 20	71 ± 12	73 ± 4	78 ± 9
R₁ ($M\Omega \cdot \text{cm}^2$)	36.7 ± 3.9	11.1 ± 0.1	2.0 ± 0.7	1.3 ± 0.2	1.6 ± 1.2	0.8 ± 0.5
Q₁ (nF/s$\alpha \cdot \text{cm}^2$)	16 ± 1	127 ± 31	88 ± 7	86 ± 3	87 ± 3	88 ± 3
α	0.95 ± 0.00	0.96 ± 0.02	0.97 ± 0.01	0.98 ± 0.00	0.98 ± 0.01	0.97 ± 0.00
R₂ ($G\Omega \cdot \text{cm}^2$)	-	14.96 ± 4.23	0.54 ± 0.40	0.49 ± 0.08	0.004 ± 0.001	0.056 ± 0.025
Q₂ (nF/s$\alpha \cdot \text{cm}^2$)	-	37 ± 15	59 ± 11	120 ± 39	109 ± 60	-
α^2	-	0.64 ± 0.06	0.68 ± 0.06	0.78 ± 0.07	0.86 ± 0.10	-
W ($M\Omega \cdot \text{cm}^2/\text{s}^{-0.5}$)	-	-	-	-	-	16.37 ± 7.88
$< \chi^2 \times 10^{-4}$	2.29	6.10	0.57	1.24	5.83	9.66
R_p ($M\Omega \cdot \text{cm}^2$)	36.7	14971.1	542.0	491.3	5.6	56.8

Table 7 - EIS fitting parameters after 14 days of immersion.

	Ta	TaCaP	TaCaP_Zn4	TaCaP_Zn4C	TaCaP_Zn7	TaCaP_Zn7C
R_{sol} ($\Omega \cdot \text{cm}^2$)	114 \pm 2	114 \pm 2	92 \pm 18	68 \pm 8	113 \pm 5	62 \pm 11
R₁ ($M\Omega \cdot \text{cm}^2$)	16.6 \pm 2.0	11.4 \pm 1.1	0.7 \pm 0.7	1.3 \pm 0.5	0.7 \pm 0.1	0.9 \pm 0.5
Q₁ ($\text{nF}/\text{s}\alpha \cdot \text{cm}^2$)	16 \pm 1	127 \pm 33	81 \pm 2	87 \pm 4	84 \pm 1	88 \pm 2
α	0.95 \pm 0.00	0.96 \pm 0.02	0.98 \pm 0.00	0.98 \pm 0.00	0.98 \pm 0.00	0.97 \pm 0.00
R₂ ($G\Omega \cdot \text{cm}^2$)	-	18.70 \pm 0.87	1.44 \pm 0.36	1.74 \pm 0.87	0.32 \pm 0.27	0.14 \pm 0.07
Q₂ ($\text{nF}/\text{s}\alpha \cdot \text{cm}^2$)	-	28 \pm 10	53 \pm 9	103 \pm 43	86 \pm 44	-
α^2	-	0.62 \pm 0.02	0.70 \pm 0.03	0.80 \pm 0.06	0.74 \pm 0.09	-
W ($M\Omega \cdot \text{cm}^2/\text{s}^{-0.5}$)	-	-	-	-	-	20.10 \pm 9.96
$\chi^2 \times 10^{-4}$	3.40	0.78	1.27	1.27	1.05	13.3
R_p ($M\Omega \cdot \text{cm}^2$)	16.6	18711.4	1440.7	1741.3	320.7	140.9

To understand the effect of the corrosion tests on the morphology and chemical composition of the samples, SEM and EDS analyses of the TaCaP_Zn7 and TaCaP_Zn7C samples are presented below.

Figure 37 A shows SEM micrographs of TaCaP_Zn7 sample after the potentiodynamic test performed immediately after immersion. It is possible to see that the porous morphology does not suffer significant changes after the test, while the nanoparticles seem to have changed morphology and agglomerate, looking very different from what they look like before the corrosion test (Figure 19). Furthermore, EDS spectra of Z1 and Z2 (Figure 37 B and C respectively) prove that the structures observed in the SEM micrographs are Zn structures, since Zn is detected in the spectrum (Z1), and that there is no longer Zn in the porous structures (Z2).

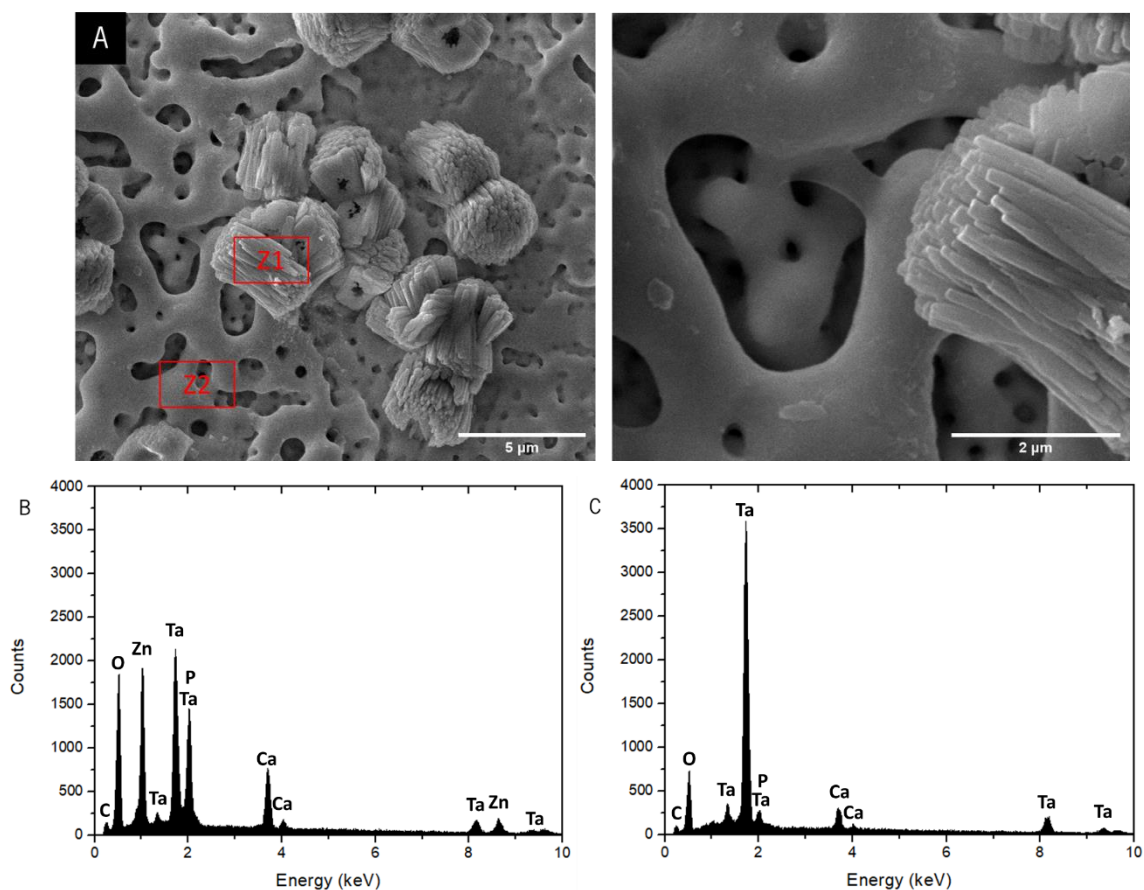


Figure 37 – A) SEM micrographs of TaCaP_Zn7 sample after the potentiodynamic test immediately after immersion (scale: 5 μm on the left and 2 μm on the right), and EDS spectra of B) Z1 and C) Z2.

After 14 days of immersion in artificial saliva and after the OCP, EIS, and potentiodynamic tests, TaCaP_Zn7 sample's SEM micrographs (Figure 38) show that this sample returns to its ground

state (porous structure without Zn NPs). Thus, these results come in agreement with the results obtained from the potentiodynamic (Figure 29) and EIS (Figure 32 A) tests, where after 14 days of immersion this sample's corrosion behavior become similar to TaCaP sample's behavior.

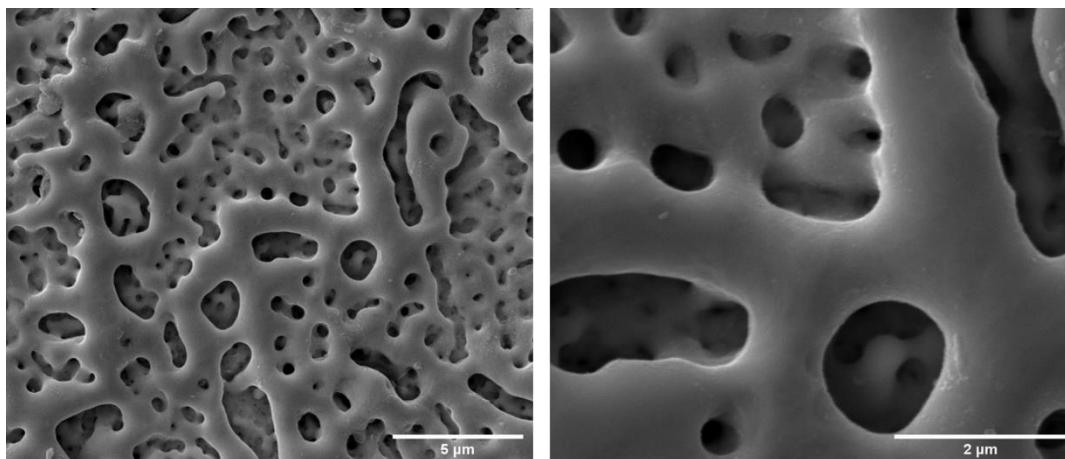


Figure 38 - SEM micrographs of TaCaP_Zn7 sample after the potentiodynamic, OCP and EIS tests 14 days after immersion (scale: 5 μm on the left and 2 μm on the right).

Regarding the TaCaP_Zn7C sample, after the potentiodynamic test immediately after immersion, SEM micrographs (Figure 39 A) also demonstrate some tendency for the nanoparticles to agglomerate, however, their morphology is completely different from TaCaP_Zn7 sample's morphology (Figure 37 A), which may be due to their encapsulation by the carbon layer that may lead to the constraining of their mobility. Furthermore, EDS spectra from two different zones of this sample's surface (Figure 39 B and C) reveal that there is yet Zn distributed over all the surface, meaning a Carbon layer's partial successful role on the control of the NPs release.

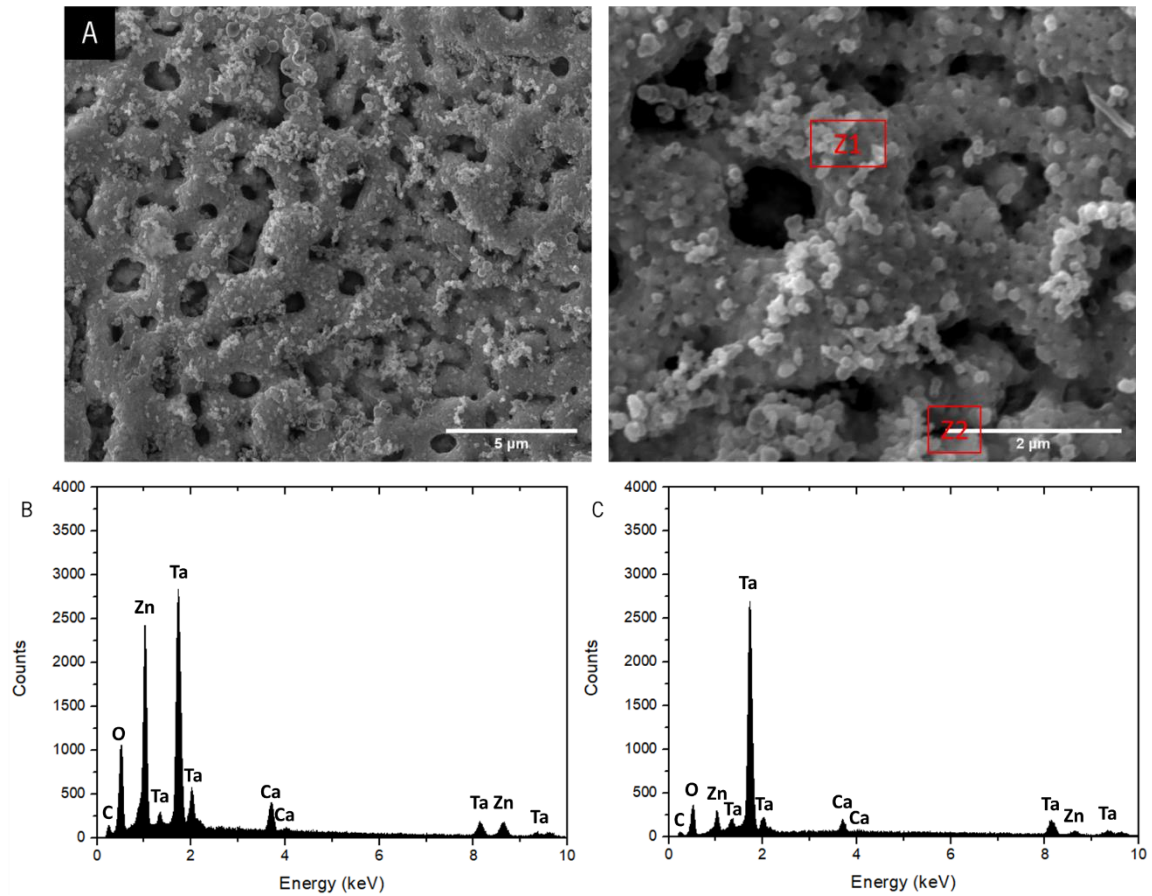


Figure 39 - A) SEM micrographs of TaCaP_Zn7C sample after the potentiodynamic test immediately after immersion (scale: 5 µm on the left and 2 µm on the right), and EDS spectra of B) Z1 and C) Z2.

SEM micrographs of a TaCaP_Zn7C sample after 14 days of immersion in saliva and the corrosion tests (Figure 40) show the existence of some Zn particles still in this sample's surface. Such fact can explain why this sample presents diffusional behavior on the EIS results from 2 hours until 14 days of immersion (Figure 32 B), unlike all the other analyzed samples.

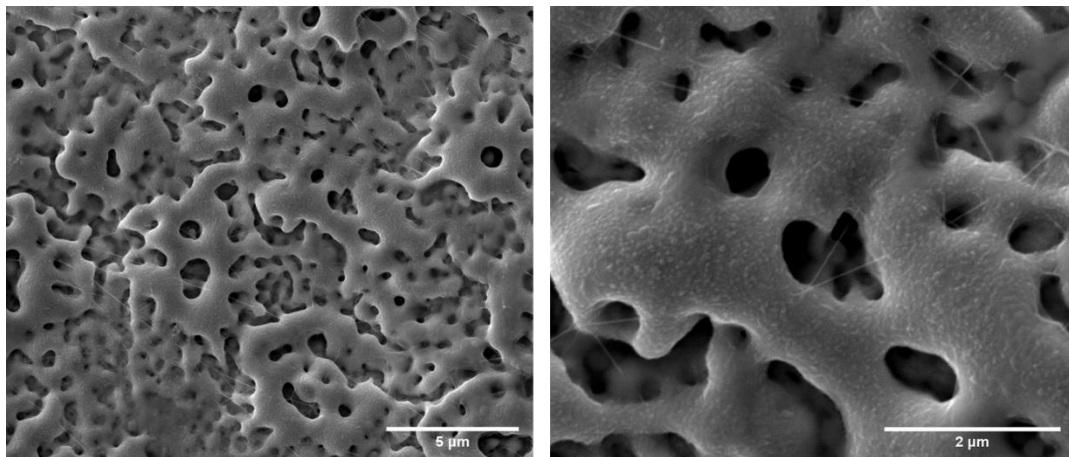


Figure 40 - SEM micrographs of TaCaP_Zn7C sample after the potentiodynamic, OCP and EIS tests 14 days after immersion (scale: 5 µm on the left and 2 µm on the right).

Chapter 4

Conclusions e Future Work

In this chapter the overall conclusion of this dissertation, as well as the discussion of the future works to be performed to complement and deepen the study carried out in this dissertation are presented.

In this study, different amount of Zn NPs, with and without a thin C layer, were deposited onto micro/nano-porous Ta surfaces, to develop antimicrobial surfaces to be used as biomaterial for dental implants. The micro/nano-porous Ta surfaces were produced by PEO, performed on high-purity Ta sheets. The Zn NPs were deposited, by magnetron sputtering, onto the porous Ta surfaces, with several different sets of deposition conditions being used to achieve surfaces with different Zn NPs' quantities, and consequently morphologies and sizes. The NPs depositions that allowed the higher amount of Zn NPs with the highest zinc ions release and a lower amount of Zn NPs with the low Zn ions release were selected as optimized samples, to better understand the influence of the amount and morphology of Zn NPs in the surfaces' antimicrobial response and corrosion resistance. Posteriorly, a thin C layer was deposited over the two optimized samples, by magnetron sputtering. The samples were characterized by morphological, chemical, and functional techniques, in order to assess their morphological and chemical properties, as well as their antimicrobial and corrosion performances.

PEO technique was proven to be successful, since the morphological and chemical characterization of the developed samples proved the existence of porous structures and incorporation of osteoconductive elements (Ca and P) onto their surfaces. Thus, the PEO allowed the development of surfaces morphological and chemically similar to the human bone. The magnetron sputtering technique, performed under different deposition conditions, allowed the deposition of Zn NPs in different contents, sizes and morphologies, as it was proven by morphological characterization. ICP-OES technique gave a quantitative characterization of the sputtered samples in terms of Zn^{2+} ions release, allowing the choice of the samples with the highest and lowest quantity of Zn. Furthermore, chemical characterization confirmed the presence of C layer where the C layer was sputtered.

ICP-OES results from both Zn-containing samples covered or not by the C layer showed that the C layer influenced the quantity of Zn^{2+} ions released from the samples, since it acts as barrier layer inhibiting the ions release, comparing with the equivalent sample without C layer.

The antimicrobial ability was assessed by CFU. The obtained results proved that the presence and quantity of Zn in the surfaces had a strong influence on the quantity of viable cells, since all the Zn-containing samples revealed capacity to inhibit the cell growth (fungistatic), in both 5 and 24 hours of cell culture. The samples with highest quantity of Zn (higher Zn ions release) are the ones that showed the greatest reduction on the quantity of viable cells after 24 h of culture. Furthermore,

it was proven that the C layer did not significantly affect the antimicrobial capacity of the samples, translating that the lower ions release did not impair the antimicrobial performance of these Zn- and C-containing surfaces.

Corrosion tests demonstrated that, generally, PEO technique positively influenced the corrosion behavior of the anodized samples, due to the growth of the oxide layer. On the other hand, the addition of Zn NPs negatively influenced the corrosion behavior of the studied samples, since the NPs are electrochemical active metallic elements. However, the results also demonstrated the tendency for the Zn-containing and Zn-containing and C layered samples to improve their corrosion response as the immersion time in artificial saliva increased, with their behavior becoming similar to the one demonstrated by the PEO-treated Ta surface. Thus, it is possible to conclude that has the Zn NPs were released, the antimicrobial capacity of the samples increased while the corrosion behavior improved.

As future work, the performance of complementary biological tests to better understand the mechanism (or mechanisms) responsible for the antimicrobial capacity of the developed samples would be interesting. It is important to prove that these surfaces are not cytotoxic of osteoblastic cells and that they promote the cellular responses (protein adsorption, cell proliferation and differentiation). Furthermore, the study of the mechanical properties, such as elastic modulus and fracture strength, of the developed samples would be important to guarantee the mechanical resistance of these surfaces. Although the corrosion behavior had already been accessed in this work, the study of the surfaces' tribocorrosion, using a chewing simulation system to simulate the chewing process with different pH corrosive environments, would also be a good way to better understand the potential of usage of the developed surfaces' modifications on actual dental implants. In addition, in order to highlight the achievements reached under this thesis, two scientific papers, whose first drafts are proposed in Annex 2: First Draft of Paper 1 and Annex 3: First Draft of Paper 2, will be submitted to ISI journals.

References

- [1] S. Pires, "Incorporação de Ca, P e Mg em óxido de Ta nanoestruturado para acelerar a osteointegração em implantes dentários," dissertação apresentada à Universidade do Minho para obtenção do grau de Mestre em Engenharia de Materiais, 2016.
- [2] P. L. Casado, R. R. Guerra, M. A. Da Fonseca, L. C. Costa, J. M. Granjeiro, and E. P. Barboza, "Tratamento das doenças peri-implantares: Experiências passadas e perspectivas futuras - Uma revisão da literatura," *Braz J Periodontol*, vol. 21, no. 02, pp. 25–35, 2011.
- [3] A. Rokn, H. Aslroosta, S. Akbari, H. Najafi, F. Zayeri, and K. Hashemi, "Prevalence of peri-implantitis in patients not participating in well-designed supportive periodontal treatments: a cross-sectional study," *Clin. Oral Implants Res.*, vol. 28, no. 3, pp. 314–319, 2017.
- [4] J. Oliveira, "Deposition of Zn-ZnO nanoparticles by magnetron sputtering onto tantalum substrates," dissertação apresentada à Universidade do Minho para obtenção do grau de Mestre em Engenharia de Materiais, 2017.
- [5] C. F. Almeida Alves, S. V. Calderón, D. Dias, and S. Carvalho, "Influence of Oxygen content on the electrochemical behavior of Ta1-xOx coatings," *Electrochim. Acta*, vol. 211, pp. 385–394, 2016.
- [6] C. F. Almeida Alves, A. Cavaleiro, and S. Carvalho, "Bioactivity response of Ta1-xOx coatings deposited by reactive DC magnetron sputtering," *Mater. Sci. Eng. C*, vol. 58, pp. 110–118, 2016.
- [7] V. K. Balla et al., "Tantalum - A Bioactive Metal for Implants," *JOM*, vol. 62, no. 7, pp. 61–64, 2010.
- [8] C. J. Frandsen, K. S. Brammer, K. Noh, G. Johnston, and S. Jin, "Tantalum coating on TiO₂ nanotubes induces superior rate of matrix mineralization and osteofunctionality in human osteoblasts," *Mater. Sci. Eng. C*, vol. 37, no. 1, pp. 332–341, 2014.
- [9] Y. Liu, C. Bao, D. Wismeijer, and G. Wu, "The physicochemical/biological properties of porous tantalum and the potential surface modification techniques to improve its clinical application in dental implantology," *Mater. Sci. Eng. C*, vol. 49, no. 14, pp. 323–329, 2015.
- [10] F. Oliveira, "Biofunctionalization of titanium surfaces for dental implants : osteogenic , anti-microbial and tribocorrosion resistant surfaces," tese apresentada à Universidade do Minho para obtenção do grau de Doutor em Engenharia Biomédica, 2015.
- [11] R. Bai *et al.*, "Metallic antibacterial surface treatments of dental and orthopedic materials," *Materials (Basel)*, vol. 13, no. 20, pp. 1–21, 2020.
- [12] A. Sirelkhatim *et al.*, "Review on zinc oxide nanoparticles: Antibacterial activity and toxicity mechanism," *Nano-Micro Lett.*, vol. 7, no. 3, pp. 219–242, 2015.
- [13] Z. R. Zhou and J. Zheng, "Tribology of dental materials: A review," *J. Phys. D. Appl. Phys.*, vol. 41, no. 11, 2008.
- [14] A. Bentes, "Desgaste de Materiais Dentários de Restauro Direto," dissertação

apresentada à Universidade do Minho para obtenção do grau de Mestre em Engenharia Biomédica, 2014.

- [15] R. Lewis and R. S. Dwyer-Joyce, "Wear of human teeth: a tribological perspective," *Proc. I MECH E Part J J. Eng. Tribol.*, vol. 219, no. 1, pp. 2–19, 2005.
- [16] Y. Oshida, E. B. Tuna, O. Aktören, and K. Gençay, "Dental implant systems," *Int. J. Mol. Sci.*, vol. 11, no. 4, pp. 1580–1678, 2010.
- [17] C. A. Alves, "Desenvolvimento de revestimentos nanoestruturados para implantes osteointegrados," dissertação apresentada à Universidade do Minho para obtenção do grau de Mestre em Engenharia de Materiais, 2013.
- [18] C. N. Elias and L. Meirelles, "Improving osseointegration of dental implants," *Expert Rev. Med. Devices*, vol. 7, no. 2, pp. 241–256, 2010.
- [19] C. M. Abraham, "A Brief Historical Perspective on Dental Implants, Their Surface Coatings and Treatments," *Open Dent. J.*, vol. 8, no. 1, pp. 50–55, 2014.
- [20] Associated Brånemark Osseointegration Centers, "Osseointegration," 2010. [Online]. Available: <https://branemark.se/osseointegration/>.
- [21] J. Li, J. A. Jansen, X. F. Walboomers, and J. J. van den Beucken, "Mechanical aspects of dental implants and osseointegration: A narrative review," *J. Mech. Behav. Biomed. Mater.*, vol. 103, no. November 2018, p. 103574, 2020.
- [22] T. Albrektsson and C. Johansson, "Osteoinduction, osteoconduction and osseointegration," *Eur. Spine J.*, vol. 10, pp. S96–S101, 2001.
- [23] and R. J. M. Y. Wang, Y. Zhang, "Health, Maintenance, and Recovery of Soft Tissues around Implants," *Clin. Implant Dent. Relat. Res.*, vol. 18, pp. 618–634, 2016.
- [24] R. Dimitriou and G. C. Babis, "Biomaterial osseointegration enhancement with biophysical stimulation," *J. Musculoskelet. Neuronal Interact.*, vol. 7, no. 3, pp. 253–265, 2007.
- [25] A. F. Mavrogenis, R. Dimitriou, J. Parvizi, and G. C. Babis, "Biology of implant osseointegration," *J. Musculoskelet. Neuronal Interact.*, vol. 9, no. 2, pp. 61–71, 2009.
- [26] M. Plecko *et al.*, "Osseointegration and biocompatibility of different metal implants - A comparative experimental investigation in sheep," *BMC Musculoskelet. Disord.*, vol. 13, pp. 1–12, 2012.
- [27] M. Gutierrez, M. Ascensão Lopes, N. Sooraj Hussain, A. Trigo Cabral, L. Almeida, and J. Domingos Santos, "Substitutos ósseos: Conceitos gerais e estado actual," *Arq. Med.*, vol. 19, no. 4, pp. 153–162, 2005.
- [28] M. Saini, "Implant biomaterials: A comprehensive review," *World J. Clin. Cases*, vol. 3, no. 1, p. 52, 2015.
- [29] L. Pinto, "Tratamento Químico Da Superfície De Implantes De Titânio," dissertação apresentada ao Instituto Militar de Engenharia para obtenção do grau de Mestre em Ciências dos Materiais, 2006.
- [30] K. Subramani and R. T. Mathew, *Titanium Surface Modification Techniques for Dental Implants-From Microscale to Nanoscale*, First Edit. Elsevier Inc., 2012.

- [31] R. Lucas, "Fatores que afetam a osteointegração dos implantes – Uma Revisão," vol. 1, 2013.
- [32] S. Sakka, K. Baroudi, and M. Z. Nassani, "Factors associated with early and late failure of dental implants," *J. Investig. Clin. Dent.*, vol. 3, no. 4, pp. 258–261, 2012.
- [33] M. Esposito, J.-M. Hirsch, U. Lekholm, and P. Thomsen, "Biological factors contributing three major determinants for late implant failures in the Brånemark system," *Eur J Oral Sci Eur J Oral Sci Eur J Oral Sci*, vol. 106, no. 106, pp. 527–551, 1998.
- [34] F. Javed, H. Ahmed, R. Crespi, and G. Romanos, "Role of primary stability for successful osseointegration of dental implants: Factors of influence and evaluation," *Interv. Med. Appl. Sci.*, vol. 5, no. 4, pp. 162–167, 2013.
- [35] L. Le Guéhennec, A. Soueidan, P. Layrolle, and Y. Amouriq, "Surface treatments of titanium dental implants for rapid osseointegration," *Dent. Mater.*, vol. 23, no. 7, pp. 844–854, 2007.
- [36] K. Subramani, S. Lavenus, J. Rozé, G. Louarn, and P. Layrolle, "Impact of nanotechnology on dental implants," *Emerg. Nanotechnologies Dent. Second Ed.*, no. February, pp. 83–97, 2018.
- [37] S. A. Alves, "A new concept of bio-multifunctional nanotubular surfaces for dental implants: tribocorrosion resistant, antibacterial and osteogenic," tese apresentada à Universidade do Minho para obtenção do grau de Doutora em Engenharia Biomédica, 2017.
- [38] L. G. Harris and R. G. Richards, "Staphylococci and implant surfaces: a review," *Injury*, vol. 37, no. 2 SUPPL., 2006.
- [39] G. Manivasagam, D. Dhinasekaran, and A. Rajamanickam, "Biomedical Implants: Corrosion and its Prevention - A Review," *Recent Patents Corros. Sci.*, vol. 2, no. 1, pp. 40–54, 2010.
- [40] S. Virtanen, I. Milošev, E. Gomez-Barrena, R. Trebše, J. Salo, and Y. T. Konttinen, "Special modes of corrosion under physiological and simulated physiological conditions," *Acta Biomater.*, vol. 4, no. 3, pp. 468–476, 2008.
- [41] J. C. M. Souza *et al.*, "How do titanium and Ti6Al4V corrode in fluoridated medium as found in the oral cavity? An in vitro study," *Mater. Sci. Eng. C*, vol. 47, pp. 384–393, 2015.
- [42] M. A. Khan, R. L. Williams, and D. F. Williams, "The corrosion behaviour of Ti-6Al-4V, Ti-6Al-7Nb and Ti-13Nb-13Zr in protein solutions," *Biomaterials*, vol. 20, no. 7, pp. 631–637, 1999.
- [43] R. Menini, M.-J. Dion, S. K. V. So, M. Gauthier, and L.-P. Lefebvre, "Surface and Corrosion Electrochemical Characterization of Titanium Foams for Implant Applications," *J. Electrochem. Soc.*, vol. 153, no. 1, p. B13, 2006.
- [44] V. K. Balla, S. Bodhak, S. Bose, and A. Bandyopadhyay, "Porous tantalum structures for bone implants: Fabrication, mechanical and in vitro biological properties," *Acta Biomater.*, vol. 6, no. 8, pp. 3349–3359, 2010.

- [45] L. Fialho, C. F. Almeida Alves, L. S. Marques, and S. Carvalho, "Development of stacked porous tantalum oxide layers by anodization," *Appl. Surf. Sci.*, vol. 511, no. August 2019, p. 145542, 2020.
- [46] T. Hanawa, "Research and development of metals for medical devices based on clinical needs," *Sci. Technol. Adv. Mater.*, vol. 13, no. 6, 2012.
- [47] T. W. Clyne and S. C. Troughton, "A review of recent work on discharge characteristics during plasma electrolytic oxidation of various metals," *Int. Mater. Rev.*, vol. 64, no. 3, pp. 127–162, 2019.
- [48] R. Rasouli, A. Barhoum, and H. Uludag, "A review of nanostructured surfaces and materials for dental implants: Surface coating, patterning and functionalization for improved performance," *Biomater. Sci.*, vol. 6, no. 6, pp. 1312–1338, 2018.
- [49] C. S. Dunleavy, I. O. Golosnoy, J. A. Curran, and T. W. Clyne, "Characterisation of discharge events during plasma electrolytic oxidation," *Surf. Coatings Technol.*, vol. 203, no. 22, pp. 3410–3419, 2009.
- [50] S. D. Wu, H. Zhang, X. D. Dong, C. Y. Ning, A. S. L. Fok, and Y. Wang, "Physicochemical properties and in vitro cytocompatibility of modified titanium surfaces prepared via micro-arc oxidation with different calcium concentrations," *Appl. Surf. Sci.*, vol. 329, pp. 347–355, 2015.
- [51] M. Sowa *et al.*, "Influence of process parameters on plasma electrolytic surface treatment of tantalum for biomedical applications," *Appl. Surf. Sci.*, vol. 407, pp. 52–63, 2017.
- [52] L. Fialho and S. Carvalho, "Surface engineering of nanostructured Ta surface with incorporation of osteoconductive elements by anodization," *Appl. Surf. Sci.*, vol. 495, no. July, p. 143573, 2019.
- [53] Y. Wang, H. Yu, C. Chen, and Z. Zhao, "Review of the biocompatibility of micro-arc oxidation coated titanium alloys," *Mater. Des.*, vol. 85, pp. 640–652, 2015.
- [54] L. Zhang and T. J. Webster, "Nanotechnology and nanomaterials: Promises for improved tissue regeneration," *Nano Today*, vol. 4, no. 1, pp. 66–80, 2009.
- [55] A. C. Alves, I. Sendão, E. Ariza, F. Toptan, P. Ponthiaux, and A. M. P. Pinto, "Corrosion behaviour of porous Ti intended for biomedical applications," *J. Porous Mater.*, vol. 23, no. 5, pp. 1261–1268, 2016.
- [56] B. Wopenka and J. D. Pasteris, "A mineralogical perspective on the apatite in bone," *Mater. Sci. Eng. C*, vol. 25, no. 2, pp. 131–143, 2005.
- [57] R. A. Surmenev, M. A. Surmeneva, and A. A. Ivanova, "Significance of calcium phosphate coatings for the enhancement of new bone osteogenesis - A review," *Acta Biomater.*, vol. 10, no. 2, pp. 557–579, 2014.
- [58] S. C. Velasco, "Production and characterization of ZrCZ-ag coatings deposited by magnetron sputtering," tese apresentada à Universidade do Minho para obtenção do grau de Doutor em Engenharia de Materiais, 2015.
- [59] J. A. Venables, "Nucleation and growth processes in thin film formation," *J. Vac. Sci. Technol. B Microelectron. Nanom. Struct.*, vol. 4, no. 4, p. 870, 1986.

- [60] S. H. Uhm, D. H. Song, J. S. Kwon, S. B. Lee, J. G. Han, and K. N. Kim, "Tailoring of antibacterial Ag nanostructures on TiO₂ nanotube layers by magnetron sputtering," *J. Biomed. Mater. Res. - Part B Appl. Biomater.*, vol. 102, no. 3, pp. 592–603, 2014.
- [61] M. D. J. Ooi, A. A. Aziz, and M. J. Abdullah, "Recent development in the growth of ZnO nanoparticles thin film by magnetron sputtering," *IEEE Int. Conf. Semicond. Electron. Proceedings, ICSE*, pp. 514–518, 2008.
- [62] M. M. Almoudi, A. S. Hussein, M. I. Abu Hassan, and N. Mohamad Zain, "A systematic review on antibacterial activity of zinc against *Streptococcus mutans*," *Saudi Dent. J.*, vol. 30, no. 4, pp. 283–291, 2018.
- [63] S. Fernando, T. Gunasekara, and J. Holton, "Antimicrobial Nanoparticles: applications and mechanisms of action," *Sri Lankan J. Infect. Dis.*, vol. 8, no. 1, p. 2, 2018.
- [64] R. M. F. de Sousa, T. A. R. da Silva, J. do C. Almeida, and W. Guerra, "Tantalum: Brief history, properties and applications," *Educ. Quim.*, vol. 24, no. 3, pp. 343–346, 2013.
- [65] Zimmers Biomet, "Trabecular Metal™ Implant Clinical Compendium." .
- [66] L. Fialho, L. Grenho, M. H. Fernandes, and S. Carvalho, "Porous tantalum oxide with osteoconductive elements and antibacterial core-shell nanoparticles: a new generation of materials for dental implants," *Mater. Sci. Eng. C*, vol. 120, no. December 2020, p. 111761, 2020.
- [67] L. Fialho, "Design of new biocompatible osseointegrated and antimicrobial dental implant," Universidade do Minho, 2021.
- [68] C. R. Brundle, *Encyclopedia of Materials Characterization*, no. 62. 1983.
- [69] R. Hazan, Y. A. Que, D. Maura, and L. G. Rahme, "A method for high throughput determination of viable bacteria cell counts in 96-well plates," *BMC Microbiol.*, vol. 12, 2012.
- [70] S. A. Alves *et al.*, "Tribo-electrochemical behavior of bio-functionalized TiO₂ nanotubes in artificial saliva: Understanding of degradation mechanisms," *Wear*, vol. 384–385, no. February, pp. 28–42, 2017.
- [71] I. Lafuente-Ibáñez de Mendoza, A. Cayero-Garay, G. Quindós-Andrés, and J. M. Aguirre-Urizar, "A systematic review on the implication of *Candida* in peri-implantitis," *Int. J. Implant Dent.*, vol. 7, no. 1, 2021.
- [72] P. Pereira-Silva *et al.*, "Antifungal activity of ZnO thin films prepared by glancing angle deposition," *Thin Solid Films*, vol. 687, no. April, p. 137461, 2019.
- [73] M. Sowa and W. Simka, "Electrochemical impedance and polarization corrosion studies of tantalum surface modified by DC Plasma electrolytic oxidation," *Materials (Basel)*, vol. 11, no. 4, 2018.
- [74] W. T. Huo, L. Z. Zhao, S. Yu, Z. T. Yu, P. X. Zhang, and Y. S. Zhang, "Significantly enhanced osteoblast response to nano-grained pure tantalum," *Sci. Rep.*, vol. 7, pp. 1–13, 2017.
- [75] A. C. Alves *et al.*, "Corrosion mechanisms in titanium oxide-based films produced by anodic treatment," *Electrochim. Acta*, vol. 234, pp. 16–27, 2017.

ANNEX

Annex 1: EDS spectra

Chemical characterization of TaCaP_Zn4, TaCaP_Zn6 and TaCaP_Zn7 samples was made by EDS (Figure 41 A to C) in order to qualitatively access the presence of Zn in the referred surfaces after the deposition of the NPs.

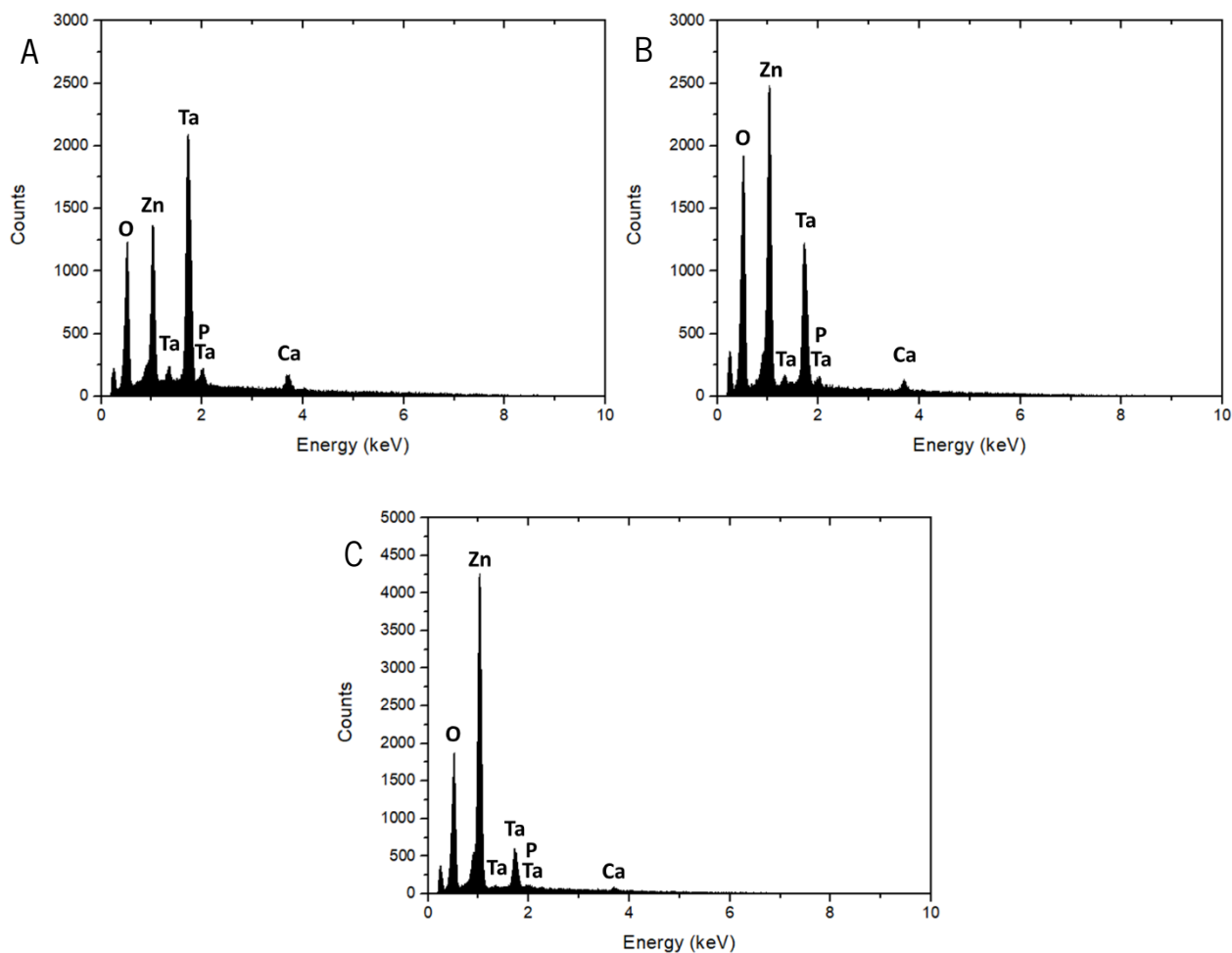


Figure 41 - EDS spectra of A) TaCaP_Zn4, B) TaCaP_Zn6 and C) TaCaP_Zn7 samples.

Annex 2: First Draft of Paper 1

Antimicrobial study of biofunctionalized Ta surfaces by PEO dopped with Zn nanoparticles

C. Rebelo, L. Fialho, S. Carvalho

University of Minho, Campus of Azurém, 4804-533 Guimarães, Portugal

CEMMPRE Mechanical Engineering Department, University of Coimbra, 3030-788 Coimbra, Portugal

Abstract — There are some problems associated with the dental implants being rejected by the body because of poor osteointegration between the implant surface and the bone and consequently bacterial growth. There are some ways to improve the osteointegration implant surfaces and inhibit the bacteria adhesion on its surface, by modifying them chemical and physically. This study is focused on Tantalum surfaces modified firstly by plasma electrolytic oxidation with incorporation of Calcium and Phosphorus and secondly with Zn(O) nanoparticles (with and without a Carbon layer) deposited by magnetron sputtering. The first modification intends to improve the osseointegration rate by mimetic the morphology and chemical composition from the bone. The NPs, deposited by different conditions to obtain different quantities, sizes and morphologies will add a new functionality: antimicrobial activity. The results obtained from the studies carried on that Tantalum surfaces revealed that the plasma electrolytic oxidation with incorporation of Calcium and Phosphorus was successful mimicking the morphology and the chemic of the bone, obtaining a porous surface dopped with Ca and P. Furthermore, the studies proved that the incorporation of Zn(O) nanoparticles in different quantities, sizes and morphologies had a great impact on the improvement of the antibacterial response of the studied surfaces.

Keywords—Tantalum, Calcium, Phosphorus, Zinc nanoparticles, Biofunctionalization, Antimicrobial Activity

I - INTRODUCTION

The criterion for the success of an implant is essentially clinical and is related to aspects as the implant's functional capacity, the absence of pain in the patient, and mobility [1]. Hence, implants are not always successful and may fail. Thus, the failure of a dental implant depends on several factors [2].

Ti-based dental implants show biological failures related to insufficient early osseointegration and high probability to occur a bacterial infection; mechanical failures concerning corrosion wear particles release; and surgical trauma, premature overloading, improper surgical placement, inadequate quantity and quality of host bone that can cause an iatrogenic failure [3][4].

When Ti-based implants are placed, interactions between their surface and human biological fluids and tissues occur. After implantation, two different responses may happen. In the first scenery, direct bone-implant contact is established, thus osseointegration is achieved. In the second scenery, fibrous soft tissue is formed around the implant, encapsulating it, which compromises proper biochemical fixation and further leads to implant failure. The surface properties (i.e., surface composition, roughness, and hydrophilicity) have an important role in implant-tissue interaction and, consequently, in proper osseointegration [5][6]. Furthermore, implant micromotions also play a key role in osseointegration and implant failure. These

have a negative influence on osseointegration and bone remodeling by allowing the formation of fibrous tissues on the resulting gap between the implant and the bone, inducing bone resorption [4]. Another main cause of dental implants failure is the development of infections as a response to microbial (e.g., bacterial or fungal) colonization onto the implant surface, that can take place during and/or after surgery [7][8]. The first and the most critical step leading to infection is microbial adhesion. Microbial colonization and biofilm formation on the implant surface may result in peri-implantitis disease, which can be characterized as an infection on the bone tissue. The infected tissues can trigger an immune response that can lead to bone resorption which may compromise the implant's anchorage leading to its loss [7][9][10]. Thus, to solve these limitations associated with the commercialized Ti-based implants, processes of surface modification of Ti are being reported. Another strategy being studied is the replacement of Ti implants by other biocompatible metals, such as Ta [11].

The surface modification of the biomaterial allows to tailor the surface properties (roughness, porosity, and chemistry) achieving the desired functionalities. This biofunctionalization aims to promote the ability to form a stronger bond between the bone tissue and the implant surface accelerating the osseointegration process [12][13]. Moreover, currently, the highest challenge in dentistry is the development of dental implant surfaces with antimicrobial activity, which is defined as the surface ability to inhibit the microorganisms' (bacteria, fungi, viruses) growth or to kill them [5][14].

The topographic/morphological modification of surfaces is based on roughness through the formation of micro/nano-porosities. The chemical composition of the implant surface is also an important feature in its biofunctionalization since it has an impact on the surface performance regarding osseointegration, antimicrobial activity, and corrosion resistance. Thus, topographic/morphological, and chemical composition modifications on the implant surfaces can be used to functionalize it. The biofunctionalization of metallic surfaces can be achieved by the application of several different surface modification techniques, such as electrochemical processes, and physical vapor deposition techniques (PVD). Electrochemical techniques, as anodization and plasma electrolytic

oxidation (PEO), are frequently used to modify metallic surfaces properties through the formation of micro/nano-porous structures, altering the surfaces roughness, wettability, free energy, crystallinity, and chemical composition, thus modeling the surfaces properties to mimic the bone's properties [15]. Furthermore, regarding the biofunctionalization provided by PVD techniques, the magnetron sputtering process is strongly used in industry to develop mostly thin films, but also the deposition of metallic nanoparticles [16].

The incorporation of osteoconductive elements, like Ca and P, has been widely studied in surface biofunctionalization since calcium (Ca^{2+}) and phosphate (PO_4^{3-}) ions are the main constituents of hydroxyapatite ($\text{Ca}_{10}(\text{PO}_4)_6(\text{OH})_2$), which is the dominant mineral phase in the bone structure. The incorporation of Ca and P mimics the bone composition, resulting in calcium phosphates, with a Ca/P ratio close to the theoretical hydroxyapatite ratio value (about 1.67) [7][12][14][17][18]. Furthermore, the incorporation of metallic nanoparticles (NPs) with antimicrobial properties, such as silver oxide, titanium dioxide, silicon, copper oxide, gold, magnesium oxide and zinc oxide (ZnO), has been studied to prevent post-operative infections. In the particular case of Zn, due to its antimicrobial properties, Zn has been added to mouth rinses and toothpaste to control dental plaque and inhibit calculus formation. However, because its NPs form is more toxic to bacteria, Zn/ZnO NPs have been used as antibacterial agents. The antimicrobial activity of ZnO nanoparticles is related to their ability to inhibit bacterial adhesion and biofilm formation by releasing Zn^{2+} ions [9][19][20].

Despite the surface modification of metallic surfaces, another sustainable alternative is the replacement of Ti-based implants by tantalum, since this is a very promising metal in terms of biocompatibility, bioactivity, and corrosion resistance.

In the work reported in this paper, the objective is to enhance the antimicrobial activity of tantalum-based surfaces, modified by PEO to mimic the morphology and chemical composition of the human bone, through the usage of different deposition conditions of Zn(O) nanoparticles by magnetron sputtering to achieve surfaces with nanoparticles in different quantities, sizes, and morphologies, starting from deposition

conditions used by Fialho *et. al* [21] in previous studies.

II – MATERIALS AND METHODS

1- Plasma electrolytic oxidation

Plasma electrolytic oxidation (PEO) was performed on an anodization system, consisting of a DC power supply (Agilent N5751A), a multimeter (Agilent 34450A 5 1/2 Digit), and an electrochemical cell. Tantalum square samples (99,95% purity, Testbourne) measuring 20x20 mm² were used as the substrate for the PEO process. The samples were first ultrasonically cleaned for 5 minutes in ethanol and in distilled water and air-dried at room temperature. Then, the PEO technique was performed on the samples in potentiostatic mode at 200 V, using an electrolyte composed of 0,35 M of calcium acetate (C₄H₆CaO₄, 99%, Biochem, Chemopharma) and 0,12 M of β-glycerol phosphate pentahydrate salt disodium ((HOCH₂)₂CHOP(O)(ONa)₂·xH₂O, 98%, Sigma-Aldrich), in agitation during 30 minutes at room temperature. In the electrochemical cell, the anode, corresponding to the Ta sample, and the cathode, corresponding to a graphite rod, were kept at a constant distance of 30 mm. After treatment, the samples were washed in distilled water and dried at room temperature. These samples were called TaCaP.

2- Magnetron Sputtering

Magnetron sputtering technique in non reactive mode was used to deposit Zn nanoparticles on the TaCaP samples (substracts), using a 200x100x6 mm³ Zn target of high purity (99,99%, Testbourne) and an

argon (Ar) flow of 80 sccm. To assure a homogeneous distribution of the nanoparticles, the sample-holder was kept in constant rotation, at 7rpm. To optimize the deposition process of Zn nanoparticles on the TaCaP surfaces, different deposition conditions were tested, starting from the condition reported by Fialho *et al.* [21], used as control (designated CD - P6.3_C0.5_t250 – control deposition). The parameters used in each deposition condition are presented in Table 1. The deposition conditions were designated after the order they were tested (Dx), followed by the working pressure (Px), current density (Cx), deposition time (t) and temperature (T) used. The modification of the deposition parameters aimed to obtain higher and different amounts of Zn nanoparticles.

Studies from other authors [22] proved that the Zn NPs tend to passivate, creating an oxide outer layer, assuming a Zn core and ZnO shell structure. However, this core-shell morphology was not accessed in this work.

An additional thin carbon layer was deposited over the optimized Zn nanoparticles, to control the Zn²⁺ ion release kinetics and consequently antimicrobial activity through the time. For that, C₂H₂ gas was used as a carbon precursor. The deposition chamber was connected to a DC power source to dissociate the C₂H₂. The carbon layer was deposited using a current of 0.4 A and a pressure of 3 Pa at a frequency of 200 kHz for 60 seconds. The atmosphere in the chamber was formed by a flow of 80 sccm of Ar and 20 sccm of C₂H₂. The carbon layer samples with nanoparticles deposited under D4-P6.3_C0.5_t1000 and D7-P2.0_C1_t500 conditions were referred to as TaCaP_Zn4C and TaCaP_Zn7C, respectively. The produced samples were stored in the desiccator.

Table 1 - Deposition parameters of Zn nanoparticles.

Designation	Pressure (Pa)	Current density (mA/cm ²)	Time (s)	Temperature (°C)
CD-P6.3_C0.5_t250	6.3	0.5	250	-
D1-P4.0_C0.5_t250	4.0	0.5	250	-
D2-P2.0_C0.5_t250	2.0	0.5	250	-
D3-P6.3_C0.5_t500	6.3	0.5	500	-
D4-P6.3_C0.5_t1000	6.3	0.5	1000	-
D5-P6.3_C1_t250	6.3	1	250	-
D6-P2.0_C0.5_t500	2.0	0.5	500	-
D7-P2.0_C1_t500	2.0	1	500	-
D8-P2.0_C1_t500_T150	2.0	1	500	150

3- STEM

The Scanning Transmission Electron Microscopy (STEM) technique allows the obtainance of micrographs of the surface of the samples under study and images of the internal microstructure of thin specimens. Thus, in this study, STEM technique was used to characterize the morphology of zinc nanoparticles deposited onto carbon lacey TEM grids, using the detector scanning transmission electron microscopy coupled with SEM (SEM/STEM, Nova NanoSEM 200 microscope, FEI), operating at 15 kV in A+B (dark and bright fields) mode.

4- SEM-EDS

The Scanning Electron Microscopy technique (SEM) allows the obtainance of micrographs of the samples under study, in order to study their morfology. The Scanning Transmission Electron Microscopy (STEM) allows the identification of the elements present in the chemical composition of the samples. Thus, SEM using an ultrahigh-resolution scanning electron microscope (Nova NanoSEM 200 microscope, FEI) at 5 kV in secondary mode was used to characterize the Zn nanoparticles deposited. In the particular case of the samples with a carbon layer, the analysis was performed at 10 kV in secondary mode. The EDS technique was performed using a EDAX- Pegasus X4M (EDS/EBSD) spectrometer, operating at 10 kV, to study the qualitative chemical composition of the samples under study.

5- ICP-EOS

The inductive coupled plasma optical emission spectroscopy (ICP-OES) technique was used to measure the release of Zn^{2+} ions from the samples. To performe this technique, the samples were immersed in 50 mL of phosphate-buffered saline (PBS) solution for 2, 24, and 48 hours, and 7, 14, and 30 days. The amount of Zn^{2+} ions leached into the PBS was diluted in HNO_3 (2%), in a ratio of 1:3 and measured 3 times for each time-point by ICO-OES (ICP PerkinElmer spectrometer model Optima 8000). The calibration curve (Figure 1) was performed using a Zn standard solution (Sigma-Aldrich, 1000 mg/L) prepared in different concentrations of HNO_3 (2%).

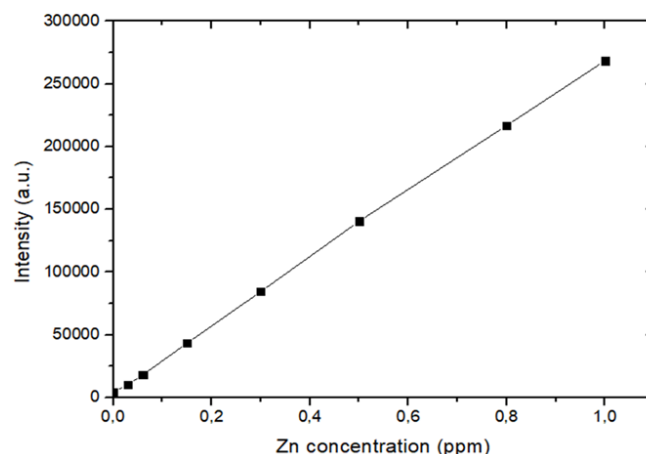


Figure 1 - ICP-OES calibration curve.

6- Biological assessment

6.1. – Antimicrobial activity

6.1.1. - Colony forming units - CFU

The colony forming units (CFU) technique is a standard method used to assess microbial viability. Thus, the antimicrobial activity of the surfaces was evaluated through incubation with the pathogenic opportunistic fungus *Candida albicans* SC5314 present in the oral cavity. Firstly, the samples were sterilized in dry heat (180 °C) for 2 h and a pre-inoculum (pre-culture) of *Candida albicans* cells was prepared by picking a colony and inoculating in 10 mL of YPD (1% w/v yeast extract, 1% w/v peptone, and 2% w/v glucose, Formedium). The pre-inoculum was incubated at 30 °C with 120 rpm in orbital agitation overnight (Benchtop Shaking Incubator 222DS). After the growth of the pre-inoculum, *Candida albicans* cells were transferred to a new culture tube, at an optical density ($O.D._{600nm}$) of 0.2, with 20 mL of YPD. This inoculum (cell culture) was incubated in 120 rpm orbital agitation at 30 °C and the cell growth was monitored until reached an $O.D._{600nm}$ of 0.5 (that translated that the *Candida albicans* cells are in the exponential growth phase). At this point, 200 μ L of the inoculum was added to the sterilized sample surfaces and incubated at 30 °C for 5 h and 24 h (cell viability time-points).

To determine the colony counts (CFU/mL), a serial dilution (from 10^{-1} to 10^{-5}) of *Candida albicans* cultures was performed for each time-point. For the first dilution(10^{-1}), 20 μ L of the cell culture on each surface

sample is diluted in 180 μL of deionized water, from where, after resuspension, 50 μL were pipetted to 450 μL of deionized water (second dilution - 10^{-2}), and so on. After all the dilutions were prepared, 50 μL of the latest three dilutions were pipetted five times onto the nutrient agar plates (YPD and agar, Labchem). This method was applied to the optimized surfaces with the Zn nanoparticles covered or not by the carbon layer. The TaCaP sample was used as a control. The experiment was performed in quadruplicate for each sample group.

Statistically significant differences between the sample groups were measured using two-ways analysis variance (one-way ANOVA) and Tukey's multiple comparison tests. All statistical analyses were carried out using GraphPad Prism6 statistical software package. All the data are expressed as mean \pm standard deviation.

Complementary biological tests (work not developed under this thesis) will be performed and added to this study, in order to better characterize the produced samples in terms of biological behavior.

6.1.2. – ROS formation

6.1.3. – Membrane integrity

6.2. – Cytotoxicity

6.2.1. – MTT

6.2.2. – LDH

6.3. – Phagocytosis study (macrophage + *candida albicans* culture)

III – RESULTS AND DISCUSSION

1 - Preparation of micro/nano-porous Ta surfaces and incorporation of osteoblastic elements

The PEO technique is used to obtain micro/nano-porous Ta surfaces with the incorporation of the

osteoconductive elements (Ca and P). The aim is to obtain surfaces morphologically and chemically closer to human bone. As already mentioned, experimental parameters reported by Fialho *et al.* [21] to obtain CaP-enriched porous Ta surfaces with a biomimetic Ca/P ratio were successful. Thus, in this study, the same experimental parameters are used to obtain similar surfaces. As expected, SEM micrographs of a Ta sample (without any treatment) (Figure 2 A) and micrographs from the functionalized PEO sample (TaCaP, Figure 2 B) show that the PEO technique results in the formation of pores of different sizes and diameters on the treated Ta surface (TaCaP), which approximates the surface morphology of this sample to that of human bone [21]. Moreover, the comparison between both Ta and TaCaP EDS spectra (Figure 2 C and D) prove the incorporation of Ca and P into the oxide layer.

2 – Optimization of Zn nanoparticles deposition

To deposit zinc nanoparticles on the TaCaP surface, the MS technique is used. Starting from the deposition conditions reported by Fialho *et al.* [21], defined as control (CD), new deposition conditions are tested by changing the deposition parameters (Table 1). These new deposition parameters aim to increase the number of nanoparticles (not attaining a thin film) to promote significative antimicrobial activity, not reached in the referred study. Figure 3 to 8 show STEM micrographs of TEM grids used for each of the deposition conditions.

First of all, the effect of working pressure is evaluated on the nanoparticles deposition. The working pressure is reduced from 6.3 Pa (pressure used on the control deposition - CD-P6.3_C0.5_t250), to 4 and 2 Pa on D1-P4.0_0.5_t250 and D2-P2.0_C0.5_t250 conditions, respectively. From the STEM images of CD-P6.3_C0.5_t250, D1-P4.0_0.5_t250, and D2-P2.0_C0.5_t250 (Figure 3), it is possible to observe that the D1-P4.0_0.5_t250 NPs (Figure 3 B) are similar in size and morphology to the ones in CD-P6.3_C0.5_t250 (Figure 3 A). However, the NPs on D2-P2.0_C0.5_t250 (Figure 3 C) look slightly larger and less regularly shaped than the NPs deposited under the CD-P6.3_C0.5_t250 and D1-P4.0_0.5_t250 conditions (Figure 3 A and B).

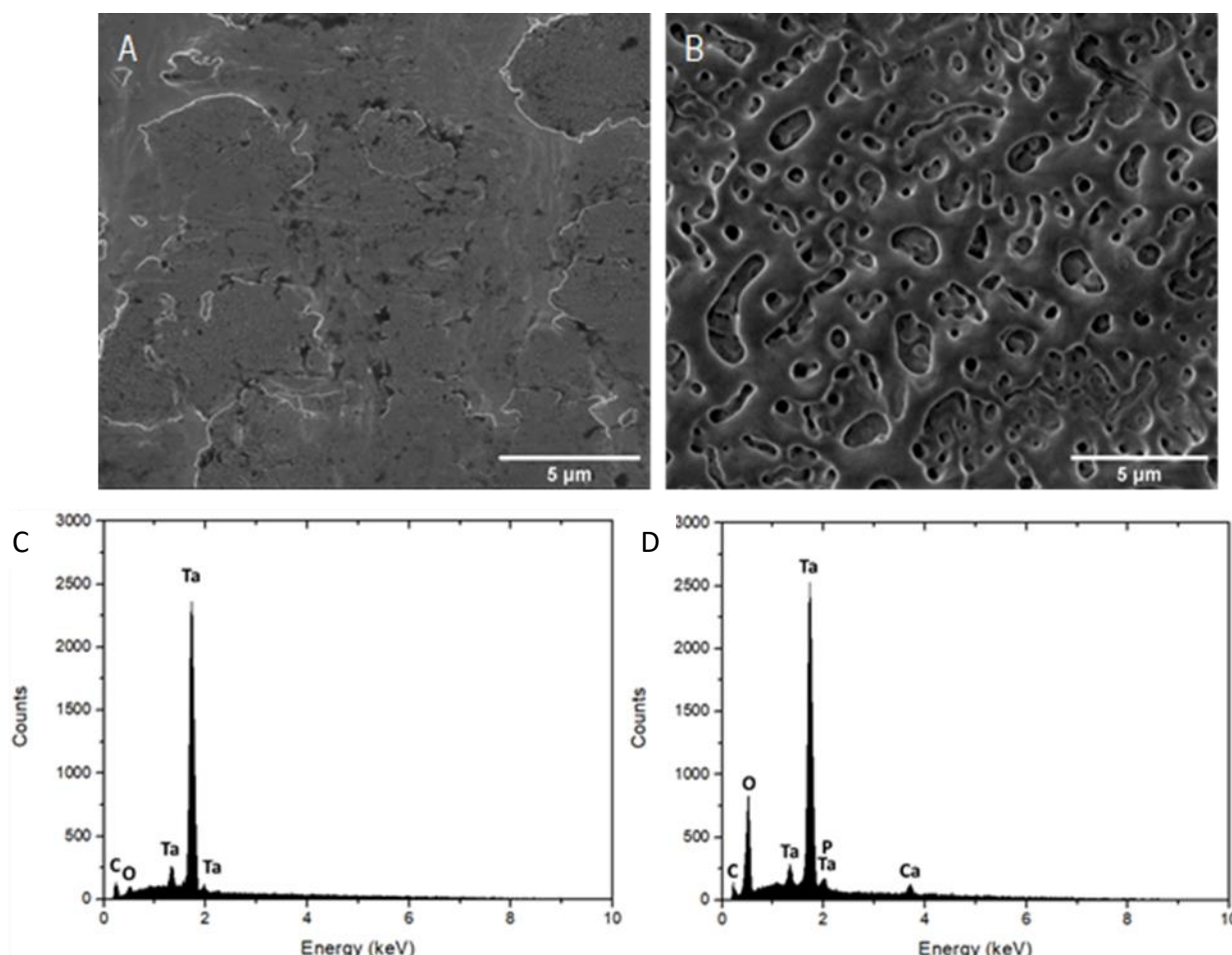


Figure 2 - SEM micrographs of A) Ta and B) Ta₂CaP and EDS spectra of C) Ta and D) TaCaP samples.

Furthermore, for this condition, it seems that a larger number of NPs is deposited on the grid.

The second parameter studied is the deposition time. STEM micrographs show that increasing the deposition time from 250 s (CD-P6.3_C0.5_t250 condition) to 500 s (D3-P6.3_C0.5_t500 condition) results in Zn NPs (Figure 4 A) with similar size and shape to those in CD-P6.3_C0.5_t250 and D1-P4.0_0.5_t250 (Figure 3 A and B). On the other hand, quadrupling the CD-P6.3_C0.5_t250 deposition time (D4-P6.3_C0.5_t1000 condition), results in larger and more irregular NPs (Figure 4 B). To this point, the NPs obtained under the D4-P6.3_C0.5_t1000 condition parameters are the ones showing more differences from the control's NPs.

Another deposition parameter tested is the current density, which is increased from 0.5 mA/cm² (CD-P6.3_C0.5_t250 condition) to 1 mA/cm² (D5-P6.3_C1_t250 condition). This change does not

result in significant changes in the size or morphology of the NPs (Figure 5), although a larger amount of NPs seems to be deposited in this TEM grid comparing to CD-P6.3_C0.5_t250's grid (Figure 3 A).

As in terms of working pressure the deposition condition that leads to better results is the D2-P2.0_C0.5_t250, the deposition time used in this deposition is increased to 500s (D6-P2.0_C0.5_t500 condition) to obtain even more improved results in terms of size and morphology of the NPs. SEM micrographs (Figure 6) show that the combination of these two parameters (pressure and time) results in the deposition of larger NPs than the ones in CD-P6.3_C0.5_t250 and D2-P2.0_C0.5_t250 (Figure 3 A and C), due to de agglomeration of some NPs. Moreover, the NPs morphology becomes more irregular and elongated.

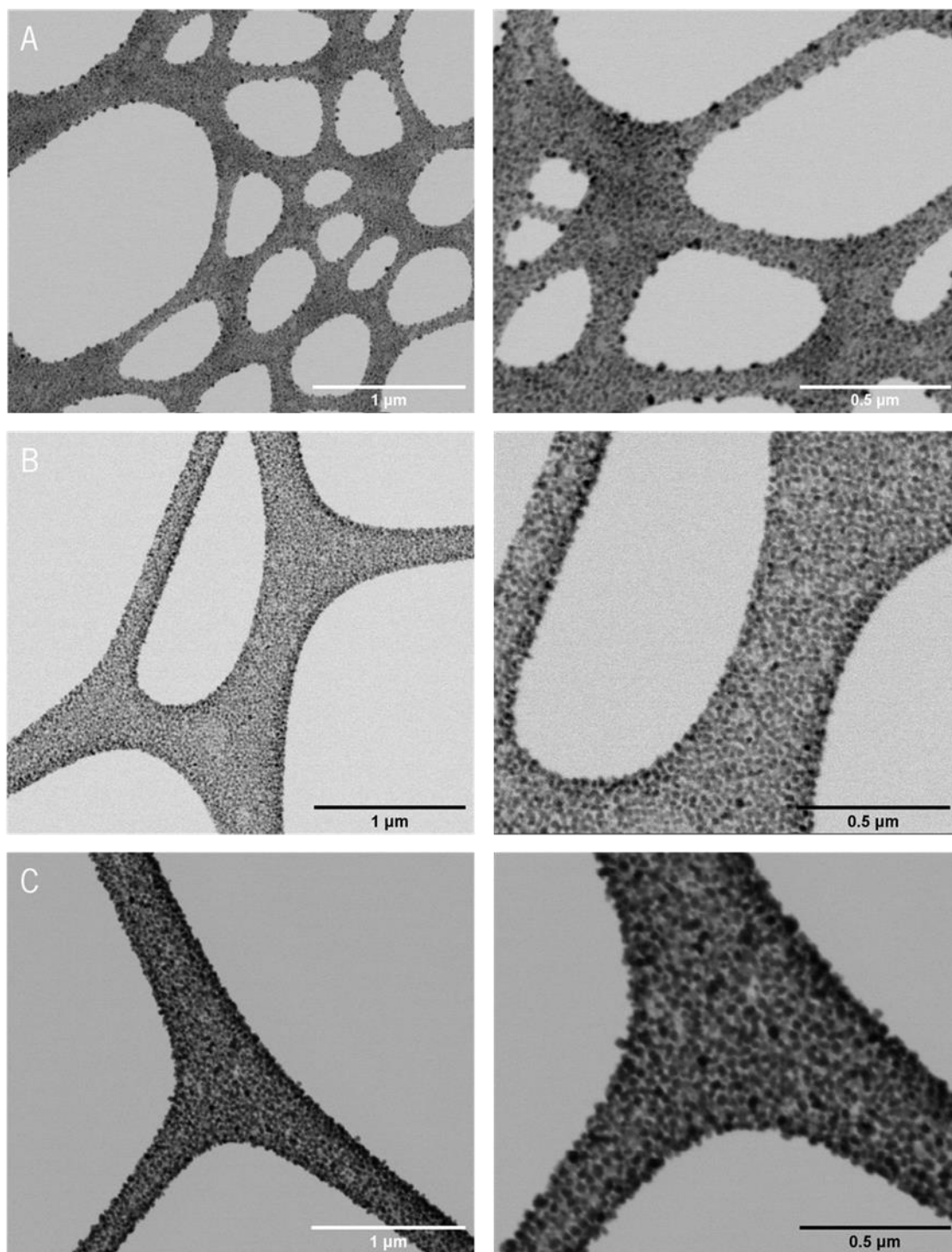


Figure 3 - STEM micrographs of A) CD-P6.3_C0.5_t250, B) D1-P4.0_0.5_t250 and C) D2-P2.0_C0.5_t250 conditions: depositions with work pressure variation. Scale: 1 μm on the left and 0.5 μm on the right.

Under the same parameters of D6-P2.0_C0.5_t500 deposition, but with a current density of 1 mA/cm² (D7-P2.0_**t500 condition) the NPs obtained (Figure 7) are, as expected, much larger than the NPs deposited under the CD-P6.3_C0.5_t250 condition (Figure 3 A). However, when compared to the NPs from the D6-P2.0_**t500 condition (Figure 6), the NPs from

the D7-P2.0_C1_t500 are less irregular, rounder, and have a more homogeneous size distribution.

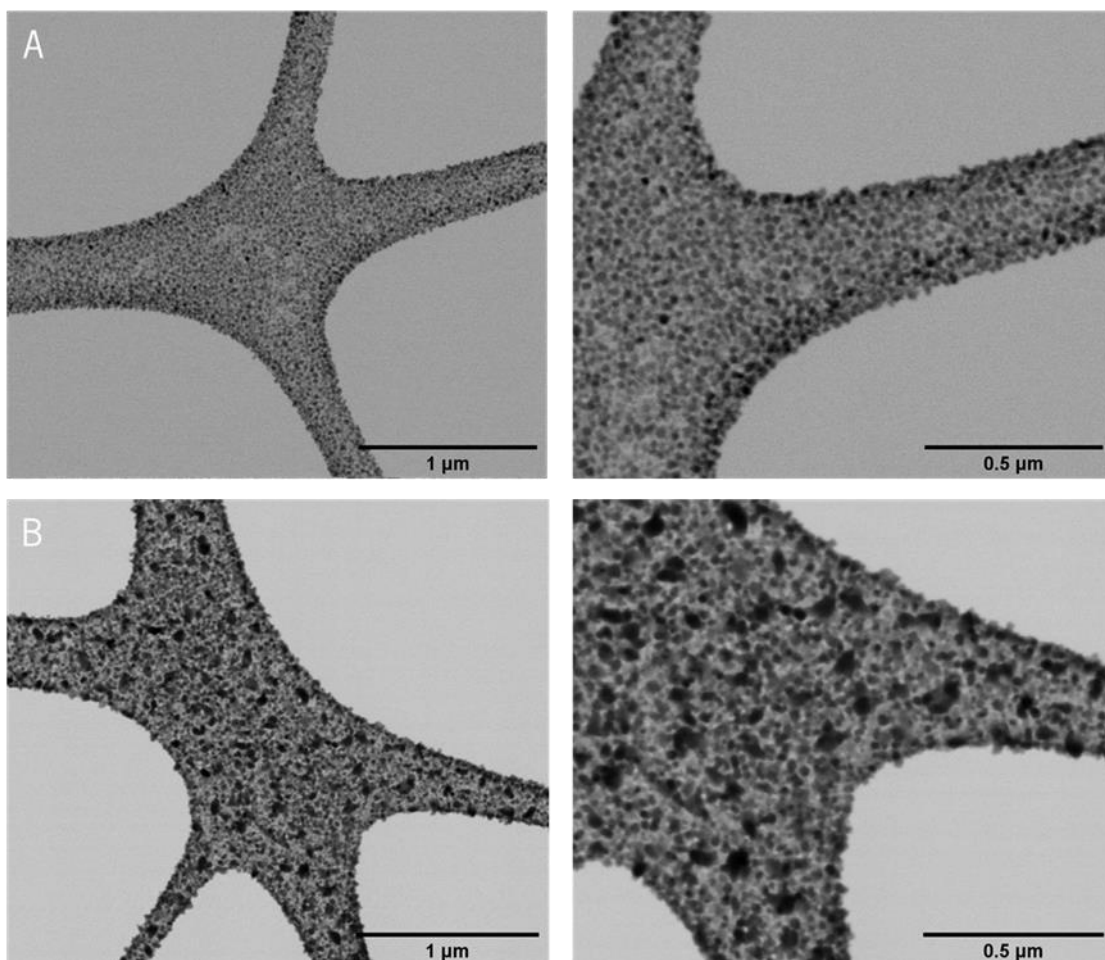


Figure 4 - STEM micrographs of A) D3-P6.3_C0.5_t500 and B) D4-P6.3_C0.5_t1000 conditions: depositions with deposition time variation. Scale: 1 μm on the left and 0.5 μm on the right.

The same parameters of D7-P2.0_C1_t500 condition, but with the deposition chamber at 150 °C (D8-P2.0_C1_t500_**T150** condition) are used to access the effect of the temperature. STEM micrographs (Figure 8) show that increase the temperature leads to a notorious effect on the morphology of the NPs, as they are elongated, compromising the nanoparticles'

rounded shape.

The flowchart from Figure 9 presents the main tendencies observed in the alteration of the amount, size, and morphology of the deposited NPs, resultant from the alteration of the deposition parameters. Generally, the results reveal that decreasing the

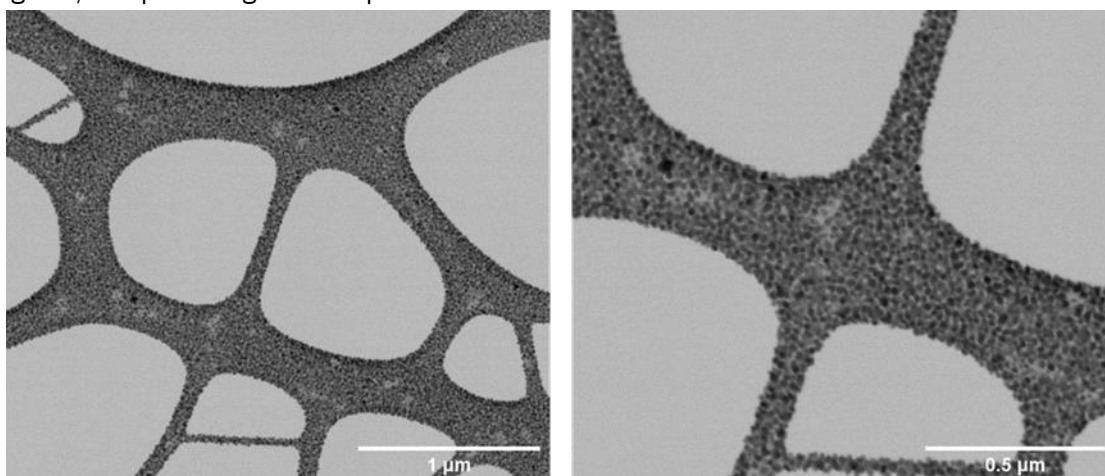


Figure 5 - STEM micrographs of D5-P6.3_C1_t250 condition: deposition with current density variation. Scale: 1 μm on the left and 0.5 μm on the right.

working pressure (D2-P2.0_C0.5_t250 condition - Figure 3 B), increasing the deposition time (D4-P6.3_C0.5_t1000 condition - Figure 4 B) and the current density (D5-P6.3_C1_t250 condition - Figure 5) result in higher amounts of nanoparticles.

Furthermore, results prove that combining the referred parameters (D6-P2.0_C0.5_t500 and D7-P2.0_C1_t500 conditions - Figure 6 and Figure 7, respectively) lead to the increase of the nanoparticles'

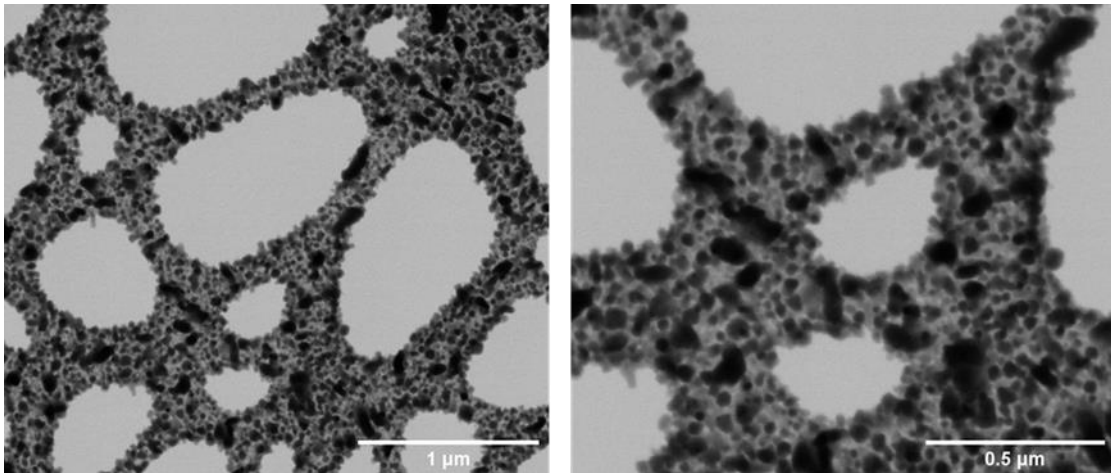


Figure 6 - STEM micrographs of D6-P2.0_C0.5_t500 condition: deposition with work pressure and deposition time variation. Scale: 1 μm on the left and 0.5 μm on the right.

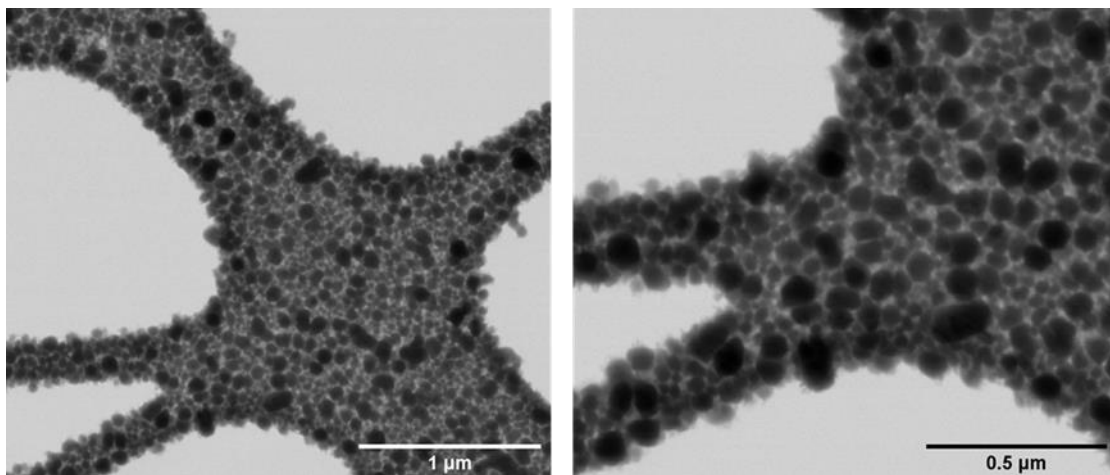


Figure 7 - STEM micrographs of D7-P2.0_C1_t500 condition: deposition with work pressure, deposition time and current density variation. Scale: 1 μm on the left and 0.5 μm on the right.

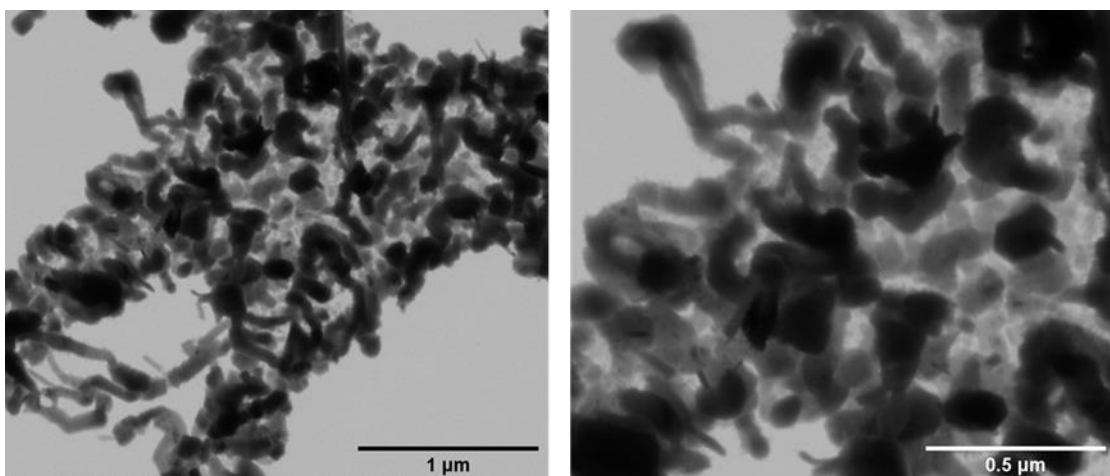


Figure 8 - STEM micrographs of D8-P2.0_C1_t500_T150 condition: deposition with work pressure, deposition time, current density, and temperature variation. Scale: 1 μm on the left and 0.5 μm on the right.

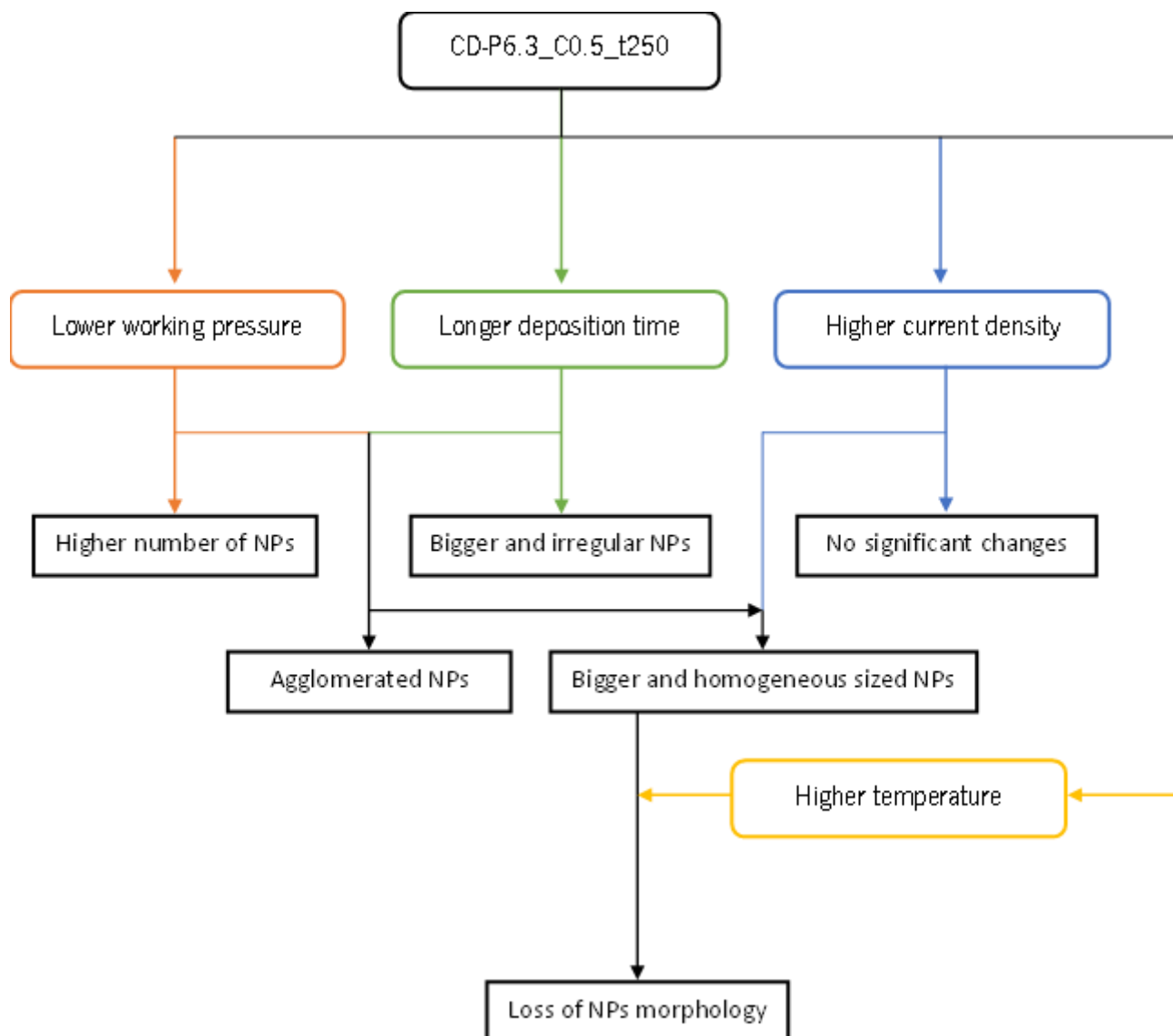


Figure 9 - Summary flowchart of the main conclusions drawn from the STEM micrographs.

size. Thus, these five deposition conditions are selected to be further analyzed in the next step.

SEM analyzes of the silicon used as substrate for the five deposition conditions selected above, as well as in the CD-P6.3_C0.5_t250 deposition (as control), are presented to verify and complement the observations made through the STEM analyses of the TEM grids.

Through the micrographs represented in Figure 10 it is possible to verify that all depositions achieve a good distribution of Zn NPs through the silicon surface, covering the surfaces completely. In the CD-P6.3_C0.5_t250 condition (Figure 10 A), it is possible to observe that the deposited NPs are small and round, in comparison with the ones deposited by the other deposition conditions. On the other hand, in D2-P2.0_C0.5_t250 and D4-P6.3_C0.5_t1000

conditions (Figure 10 B and C, respectively), there is noticed an increment in the size of the NPs, followed by a morphological change, with a mix of smaller (like in CD-P6.3_C0.5_t250 condition - Figure 10 A), larger and irregular NPs being observed. Figure 10 C makes it clear that in the D4-P6.3_C0.5_t1000 condition there is a greater amount of larger and more irregular nanoparticles compared to the D2-P2.0_C0.5_t250 condition (Figure 10 B). The D5-P6.3_C1_t250 condition (Figure 10 D) allows the deposition of Zn NPs extremely similar to the ones in CD-P6.3_C0.5_t250, although few larger NPs are observed. In the D6-P2.0_C0.5_t500 condition (Figure 10 E), as observed through the STEM images (Figure 6), it is visible an increase in the NPs size, as well as a more irregularity in their shape. D7-P2.0_C1_t500 condition (Figure 10 F) leads to the deposition of big Zn NPs with a very

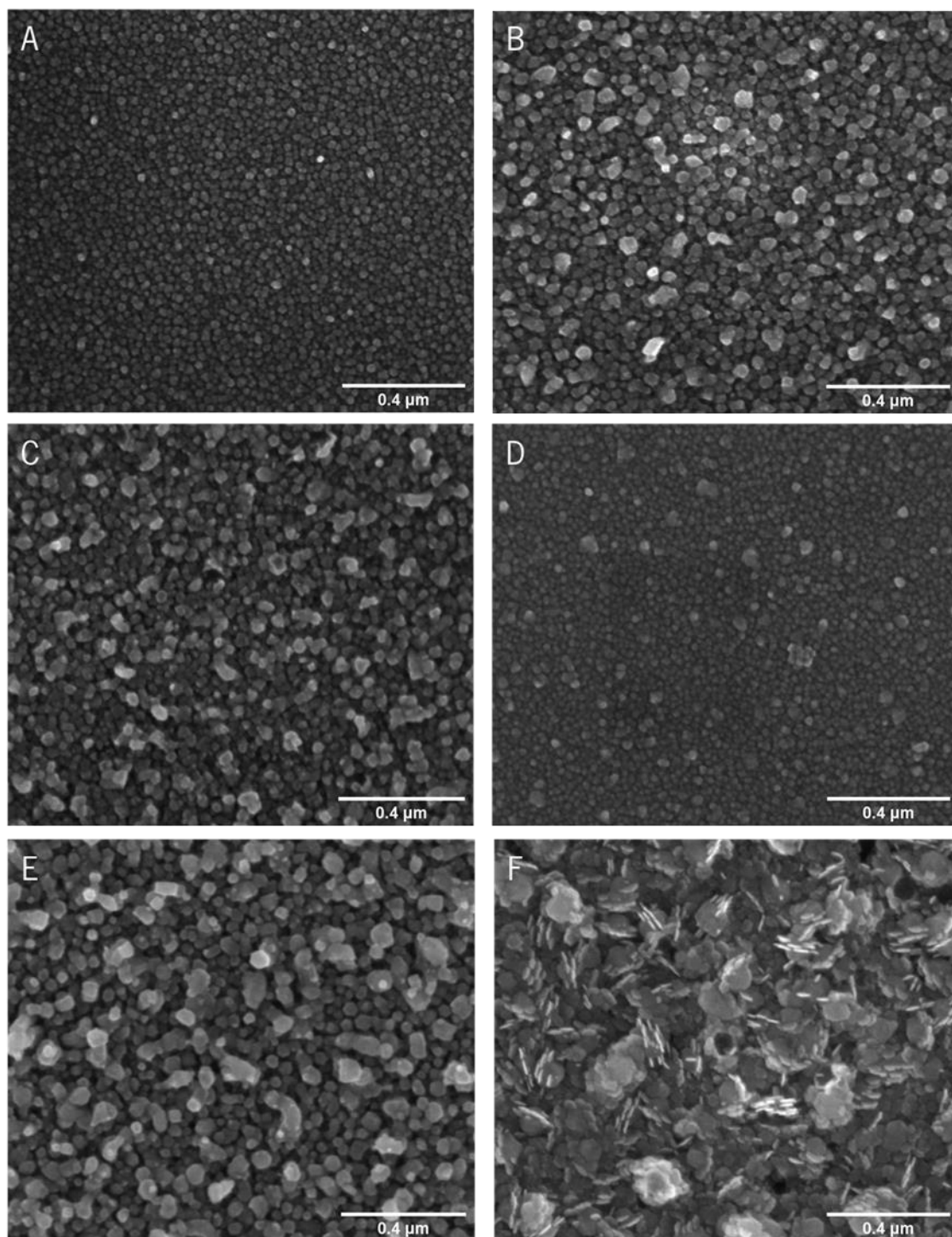


Figure 10 - SEM micrographs of the Si substrate with Zn nanoparticles deposited under A) CD-P6.3_C0.5_t250, B) D2-P2.0_C0.5_t250, C) D4-P6.3_C0.5_t1000, D) D5-P6.3_C1_t250, E) D6-P2.0_C0.5_t500 and F) D7-P2.0_C1_t500 depositions. Scale: 0.4 μm .

different morphology from all the other NPs achieved from the other conditions, with the NPs seeming to be more of agglomerations of smaller NPs, rather than isolated NPs.

Regarding these results, as the number of Zn nanoparticles deposited using the D5-P6.3_C1_t250 condition seems to be too similar to the number

obtained using the CD-P6.3_C0.5_t250 condition, the D4-P6.3_C0.5_t1000, D6-P2.0_C0.5_t500, and D7-P2.0_C1_t500 conditions are chosen for further evaluation. This selection aims to analyze the influence of the size (D4-P6.3_C0.5_t1000 condition with smaller NPs and D6-P2.0_C0.5_t500 sample with larger NPs), and morphology (D7-P2.0_C1_t500

condition) of the deposited NPs on the antimicrobial activity and corrosion behavior of the surfaces..

Although the STEM and SEM images presented above allow to take some conclusions about the amount, size, and morphology of the deposited NPs, these conclusions are only qualitative, once the obtained NPs do not allow a quantitative analyze, due to the reduced size of some of the nanoparticles and the coalescence of the bigger ones. Furthermore, EDS analyses of the selected samples (now redenominated TaCaP_Zn4, TaCaP_Zn6, and TaCaP_Zn7), presented in Annex, also do not allow to make any conclusion about the quantity of Zn present in each sample since this is a qualitative technique. Thus, the selected samples, as well as a TaCaP_CD sample serving as control, are analyzed by ICP-OES to study the release of Zn^{2+} ions from the surfaces.

Figure 11 shows the Zn^{2+} ions profile of each surface group after 2, 24, and 48 hours and 7, 14, and 30 days of immersion in PBS.

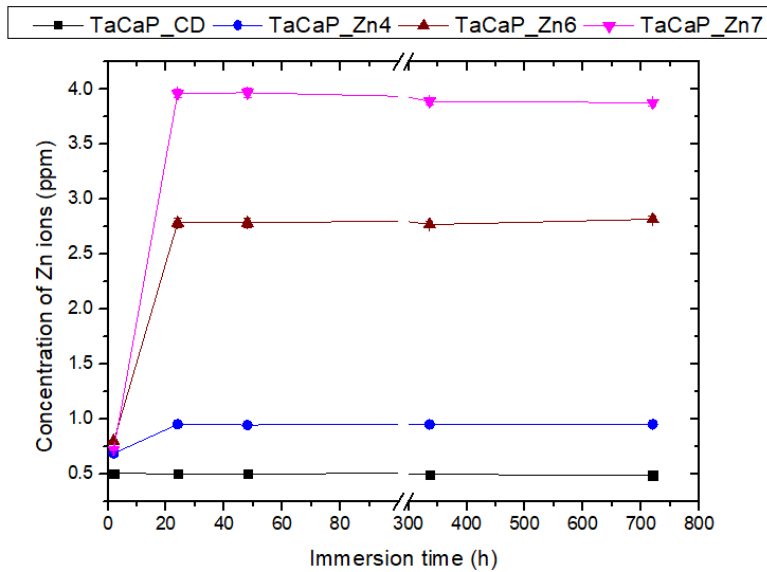


Figure 11 - Zn^{2+} ion release profile for TaCaP_CD, TaCaP_Zn4, TaCaP_Zn6 and TaCaP_Zn7 samples.

All Zn-containing samples show higher ionic release than the overall profile of the TaCaP_CD sample, which shows a maximum concentration of Zn^{2+} ions release of 0.49 ± 0.01 ppm. After 2 h of immersion, all samples reveal similar levels of Zn^{2+} ions release, achieving the maximum ionic release after 24 h of immersion, remaining constant afterward. The sample that presents higher concentration of Zn^{2+} ions release is TaCaP_Zn7 (3.96 ± 0.04 ppm), followed by TaCaP_Zn6 (2.79 ± 0.01 ppm) and TaCaP_Zn4 (0.95

± 0.01 ppm). Thus, it is possible to conclude that the samples with a higher concentration of Zn^{2+} ions release, TaCaP_Zn6, and TaCaP_Zn7 samples, are the ones with more quantity of Zn NPs deposited, which comes in agreement with what is observed in the morphological analyses.

An important fact to take into consideration is that none of the Zn-containing samples exceeds the limit of toxicity of Zn^{2+} ions in the human body, which according to the literature corresponds to $10 \mu\text{g/mL}$ (approximately 10 ppm) [19].

Considering the Zn^{2+} ions release profiles, as well as the NPs morphology, TaCaP_Zn4 and TaCaP_Zn7 samples are the samples selected to be further studied in order to understand the effect of the amount of Zn^{2+} ions released from the surfaces and the effect of the Zn nanoparticles' sizes and shapes on the surfaces' functional performance, since these are the samples with the lowest and the highest quantity of Zn NPs, as well as the more and the less homogeneous shaped NPs, comparing to the control.

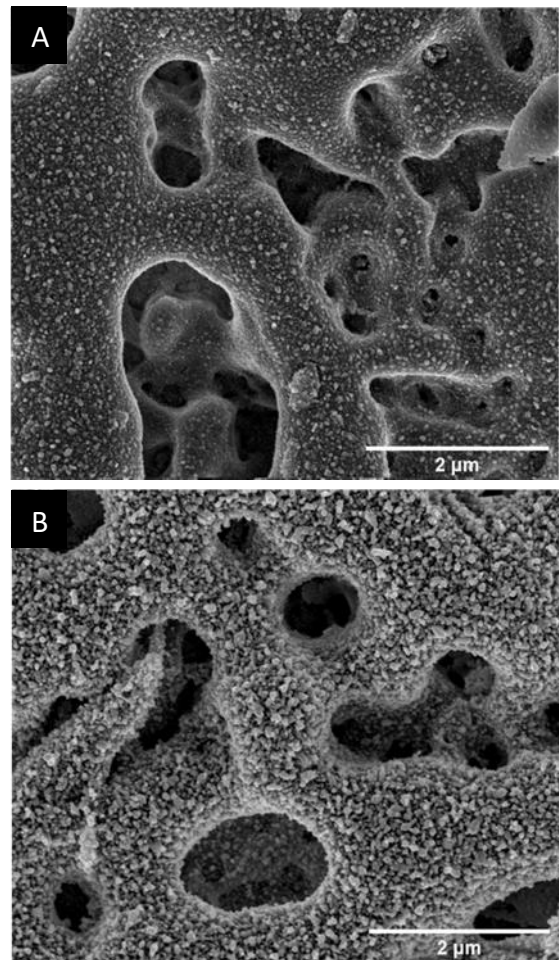


Figure 12 - SEM micrographs of A) TaCaP_Zn4 and B) TaCaP_Zn7 samples.

Figure 12 presents SEM micrographs of the TaCaP_Zn4 and TaCaP_Zn7 samples. Through the observation of the micrographs, it is possible to observe that in both samples, the nanoparticles are present in the surface of the samples, as well as in the interior of the pores, without compromising the porous morphology achieved by the PEO technique (Figure 2 B).

3 – Deposition of a carbon layer over the optimized surfaces

As all the Zn-containing surfaces have the burst ion release in the first 24 h of immersion, a carbon layer is deposited over the Zn NPs of the selected samples (TaCaP_Zn4 and TaCaP_Zn7) to try to control and prolong the ionic release over the first 24 hours of immersion. The samples resulting from this process are named TaCaP_Zn4C and TaCaP_Zn7C.

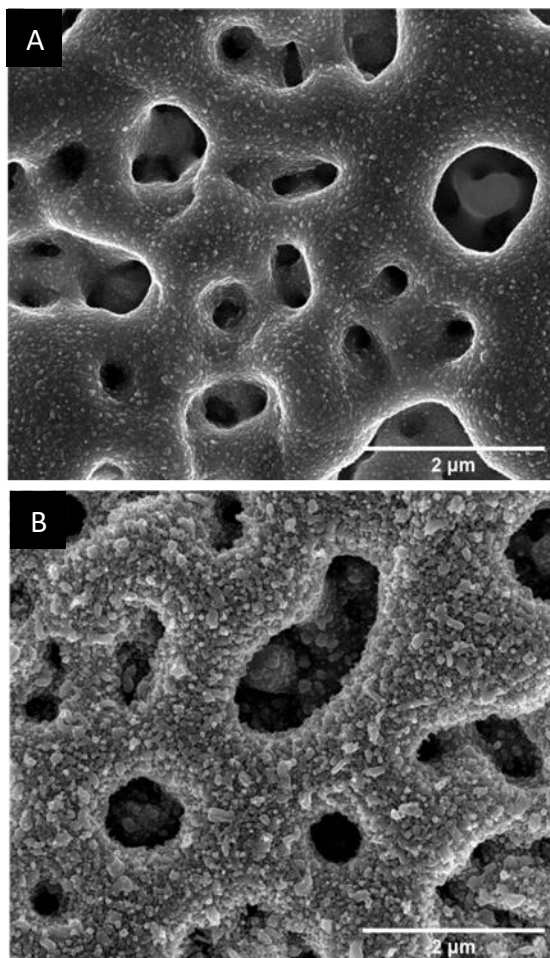


Figure 13 - SEM micrographs of A) TaCaP_Zn4C and B) TaCaP_Zn7C samples.

To assess the impact of the carbon layer deposition on the porous morphology, SEM micrographs (Figure 13 of TaCaP_Zn4C, and TaCaP_Zn7C samples) is presented. It is possible to observe that the carbon layer encapsulates the NPs when compared with the TaCaP_Zn4 and TaCaP_Zn7 samples (Figure 12), without compromising their micro/nano-porous structure.

As the aim of the carbon layer deposited over the Zn NPs is to control the kinetics of Zn^{2+} release in the first hours of immersion, the ion release profiles of the carbon layered samples, evaluated by ICP-OES (Figure 14), is also analyzed.

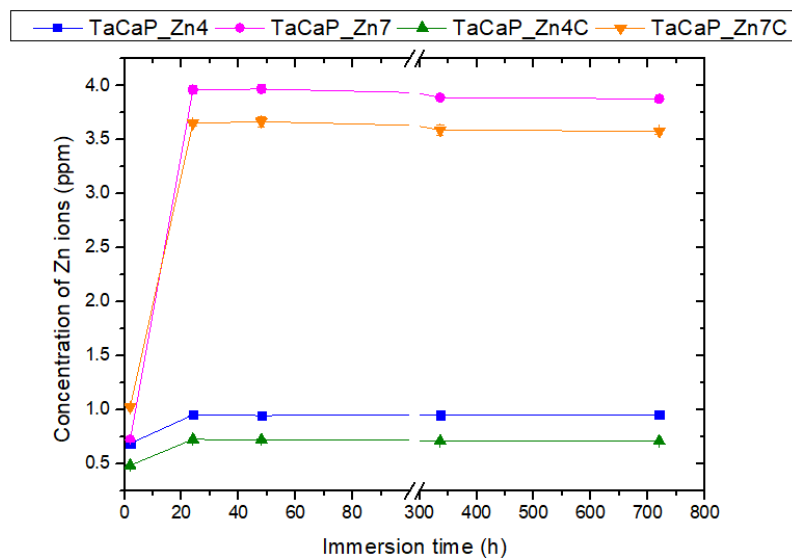


Figure 14 - Zn^{2+} ion release profile for TaCaP_Zn4, TaCaP_Zn4C, TaCaP_Zn7 and TaCaP_Zn7C samples.

Both the samples with (TaCaP_Zn4C and TaCaP_Zn7C) and without (TaCaP_Zn4 and TaCaP_Zn7) carbon layer show the same trend of Zn^{2+} ion release profile, with the largest amount of ions being released between the first 2 and 24 hours of immersion and no significant Zn^{2+} release being observed thereafter. The results also indicate that the carbon layer presence results in a decrease in the Zn^{2+} ions release, as the released zinc ions concentration is lower for TaCaP_Zn4C and TaCaP_Zn7C than for TaCaP_Zn4 and TaCaP_Zn7 samples, respectively, in every studied time-point during the 30 days of immersion in PBS. Thus, it suggests that some of the Zn NPs are still encapsulated by the C layer, however they not have mobility on the carbon layer meaning that they cannot be released.

4 – Biological assessment

4.1. – Antimicrobial activity

4.1.1. – CFU

To access the antimicrobial capacity of the Zn-containing porous Ta₂O₅ surfaces, CFU technique, performed with *Candida albicans* fungus, was used. The study was performed using *Candida albicans* fungus since it is reported in the literature [23] that this fungus is commonly present in the oral cavity and can trigger mucosa infections associated with the maintenance of peri-implantitis disease. Pereira-Silva *et al.* [24] studied the antifungal activity of ZnO thin films against *Candida albicans*, obtaining values of inhibition of viable cell growth of 58% and 68% compared to the glass lamella used as control, after 8h and 25h of incubation, respectively.

Figure 15 shows the cell viability of the Zn-containing surfaces at 5 and 24 hours of culture, and the TaCaP sample as control. The results reveal a significant reduction in the quantity of viable fungus in Zn-containing sample, compared to the control (TaCaP), both at 5 and 24 hours. At 5 hours of culture, the results reveal similar cell viability for all the Zn-containing samples, with a significant reduction in the number of viable cells when compared to the control. Regarding the results at 24 hours, it is verified a clear influence of the quantity of NPs in the reduction of the number of viable cells, with the TaCaP_Zn7 sample showing a lower quantity of viable cells compared with TaCaP_Zn4 sample's quantity, which is in agreement with the obtained results for the ionic release of Zn²⁺ ions in the ICP-OES (Figure 11 and Figure 14). Although there is no statistically significant difference between the respective surfaces, the carbon layered samples seem to demonstrate a slightly better antimicrobial behavior when compared with their equivalent sample without carbon layer, even though these samples have a lower quantity of Zn²⁺ ions released in the ICP-OES (Figure 14). Thus, the ionic release from the TaCaP-Zn7C is sufficient to guarantee a significant inhibition of the fungi growth. As it is well known, the chemical composition and the surface morphology has a strong influence on cell responses. Thus, a possible explanation for these results may be the fact that the carbon layer leads to partial mitigation of the pores at the nanoscale (Figure 13), which are

preferential spots for cell growth, thus making it more difficult for the *C. albicans* to adhere and proliferate.

To sum up, the results clearly demonstrate that the presence of the Zn NPs prevent the *Candida albicans* growth, which means that these samples are fungistatic. By increasing the amount of Zn NPs deposited onto the TaCaP surface the reduction of metabolic viable cells increases, which indicates that the higher Zn²⁺ ions release can be a possible antimicrobial mechanism. However, other mechanisms may also be responsible for the antimicrobial activity of the developed samples.

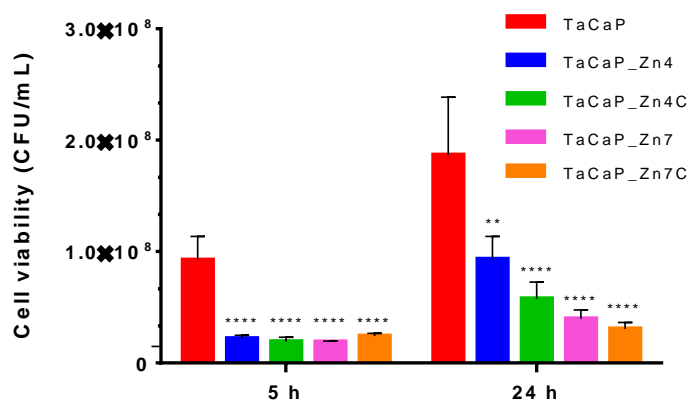


Figure 15 - Cell viability of *Candida albicans* after 5 and 24 h of incubation on TaCaP (control), TaCaP-Zn4, TaCaP-Zn4C, TaCaP-Zn8 and TaCaP-Zn8C surfaces. Significant values as * $p \leq 0.05$, ** $p \leq 0.01$, *** $p \leq 0.001$ and **** $p \leq 0.0001$, significant reduction compared to control (TaCaP surface).

Complementary biological tests to better understand the mechanism (or mechanisms) responsible for the antimicrobial capacity of the developed samples will be lately performed to complement this study. It is important to prove that these surfaces are not cytotoxic of osteoblastic cells and that they promote the cellular responses (protein adsorption, cell proliferation and differentiation).

4.1.2. – ROS formation

4.1.3. – Membrane integrity

4.2. – Citotoxicity

4.2.1. – MTT

4.2.2. – LDH

4.3. – Phagocytosis study (macrophage + *candida albicans* culture)

IV – CONCLUSIONS

In this study, different amount of Zn NPs, with and without a thin C layer, were deposited onto micro/nano-porous Ta surfaces, to develop antimicrobial surfaces to be used as biomaterial for dental implants. The micro/nano-porous Ta surfaces were produced by PEO, performed on high-purity Ta sheets. The Zn NPs were deposited, by magnetron sputtering, onto the porous Ta surfaces, with several different sets of deposition conditions being used to achieve surfaces with different Zn NPs' quantities, and consequently morphologies and sizes. The NPs depositions that allowed the higher amount of Zn NPs with the highest zinc ions release and a lower amount of Zn NPs with the low Zn ions release were selected as optimized samples, to better understand the influence of the amount and morphology of Zn NPs in the surfaces' antimicrobial response and corrosion resistance. Posteriorly, a thin C layer was deposited over the two optimized samples, by magnetron sputtering. The samples were characterized by morphological, chemical, and functional techniques, in order to assess their morphological and chemical properties, as well as their antimicrobial and corrosion performances.

PEO technique was proven to be successful, since the morphological and chemical characterization of the developed samples proved the existence of porous structures and incorporation of osteoconductive elements (Ca and P) onto their surfaces. Thus, the PEO allowed the development of surfaces morphological and chemically similar to the human bone. The magnetron sputtering technique, performed under different deposition conditions, allowed the deposition of Zn NPs in different contents, sizes and morphologies, as it was proven by morphological characterization. ICP-OES technique gave a quantitative characterization of the sputtered samples in terms of Zn²⁺ ions release, allowing the choice of the samples with the highest and lowest quantity of Zn.

Furthermore, chemical characterization confirmed the presence of C layer where the C layer was sputtered.

ICP-OES results from both Zn-containing samples covered or not by the C layer showed that the C layer influenced the quantity of Zn²⁺ ions released from the samples, since it acts as barrier layer inhibiting the ions release, comparing with the equivalent sample without C layer.

The antimicrobial ability was assessed by CFU. The obtained results proved that the presence and quantity of Zn in the surfaces had a strong influence on the quantity of viable cells, since all the Zn-containing samples revealed capacity to inhibit the cell growth (fungistatic), in both 5 and 24 hours of cell culture. The samples with highest quantity of Zn (higher Zn ions release) are the ones that showed the greatest reduction on the quantity of viable cells after 24 h of culture. Furthermore, it was proven that the C layer did not significantly affect the antimicrobial capacity of the samples, translating that the lower ions release did not impair the antimicrobial performance of these Zn- and C-containing surfaces.

As future work, the study of the mechanical properties, such as elastic modulus and fracture strength, of the developed samples would be important to guarantee the mechanical resistance of these surfaces. The study of the corrosion behavior of the optimized surfaces would also be interesting to access if the antimicrobial enhancement does not compromise the corrosion resistance of the developed samples.

ACKNOWLEDGEMENTS

REFERENCES

- [1] R. Lucas, "Fatores que afetam a osteointegração dos implantes – Uma Revisão," vol. 1, 2013.
- [2] S. Sakka, K. Baroudi, and M. Z. Nassani, "Factors associated with early and late failure of dental implants.," *J. Investig. Clin. Dent.*, vol. 3, no. 4, pp. 258–261, 2012.
- [3] K. Subramani and R. T. Mathew, *Titanium Surface Modification Techniques for Dental Implants-From Microscale to Nanoscale*, First Edit. Elsevier Inc., 2012.

- [4] F. Javed, H. Ahmed, R. Crespi, and G. Romanos, "Role of primary stability for successful osseointegration of dental implants: Factors of influence and evaluation," *Interv. Med. Appl. Sci.*, vol. 5, no. 4, pp. 162–167, 2013.
- [5] L. Le Guéhennec, A. Soueidan, P. Layrolle, and Y. Amouriq, "Surface treatments of titanium dental implants for rapid osseointegration," *Dent. Mater.*, vol. 23, no. 7, pp. 844–854, 2007.
- [6] K. Subramani, S. Lavenus, J. Rozé, G. Louarn, and P. Layrolle, "Impact of nanotechnology on dental implants," *Emerg. Nanotechnologies Dent. Second Ed.*, no. February, pp. 83–97, 2018.
- [7] S. A. Alves, "A new concept of bio-multifunctional nanotubular surfaces for dental implants: tribocorrosion resistant, antibacterial and osteogenic," tese apresentada à Universidade do Minho para obtenção do grau de Doutora em Engenharia Biomédica, 2017.
- [8] L. G. Harris and R. G. Richards, "Staphylococci and implant surfaces: a review," *Injury*, vol. 37, no. 2 SUPPL., 2006.
- [9] J. Oliveira, "Deposition of Zn-ZnO nanoparticles by magnetron sputtering onto tantalum substrates," dissertação apresentada à Universidade do Minho para obtenção do grau de Mestre em Engenharia de Materiais, 2017.
- [10] C. A. Alves, "Desenvolvimento de revestimentos nanoestruturados para implantes osteointegrados," dissertação apresentada à Universidade do Minho para obtenção do grau de Mestre em Engenharia de Materiais, 2013.
- [11] R. Bai *et al.*, "Metallic antibacterial surface treatments of dental and orthopedic materials," *Materials (Basel)*, vol. 13, no. 20, pp. 1–21, 2020.
- [12] S. Pires, "Incorporação de Ca, P e Mg em óxido de Ta nanoestruturado para acelerar a osteointegração em implantes dentários," dissertação apresentada à Universidade do Minho para obtenção do grau de Mestre em Engenharia de Materiais, 2016.
- [13] T. Hanawa, "Research and development of metals for medical devices based on clinical needs," *Sci. Technol. Adv. Mater.*, vol. 13, no. 6, 2012.
- [14] F. Oliveira, "Biofunctionalization of titanium surfaces for dental implants: osteogenic, anti-microbial and tribocorrosion resistant surfaces," tese apresentada à Universidade do Minho para obtenção do grau de Doutor em Engenharia Biomédica, 2015.
- [15] T. W. Clyne and S. C. Troughton, "A review of recent work on discharge characteristics during plasma electrolytic oxidation of various metals," *Int. Mater. Rev.*, vol. 64, no. 3, pp. 127–162, 2019.
- [16] R. Rasouli, A. Barhoum, and H. Uludag, "A review of nanostructured surfaces and materials for dental implants: Surface coating, patterning and functionalization for improved performance," *Biomater. Sci.*, vol. 6, no. 6, pp. 1312–1338, 2018.
- [17] B. Wopenka and J. D. Pasteris, "A mineralogical perspective on the apatite in bone," *Mater. Sci. Eng. C*, vol. 25, no. 2, pp. 131–143, 2005.
- [18] R. A. Surmenev, M. A. Surmeneva, and A. A. Ivanova, "Significance of calcium phosphate coatings for the enhancement of new bone osteogenesis - A review," *Acta Biomater.*, vol. 10, no. 2, pp. 557–579, 2014.
- [19] A. Sirelkhatim *et al.*, "Review on zinc oxide nanoparticles: Antibacterial activity and toxicity mechanism," *Nano-Micro Lett.*, vol. 7, no. 3, pp. 219–242, 2015.
- [20] M. M. Almoudi, A. S. Hussein, M. I. Abu Hassan, and N. Mohamad Zain, "A systematic review on antibacterial activity of zinc against *Streptococcus mutans*," *Saudi Dent. J.*, vol. 30, no. 4, pp. 283–291, 2018.
- [21] L. Fialho, L. Grenho, M. H. Fernandes, and S. Carvalho, "Porous tantalum oxide with osteoconductive elements and antibacterial core-shell nanoparticles: a new generation of materials for dental implants," *Mater. Sci. Eng. C*, vol. 120, no. December 2020, p. 111761, 2020.
- [22] L. Fialho, "Design of new biocompatible osseointegrated and antimicrobial dental implant," Universidade do Minho, 2021.
- [23] I. Lafuente-Ibáñez de Mendoza, A. Cayero-Garay, G. Quindós-Andrés, and J. M. Aguirre-Urizar, "A systematic review on the implication of *Candida* in peri-implantitis," *Int. J. Implant Dent.*, vol. 7, no. 1, 2021.
- [24] P. Pereira-Silva *et al.*, "Antifungal activity of ZnO

thin films prepared by glancing angle deposition," *Thin Solid Films*, vol. 687, no. April, p. 137461, 2019.

ANEXX

Chemical characterization of TaCaP_Zn4, TaCaP_Zn6 and TaCaP_Zn7 samples was made by EDS (Figure 16 A to C) in order to qualitatively access the presence of Zn in the referred surfaces after the deposition of the NPs.

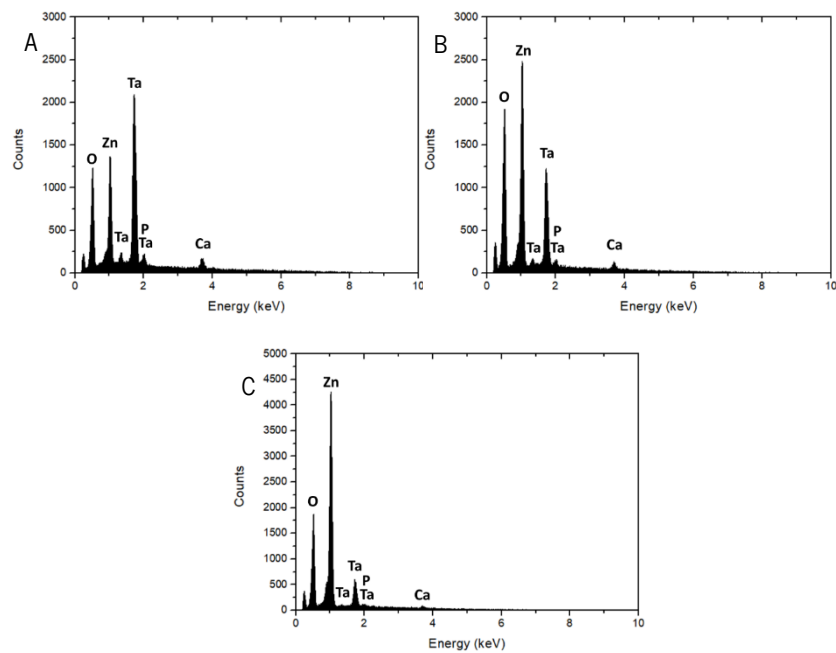


Figure 16 - EDS spectra of A) TaCaP_Zn4, B) TaCaP_Zn6 and C) TaCaP_Zn7 samples.

Annex 3: First Draft of Paper 2

Corrosion behavior of biofunctionalized Ta surfaces under artificial saliva

C. Rebelo, J. Castro, C. F. Alves, L. Fialho, S. Carvalho
Universidade do Minho, Campus de Azurém, 4804-533 Guimarães, Portugal
CEMMPRE Mechanical Engineering Department, University of Coimbra, 3030-788 Coimbra, Portugal

Abstract— There are some problems associated with the dental implants suffering corrosion after placement, thus compromising their function. Furthermore, there are also some problems associated with the dental implants being rejected by the body because of poor osteointegration between the implant surface and the bone and consequently bacterial growth. There are some ways to improve the osteointegration implant surfaces and inhibit the bacteria adhesion on its surface, by modifying them chemical and physically. This study is focused on the study of the corrosion behavior of Tantalum surfaces modified firstly by plasma electrolytic oxidation with incorporation of Calcium and Phosphorus and secondly with Zn(O) nanoparticles (with and without a Carbon layer) deposited by magnetron sputtering. The first modification intends to improve the osseointegration rate by mimetic the morphology and chemical composition from the bone. The NPs will add a new functionality: antimicrobial activity. The results obtained from the studies carried on that Tantalum surfaces revealed that the plasma electrolytic oxidation with incorporation of Calcium and Phosphorus was successful mimicking the morphology and the chemic of the bone, obtaining a porous surface with osteoblastic elements. Regarding the corrosion resistance, results showed that the Zn(O) nanoparticles led to a decrease in the corrosion resistance of the samples, however, their corrosion resistance improved as the immersion time increased, due to the Zn release.

Keywords—Tantalum, Calcium, Phosphorus, Zinc nanoparticles, Biofunctionalization, Corrosion resistance

I - INTRODUCTION

Teeth are an important part of human anatomy, because of their role in chewing and their aesthetic. However, there are health problems, such as gingivitis, diabetes, caries, and poor diet which can lead to tooth loss. Consequently, arises the requirement to create implants capable to replace missing teeth [1]. In the long-term, implant failure due to biological complications is common. Particularly, peri-implantitis disease stands out, which can be generically defined as an infection in the implant adjacent tissues, caused by the accumulation of bacteria (biofilm) on the implant surface causing the regression of the bone tissue [2][3][4]. Moreover, another problem associated with the failure of dental implants is the degradation of the implant's metal, triggered by the corrosion of its surface in a physiological environment (e.g. saliva and blood) [5].

Nowadays, titanium-based (Ti) dental implants are the most commercialized. However, in some cases, their biocompatibility is not sufficient to guarantee the rapid osseointegration of the implant which increases the probability of entrance of microorganisms near the implant surface, that can initiate infection and, consequently, culminate in implant failure [6]. Furthermore, although Ti and its alloys are considered corrosion-resistant materials due to the stability of the passive titanium oxide (TiO₂) film, this oxide can be

degraded when put under particularly aggressive *in vivo* conditions. When it is in contact with plasma from the blood due to chloride ions (Cl^-), local corrosion is induced and metallic ions from the passive film are released, being more dangerous and harder to predict than uniform corrosion [7][8][9]. Regarding dental implants, the corrosion of the metallic implants is exponentiated not only by Cl^- ions but also by fluoride and hydrogen ions (F^- e H^+), all of them present in saliva. Furthermore, fluoride ions are used very frequently to prevent caries, which may induce the degradation of Ti (and its alloys) dental implants [10]. The corrosion of materials used in implants is affected by several different factors, such as the material itself (chemical composition, microstructure, and surface features) and the pH of the surrounding environment. Regarding pH of the dental implant's surrounding environment, it varies between 5.3 and 5.6 right after surgery, stabilizing at 7 afterward. However, due to several factors such as tobacco, food, and oral hygiene, the pH near the implant can vary between 3 and 9 significantly influencing the corrosion behavior of Ti implants [8][9][11]. Furthermore, regarding the microstructure and surface features of the material, it is reported that Ti corrosion behavior is directly associated with the existence of pores and their size and morphology, the oxide thickness, and the Ti ability to self-heal or passivate [12].

Corrosion and degradation of dental implants can lead to the release and accumulation of corrosion products in the peri-implant tissues which can trigger inflammatory reactions and can induce and/or promote the occurrence of peri-implantitis disease, culminating in the loss of bone tissue adjacent to the implant [7][10]. Thus, the corrosion resistance of dental implants directly dictates its failure or its success.

To solve these limitations associated with the commercialized Ti-based implants, processes of surface modification of Ti are being reported. Surface bioactivity can be enhanced by modulating its topographic and chemical properties through their modification by electrochemical and physical processes. Thus, the topographical modification of Ta surfaces, promoting micro/nano-porous structures, can improve osseointegration, since the micro/nano-pores bring to the surface morphology similar to the human bone morphology, favoring cell adhesion. The incorporation of constituent elements of bone (osteoconductive elements), like calcium (Ca) and

phosphorus (P), also favors osseointegration, once it mimics the chemical composition of the bone [1][13]. Moreover, the presence of particles with antimicrobial properties, like zinc oxide (ZnO), reduces bacteria adhesion and, consequently, reduces the probability of infection and inflammation of the adjacent tissues to the implant [14][15]. Another strategy being studied is the replacement of Ti implants by other biocompatible metals, such as Ta, since this metal is very resistant to the ions responsible for the corrosion of Ti dental implants, specially to the F^- ion [16][17].

Thus, tantalum (Ta) has been studied as a viable option as a replacement for Ti. Ta and its oxides ($\text{Ta}_{1-x}\text{O}_x$) have shown to be promising since they are biocompatible and bioactive (both *in vivo* and *in vitro*), with high corrosion resistance [1][18][19].

In the work reported in this paper, the objective is to study the corrosion behavior of previously optimized [reference to "article proposal 1"] antimicrobial tantalum-based surfaces, modified by PEO to mimic the morphology and chemical composition of the human bone, and by magnetron sputtering with the incorporation of Zn(O) to enhance the antimicrobial activity of the surfaces.

II – MATERIALS AND METHODS

1 – Plasma eletrolytic oxidation

Plasma electrolytic oxidation (PEO) was performed on an anodization system, consisting of a DC power supply (Agilent N5751A), a multimeter (Agilent 34450A 5 1/2 Digit), and an electrochemical cell. Tantalum square samples (99,95% purity, Testbourne) measuring $20 \times 20 \text{ mm}^2$ were used as the substrate for the PEO process. The samples were first ultrasonically cleaned for 5 minutes in ethanol and in distilled water and air-dried at room temperature. Then, the PEO technique was performed on the samples in potentiostatic mode at 200 V, using an electrolyte composed of 0,35 M of calcium acetate ($\text{C}_4\text{H}_6\text{CaO}_4$, 99%, Biochem, Chemopharma) and 0,12 M of β -glycerol phosphate pentahydrate salt disodium ($(\text{HOCH}_2)_2\text{CHOP(O)(ONa)}_2 \cdot x\text{H}_2\text{O}$, 98%, Sigma-Aldrich), in agitation during 30 minutes at room temperature. In the electrochemical cell, the anode, corresponding to the Ta sample, and the cathode, corresponding to a graphite rod, were kept at a constant distance of 30

mm. After treatment, the samples were washed in distilled water and dried at room temperature. These samples were called TaCaP.

2 – Magnetron Sputtering

Magnetron sputtering technique in non reactive mode was used to deposit Zn nanoparticles on the TaCaP samples (substrates), using a 200x100x6 mm³ Zn target of high purity (99,99%, Testbourne). To assure a homogeneous distribution of the nanoparticles, the sample-holder was kept in constant rotation, at 7rpm. From previous works [reference to “first draft of paper 1”], two different deposition conditions, presented on Table 1, were used to obtain different amounts of nanoparticles with different sizes and morphology. The samples were designated TaCaP_Zn1 and TaCaP_Zn2.

Additionally, with the objective of controlling the Zn²⁺ ions release, a carbon layer was deposited over the Zn nanoparticles. For that, C₂H₂ gas was used as a carbon precursor. The deposition chamber was connected to a DC power source to dissociate the C₂H₂. The carbon layer was deposited using a current of 0.4 A and a pressure of 3 Pa at a frequency of 200 kHz for 60 seconds. The atmosphere in the chamber was formed by a flow of 80 sccm of Ar and 20 sccm of C₂H₂. The samples were named TaCaP_Zn1C and TaCaP_Zn2C, and stored in the desiccator.

Table 1 - Deposition parameters of Zn nanoparticles.

Designation	Pressure (Pa)	Current density (mA/cm ²)	Time (s)
TaCaP_Zn1	6.3	0.5	1000
TaCaP_Zn2	2.0	1	500

3- – SEM-EDS

The Scanning Electron Microscopy technique (SEM) allows the obtainance of micrographs of the samples under study, in order to study their morphology. The Scanning Transmission Electron Microscopy (STEM) allows the identification of the elements present in the chemical composition of the samples. Thus, SEM using an ultrahigh-resolution scanning electron microscope (Nova NanoSEM 200 microscope, FEI) at 5 kV in secondary mode was used to characterize the Zn nanoparticles deposited. In the particular case of

the samples with a carbon layer, the analysis was performed at 10 kV in secondary mode. The EDS technique was performed using a EDAX- Pegasus X4M (EDS/EBSD) spectrometer, operating at 10 kV, to study the qualitative chemical composition of the samples under study.

4 - ICP-OES

The inductive coupled plasma optical emission spectroscopy (ICP-OES) technique was used to measure the release of Zn²⁺ ions from the samples. To perform this technique, the samples were immersed in 50 mL of phosphate-buffered saline (PBS) solution for 2, 24, and 48 hours, and 7, 14, and 30 days. The amount of Zn²⁺ ions leached into the PBS was diluted in HNO₃ (2%), in a ratio of 1:3 and measured 3 times for each time-point by ICP-OES (ICP PerkinElmer spectrometer model Optima 8000). The calibration curve (Figure 1) was performed using a Zn standard solution (Sigma-Aldrich, 1000 mg/L) prepared in different concentrations of HNO₃ (2%).

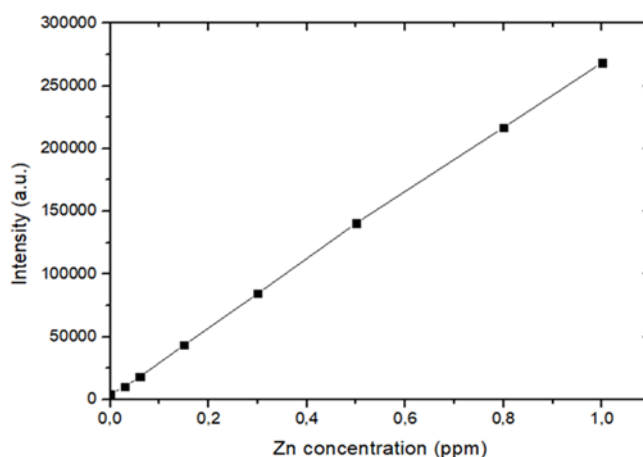


Figure 1 - ICP-OES calibration curve.

5 - Corrosion tests

To access the corrosion behavior of the different samples produced, each group of samples was subjected to open circuit potential (OCP), electrochemical impedance spectroscopy (EIS), and potentiodynamic polarization tests. A potentiostat (Gamry Instruments REF600) controlled by software (Gamry Instruments Framework REF14048) was used for this purpose. Samples were set up on a standard 3-electrode electrochemical cell with an exposed

sample area of 0.20 cm². In each test, a saturated calomel electrode (SCE) was used as the reference electrode, while a platinum electrode served as the counter electrode and the sample under study as the working electrode. Thus, the untreated Ta samples (used as control) and the samples from the 5 groups of modified Ta surface (TaCaP, TaCaP_Zn1, TaCaP_Zn2, TaCaP_Zn1C, TaCaP_Zn2C) were immersed in 200 mL of modified artificial saliva prepared according to Fusayama [20]: (0,4g/L NaCl, 0.4g/L KCl, 0.795 g/L CaCl₂·2H₂O, 0.005g/L Na₂S₉H₂O, 0.69g/L NaH₂PO₄·2H₂O e 1g/L urea) with a pH of 5.50. The artificial saliva was maintained at 37 °C using a heating and circulation system of water on the outside of the electrochemical cell and its pH was kept using buffer solutions. Each sample was tested after 2, 24 and 48 hours, 7 and 14 days of immersion in artificial saliva. Firstly, OCP was measured and allowed to stabilize for 1 hour at the first time point (2 hours of immersion) and for 30 minutes at the other time points. Therefore, EIS measurements were performed in a frequency range from 0.01 Hz to 10⁵ Hz, with an AC sinusoidal perturbation with an amplitude of 10 mV (rsm), relative to the OCP applied to the electrode. In addition, after both 14 days of immersion and immediately after immersion (0 hours), potentiodynamic tests were performed, using a scan rate of 60 mV/min, from -3 V vs. OCP to +1.2 V vs. OCP. Every analysis was performed in triplicate.

5 – STEM/EDS

A STEM/EDS cross-sectional characterization of the oxide layer will be performed to obtain an elemental mapping and morphological assessment of the porous Ta₂O₅ layer of the modified samples. This characterization will provide a better understanding of the oxide features that can explain the corrosion behavior of the surfaces.

III – RESULTS AND DISCUSSION

1 – Morphology and chemical characterization of the developed samples

SEM micrographs of a Ta sample (without any treatment) (Figure 2 A) and micrographs from the functionalized PEO sample (TaCaP, Figure 2 B) show that the PEO technique results in the formation of pores of different sizes and diameters on the treated Ta surface (TaCaP), which approximates the surface morphology of this sample to that of human bone [21]. Moreover, the comparison between both Ta and TaCaP EDS spectra (Figure 2 C and D) prove the incorporation of Ca and P into the oxide layer.

Figure 3 A and B presents presents SEM micrographs of the TaCaP_Zn1 and TaCaP_Zn2 samples. Through the observation of the micrographs, it is possible to observe that in both samples, the nanoparticles are present in the surface of the samples, as well as in the interior of the pores, without compromising the porous morphology achieved by the PEO technique. Furthermore, the micrographs show differences on the morphology and size of the deposited nanoparticles in each samples. The NPs on the TaCaP_Zn1 sample are smaller and more rounded shaped than the ones on the TaCaP_Zn2 sample. Furthermore, the TaCaP_Zn2 sample seems to have a greater amount of NPs deposited, comparing to the TaCaP_Zn1 sample. Regarding the effect of the carbon layer on the surfaces morphology, it is possible to observe on Figure 3 C and D that the carbon layer encapsulates the NPs when compared with the TaCaP_Zn1 and TaCaP_Zn2 samples, without compromising the micro/nano-porous structure of the samples. Although the SEM images allow to take some conclusions about the amount, size, and morphology of the deposited NPs, these conclusions are only qualitative, once the size and morphology of the NPs do not allow a quantitative analyze, due to the reduced size of the nanoparticles and the coalescence of the bigger particles. Thus, the selected samples, as well as a TaCaP_CD sample serving as control, are analyzed by ICP-OES to study the release of Zn²⁺ ions from the surfaces.

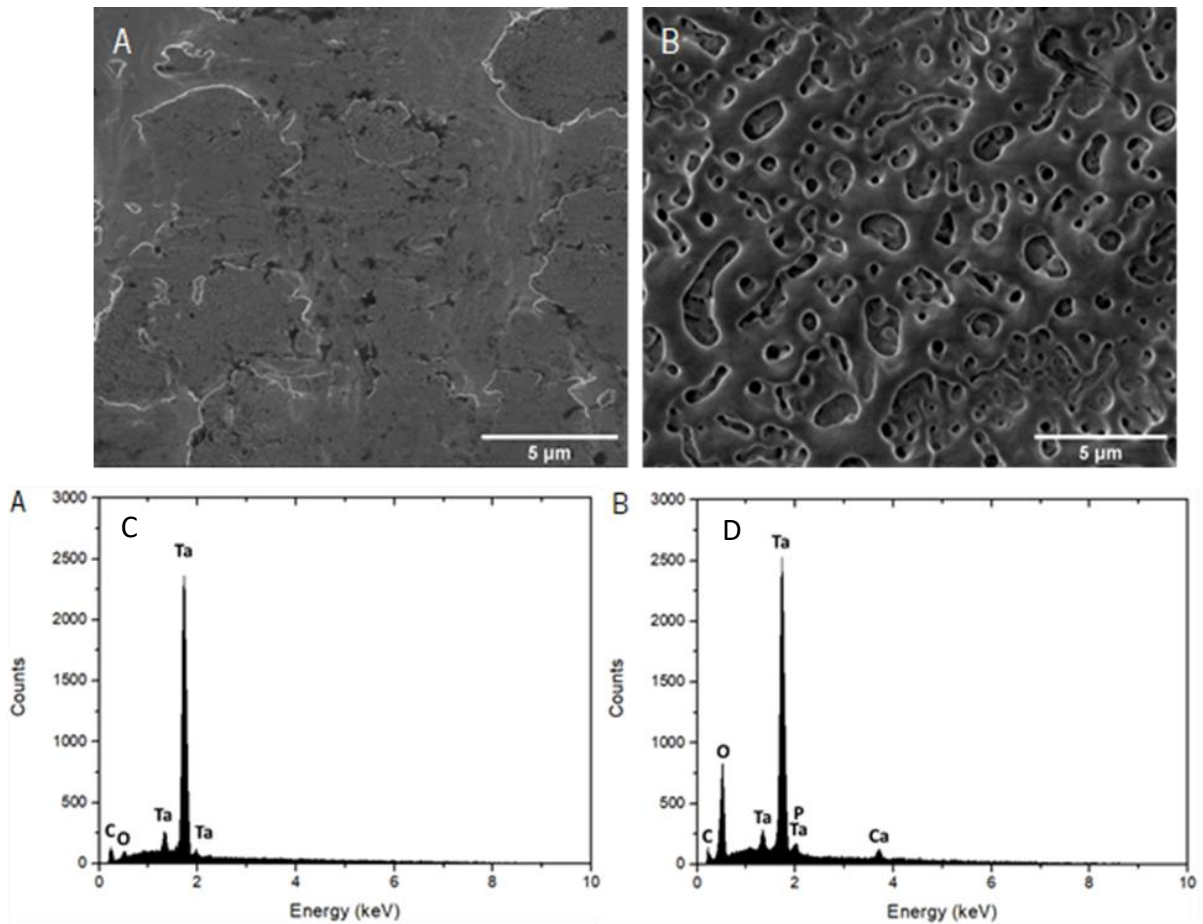


Figure 2 - SEM micrographs of A) Ta and B) TaCaP and EDS spectra of C) Ta and D) TaCaP samples.

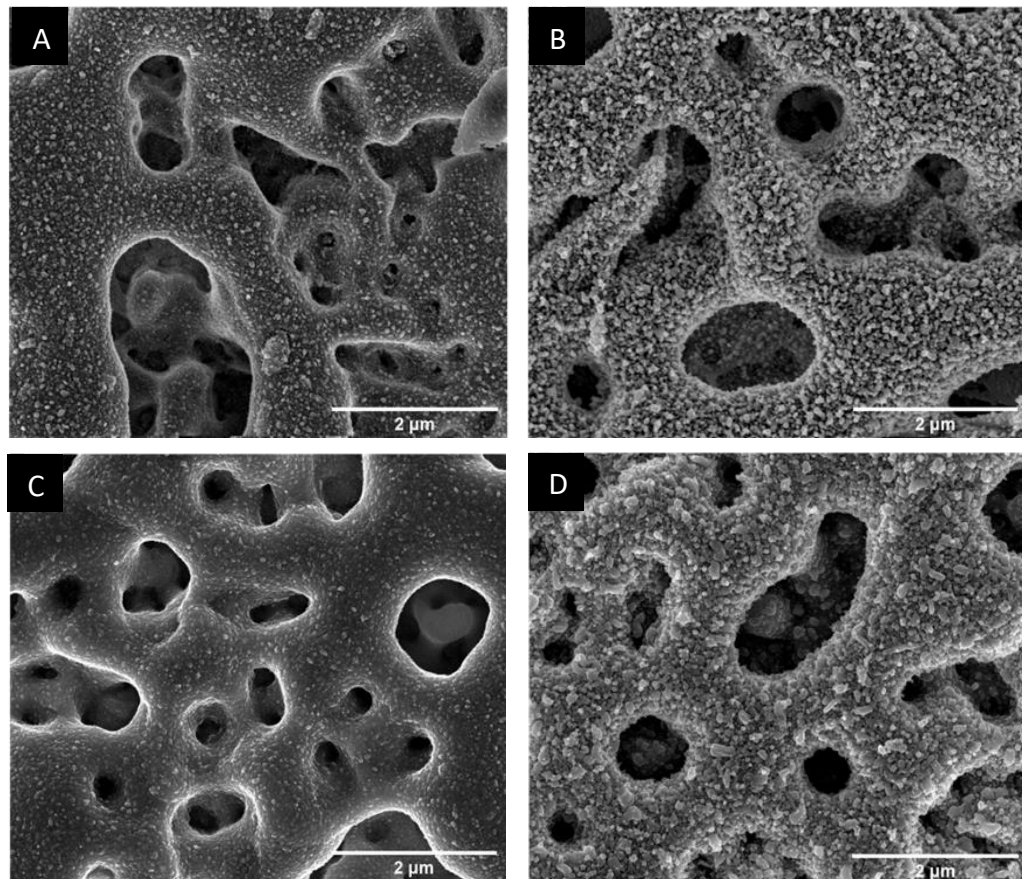


Figure 3 - SEM micrographs of A) TaCaP_Zn1, B) TaCaP_Zn2, C) TaCaP_Zn1C and D) TaCaP_Zn2C samples.

Figure 4 presents the ICP-OES results of each sample in study after 2, 24 and 48 hours, 7, 14 and 30 days of immersion in PBS. Both the samples with the carbon layer (TaCaP_Zn1C and TaCaP_Zn2C) and the samples without carbon layer (TaCaP_Zn1 and TaCaP_Zn2) show the same trend of Zn^{2+} ion release profile, with the largest amount of ions being released between the first 2 and 24 hours of immersion and no significant Zn^{2+} release observed thereafter. The sample that presents higher concentration of Zn^{2+} ions release is TaCaP_Zn2 (3.96 ± 0.04 ppm), while TaCaP_Zn1 shows a much lower concentration (0.95 ± 0.01 ppm), proving that the sample with greater amount of Zn NPs is the TaCaP_Zn2, as is observed by the SEM micrographs. The presence of the carbon layer results in a decrease in the release of Zn^{2+} ions as the released zinc ions concentration is lower for TaCaP_Zn1C and TaCaP_Zn2C than TaCaP_Zn1 and TaCaP_Zn2 samples, respectively. This behavior remains after 30 days of immersion in PBS. Thus, it suggests that some of the Zn NPs are still encapsulated by the C layer, however they not have mobility on the carbon layer meaning that cannot be released.

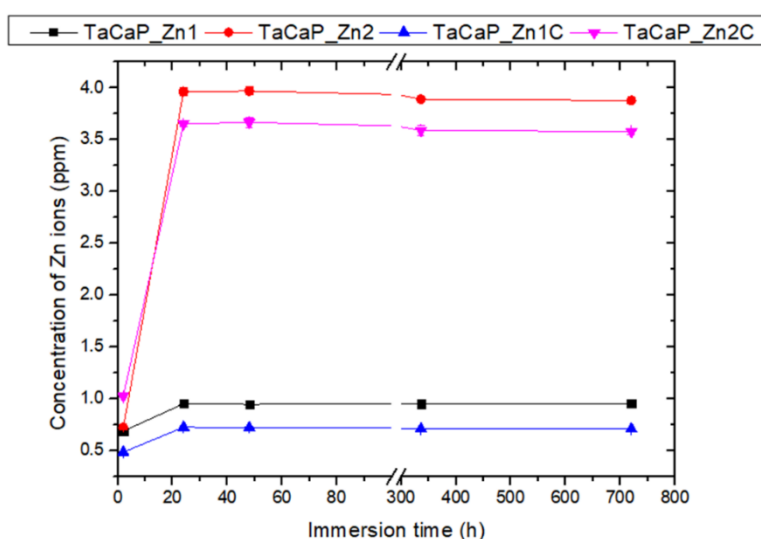


Figure 4 - Zn^{2+} ion release profile for TaCaP_Zn1, TaCaP_Zn1C, TaCaP_Zn2 and TaCaP_Zn2C samples.

2 – Corrosion behavior

Dental implants are subject to corrosion since the saliva can be a corrosive environment. Thus selected samples (TaCaP, TaCaP_Zn1, TaCaP_Zn2, TaCaP_Zn1C, TaCaP_Zn2C), and untreated Ta sample (as a control), are subjected to

potentiodynamic, open circuit potential (OCP) and electrochemical impedance spectroscopy (EIS) tests in artificial saliva for several time-points.

After the modification treatments that the Ta sheet had suffered, the achieved surfaces exhibit changes that can be crucial for the OCP behavior. These changes are: the oxide formation, incorporation of Ca and P by the PEO functionalization; the amount and size of Zn NPs deposited on the surfaces of the samples, and finally the roughness achieved with the formation of micro/nano-porosity during the PEO process and by the deposition of Zn NPs and carbon layer. Figure 5 shows the OCP value for each sample as a function of immersion time in artificial saliva, at 37 °C, after 2, 24, and 48 hours, 7 and 14 days.

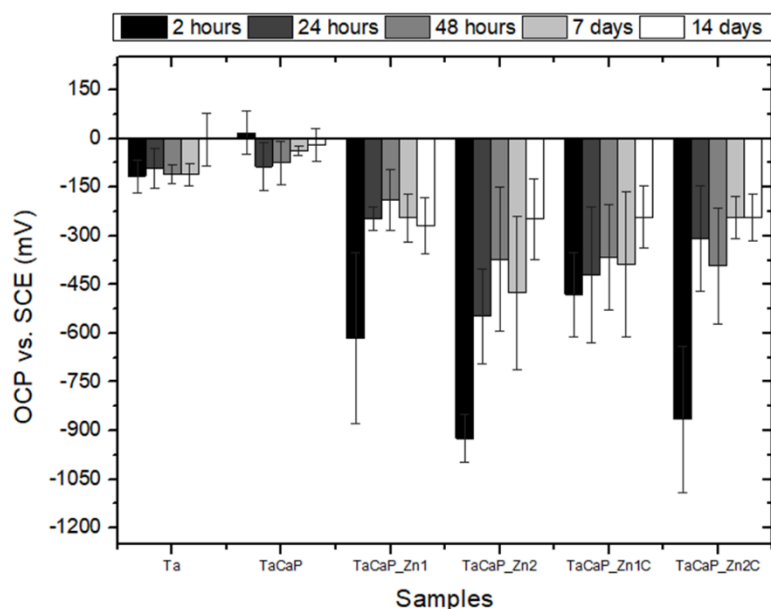


Figure 5 - OCP vs. SCE values for the 5 studied time-points.

Generally, all the samples exhibit a negative OCP. The Ta control sample reveals a constant OCP value between 2 hours and 7 days of immersion. At 14 days of immersion, a slight increase in OCP value is recorded, suggesting slight passivation of the surface. On the other hand, a decrease in OCP behavior is observed in the TaCaP sample between 2 and 24 hours of immersion, possibly related to the reactivity of the Ca^{2+} and PO_4^{3-} ions resulting from the Ca and P embedded into the oxide layer with the artificial saliva solution. From 24 hours to 14 days, the OCP value slightly increase and stabilize, indicating a slight improvement in the corrosion behavior of this sample. Generally, the addition of Zn NPs to the samples'

surface leads to a clear decrease in the OCP values, meaning a worst corrosion behavior, which was expected as the Zn NPs are metallic elements. In the particular case of the TaCaP_Zn1 sample, a significant increase in OCP value is observed between 2 and 24 hours after immersion. Thereafter, the sample shows a tendency to stabilize the OCP values without showing significant differences in the remaining time-points. The same tendency is observed for TaCaP_Zn2 and TaCaP_Zn2C samples. The increase in OCP values observed in these 3 samples between 2 and 24 hours after immersion could be attributed to the release of Zn NPs from the surface in this time interval with the electrolyte, as the largest amount of Zn^{2+} ions released from these surfaces, determined by ICP, occurs in this time interval (Figure 4). Therefore, the samples become less active. In opposite, TaCaP_Zn1C sample reveals a different corrosion behavior since the OCP value at 2 hours of immersion is higher than all the other Zn-containing samples and the increase in OCP value between 2 and 24 hours after immersion is much less significant than the other Zn-containing samples. This can be explained by the fact that, in this case, the carbon layer deposited over the Zn NPs may reduce the interaction between the NPs and the electrolyte, inhibiting the Zn^{2+} release, making the surface more inert due to the inert character of C. Although C is inert, the same effect is not verified in the TaCaP_Zn2C sample, where the effect of the interaction between the Zn NPs with the electrolyte is dominant and outweighs the effect of the C layer. This behavior may be related to the size and morphology of this sample's NPs (Figure 3 D), which are much larger and more irregular than those in the TaCaP_Zn1C sample (Figure 3 C).

As observed in Figure 2 B, the PEO treatment induces a porous structure with non-homogeneous distribution and dimension. Consequently, due to substrate heterogeneity, the deposition of the nanoparticles occurs in preferential nucleation points (Figure 3 A and B). Therefore, the heterogeneity of the surface explains the error values associated with the experimentally determined OCP values.

Figure 6 shows the plotted potentiodynamic curves of the analyzed samples immediately after immersion (0h) and after 14 days of immersion. Immediately after immersion (Figure 6 A), it is visible that the sample with the lowest current density rate (i_{corr}) is the TaCaP

sample (red line), indicating that corrosion occurs at a lower rate on this surface when compared with the others. On the other hand, TaCaP_Zn2 is the sample that shows the highest current density (pink line), meaning that the corrosion rate is faster, probably due to the higher amount of Zn NPs in this samples when compared with the TaCaP_Zn1 sample. Comparing all the samples with the Ta control, it seems like the surface modification by PEO slows down the corrosion rate, while the deposition of NPs leads to an increase in the system electrochemical reactivity. The presence of the carbon layer slightly decreases the current densities of the coated samples in comparison with the non-coated ones, which comes in agreement with the fact that the more inert C layer covers the NPs, observed by SEM (Figure 3 C and D). Regarding the corrosion resistance, estimated by the E_{corr} value of the potential vs. SCE, Ta and TaCaP samples are the ones with the best behavior, showing the higher values, which is expected and in agreement with the OCP behavior, since those are the only samples without metallic NPs on their surfaces. The potentiodynamic curves at 0 hours also reveal the existence of pitting corrosion on the TaCaP_Zn1, TaCaP_Zn2, and TaCaP_Zn2C samples.

After 14 days of immersion (Figure 6 B), Ta sample shows a slight improvement in the corrosion behavior, presenting a higher E_{corr} value and no significant change in the corrosion rate. On the other hand, TaCaP sample does not show significant changes in the corrosion rate, presenting nearly the same current density as at 0 hours of immersion, nor in the corrosion resistance, which may indicate that this sample is stable throughout the time. Furthermore, the potentiodynamic curves reveal clear changes either in terms of corrosion rate (i_{corr}), either in terms of corrosion resistance (E_{corr}) of the Zn-containing surfaces (TaCaP_Zn1, TaCaP_Zn2, TaCaP_Zn1C, and TaCaP_Zn2C). Indeed, after 14 days, Zn-containing surfaces present a more passive behavior (higher E_{corr} value) and a lower corrosion rate (lower i_{corr}) compared to the immediately after immersion curves (Figure 6 A). These results show that after 14 days of immersion, the Zn-containing samples tend to approximate their behavior to the behavior exhibited by the TaCaP sample, due to the loss of the Zn NPs throughout the immersion time, becoming less active. Moreover, the deposition of the C layer leads to a more significant improvement in the corrosion resistance of

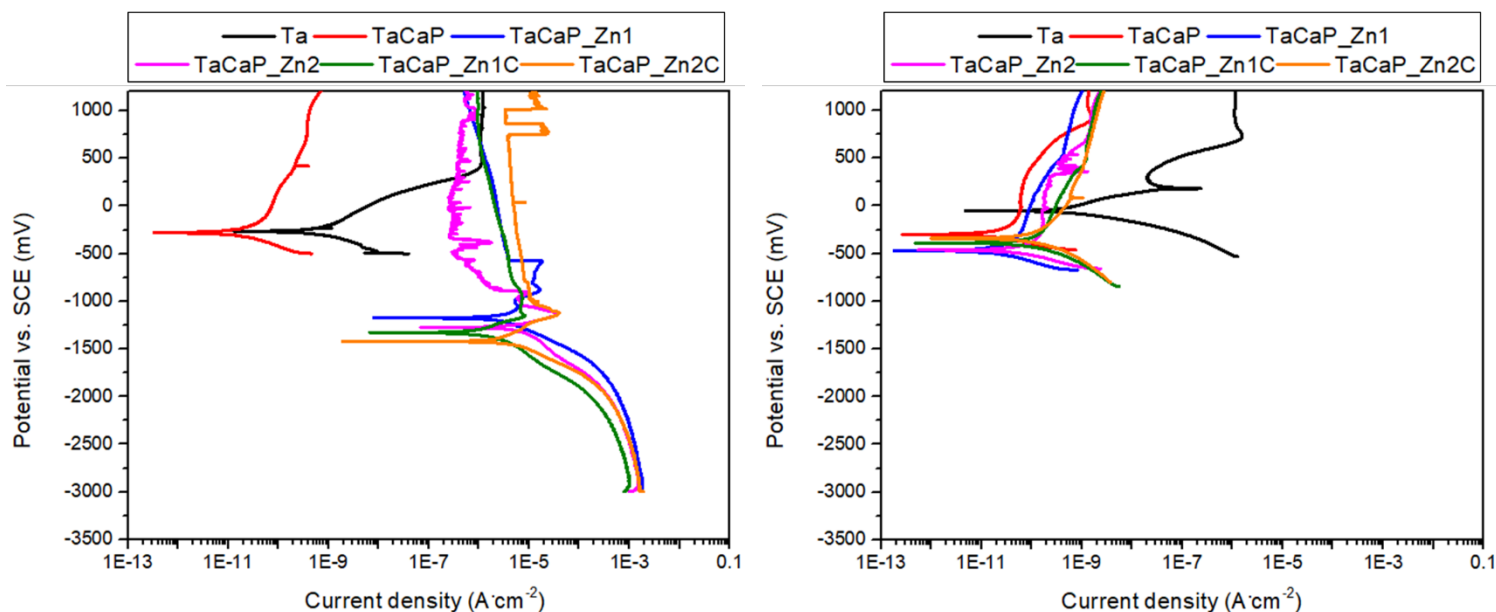


Figure 6 - Potentiodynamic curves A) immediately after immersion (0h) and B) 14 days after immersion.

the TaCaP_Zn1C and TaCaP_Zn2C samples after 14 days of immersion, when compared to the improvement achieved by the TaCaP_Zn1 and TaCaP_Zn2 samples.

To characterize in detail the corrosion performance of the samples, electrochemical impedance spectroscopy is performed. Bode and Nyquist plots for all the developed samples, as well as a Ta control sample, after 2, 24 and 48 hours, 7 and 14 days of immersion in artificial saliva are presented from Figure 7 to 9 and in Figure 10, respectively. It is important to notice that for the first 2 hours of test, the TaCaP_Zn2 and TaCaP_Zn2C samples are not represented, because, in all the 3 replicas tested, for that time of

test the system is not capable to reach a stabilized point to take any conclusion on the corrosion behavior of these samples.

Generally, Ta control sample shows a capacitive behavior with a single time constant while TaCaP sample shows 2-time constants through all the studied immersion times, as it is possible to see in the Bode plots from Figure 7. Furthermore, it is possible to observe that both samples do not suffer much significant changes on their impedance modulus ($|Z|$) as the immersion time increases, indicating that these samples are already electrochemically stable before the EIS experiment starts, specially the TaCaP sample, which presents higher values of impedance modulus,

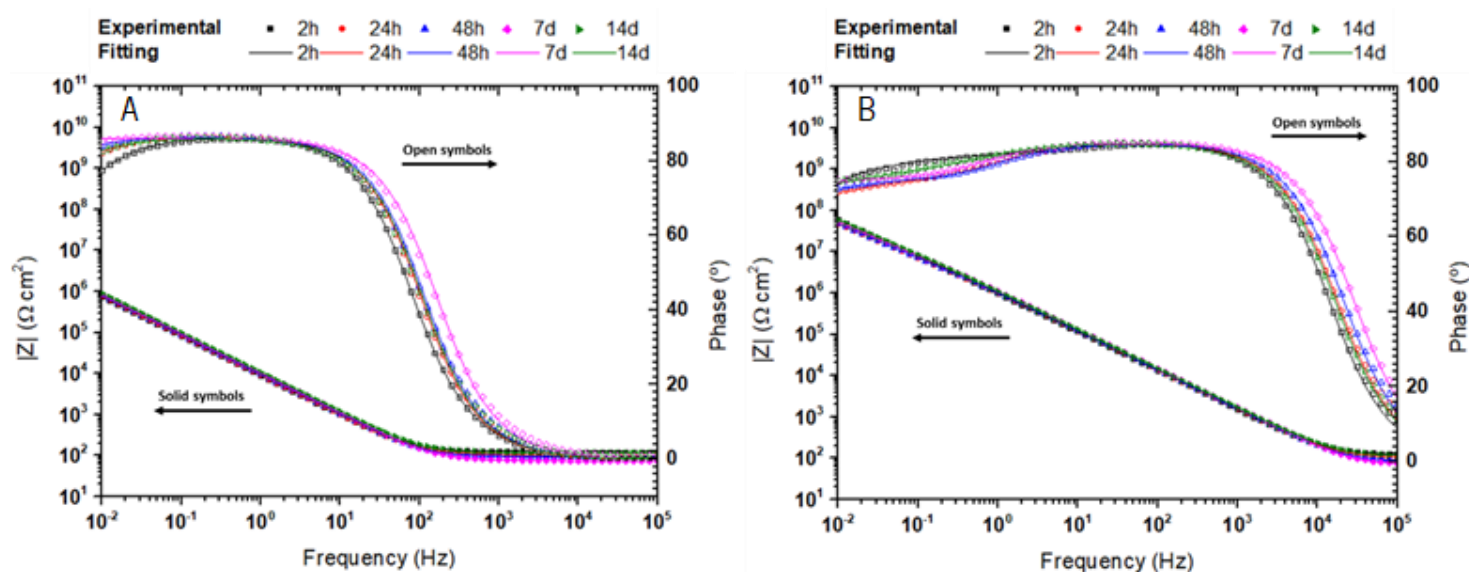


Figure 7 - Bode plot of A) Ta and B) TaCaP samples after 2, 24, and 48 hours, 7 and 14 days of immersion in artificial saliva at 37°C. (Measured (symbols) and fitted (lines) values of impedance modulus are related to the left axis while the measured (symbols) and fitted (lines) values of phase are related to the right axis).

thus indicating a better electrochemical response from this sample. Such fact may be explained by the formation of the oxide layer promoted by the PEO technique.

Analyzing the Bode graphs from Figure 8 and Figure 9 is possible to see that the samples with Zn NPs and the samples with Zn NPs and carbon layer show different behaviors compared with the Ta control and TaCaP samples, as well as along the immersion time. For the 2 and 24 hours of immersion, TaCaP_Zn1 sample (Figure 8 A) shows a diffusional behavior and after 48h of immersion, shows a 2-time constants

transitional behavior after the first 24 hours of immersion in saliva can be related with the results obtained in the ICP-OES (Figure 4), once after the first 24 hours of immersion in PBS there is no more significant release of Zn^{2+} ions from this surface, indicating that after those 24 hours of immersion this sample returns to its ground stage (TaCaP). This results also confirm the conclusions taken by the potentiodynamic curves analysis for this sample. On the other hand, although TaCaP_Zn1C sample (Figure 8 B) shows a similar kinetics of Zn^{2+} ion releasing as the TaCaP_Zn1 sample in the ICP-OES (Figure 4), this sample only shows diffusional behavior in the first 2

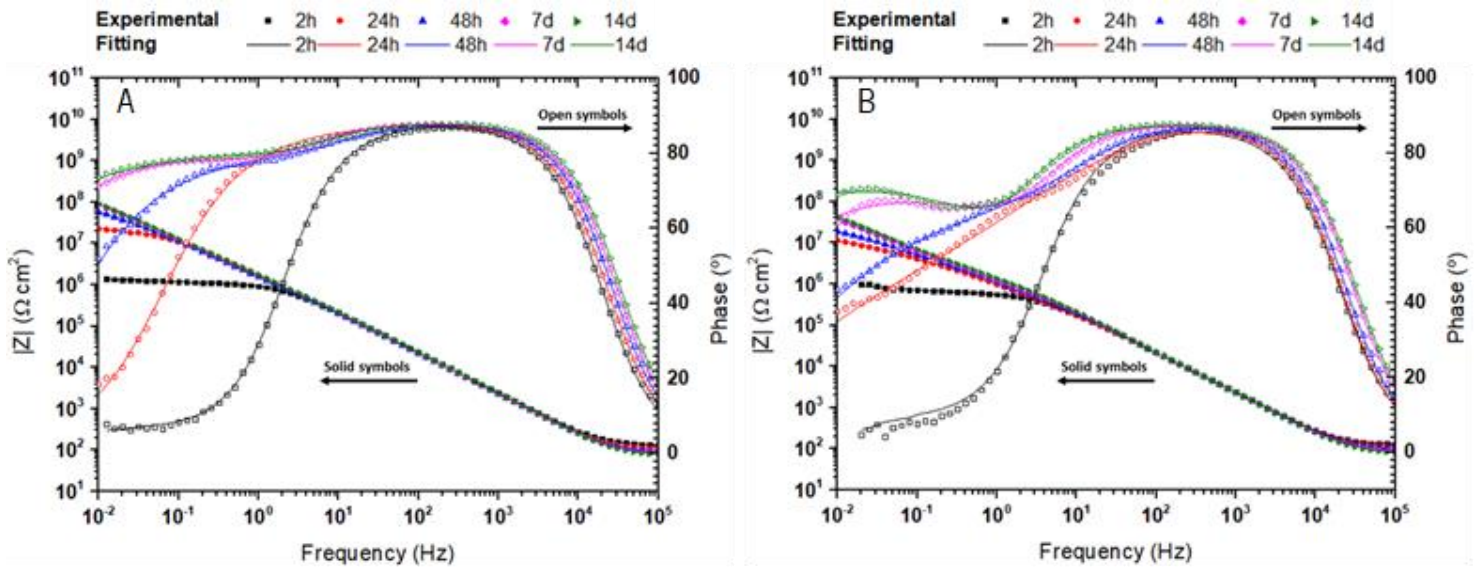


Figure 8 - Bode plot of A) TaCaP_Zn1 and B) TaCaP_Zn1C samples after 2, 24, and 48 hours, 7 and 14 days of immersion in artificial saliva at 37°C. (Measured (symbols) and fitted (lines) values of impedance modulus are related to the left axis while the measured (symbols) and fitted (lines) values of phase are related to the right axis).

behavior until the 14 days of immersion. This

hours of immersion, becoming represented by 2-time

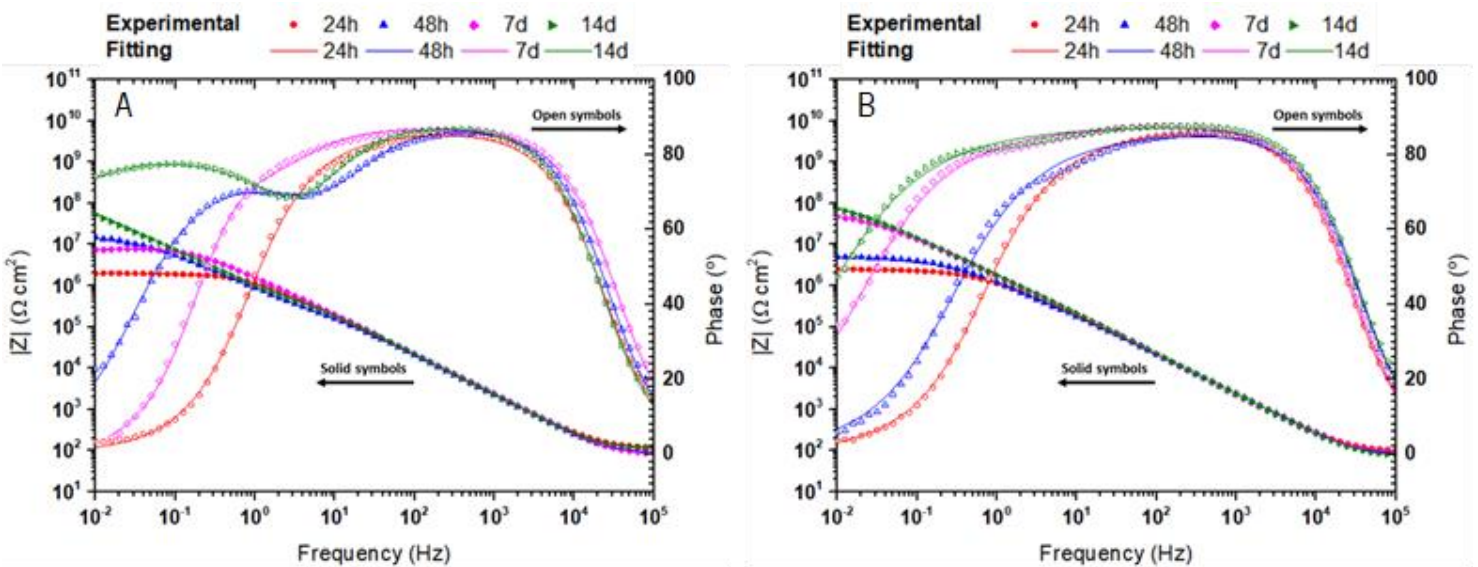


Figure 9 - Bode plot of A) TaCaP_Zn2 and B) TaCaP_Zn2C samples after 2, 24, and 48 hours, 7 and 14 days of immersion in artificial saliva at 37°C. (Measured (symbols) and fitted (lines) values of impedance modulus are related to the left axis while the measured (symbols) and fitted (lines) values of phase are related to the right axis).

constants afterwards. The faster release of Zn NPs in this case may be due to the fact that the ICP and the corrosion tests are performed using two different solutions, which, combined with the encapsulation of the NPs by the carbon layer, can affect the kinetics of ions releasing. Regarding the electrochemical response of these two samples, an improvement is achieved as a function of the immersion time, with $|Z|$ values increasing throughout the immersion time. After 14 days of immersion the electrochemical response of these two samples achieves values close to the ones of TaCaP sample, thus indicating once again the approximation of these surfaces to their ground stage as the NPs were being released from their surface.

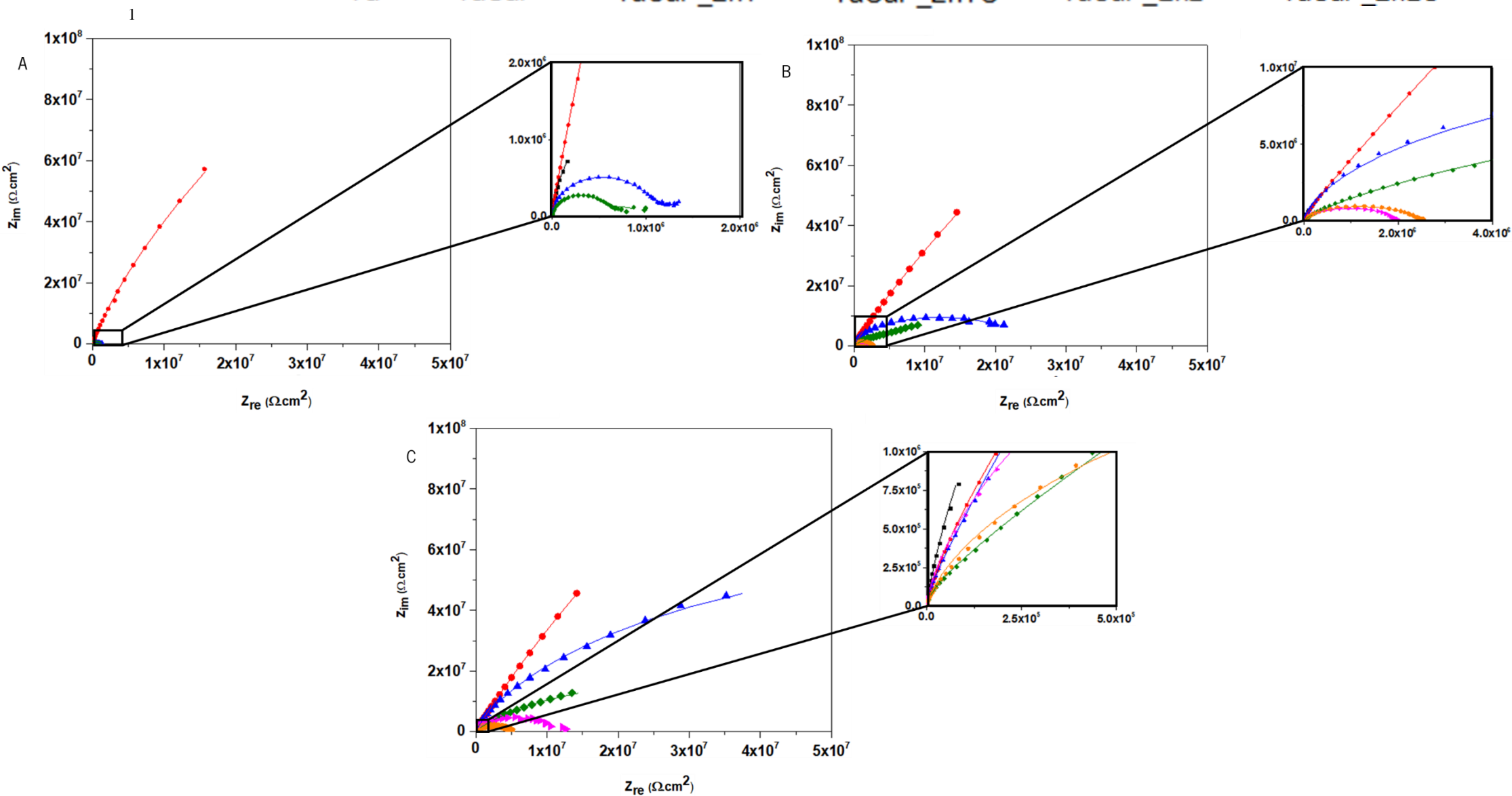
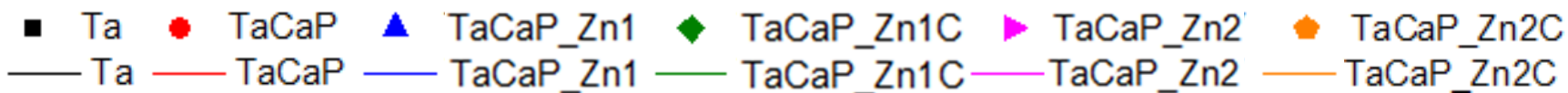
TaCaP_Zn2 (Figure 9 A) sample also presents diffusion at 24 hours of immersion and 2-time constants afterwards, like the TaCaP_Zn1 sample. Despite the 7 days of immersion curve (pink curve) seems to show diffusional behavior, the high α_2 value (0.86 ± 0.10) presented on Table 2 from the Anexx, indicates that there is no need to fit this curve using a W component, since the α_2 is high enough to not consider the effect of diffusion (normally considered for $\alpha_2 \approx 0.6$) in this time point. On the other hand, TaCaP_Zn2C (Figure 9 B) sample shows diffusion along all the immersion time, which somehow suggests that some Zn NPs remain in the surface after 14 days of immersion. Such theory is confirmed by SEM micrographs of this sample, after 14 days of immersion. In terms of impedance modulus, firstly at 24 hours of immersion, TaCaP_Zn2 and TaCaP_Zn2C samples show similar electrochemical behaviors between themselves, secondly, generally, their impedance modulus values increase throughout the immersion time. These results indicate a clear improvement on the corrosion behavior of the samples with NPs (TaCaP_Zn1 and TaCaP_Zn2) and with NPs and C layer (TaCaP_Zn1C and TaCaP_Zn2C) as a function of immersion time, with their behavior becoming more capacitive throughout the immersion time due to the Zn NPs release.

Regarding the impedance, in particular after the first 2 hours of immersion, Nyquist plot (Figure 10) reveals that the sample with the largest impedance is the TaCaP sample, proving the surface treatment benefit in corrosion enhancement, since the non-treated Ta control sample shows lower impedance values. On the other hand, the samples with lower impedance values

are the TaCaP_Zn1 and TaCaP_Zn1C samples, which is somehow expected as the NPs are electrochemical active metallic elements even though they have a pristine passive oxide layer. In good agreement, after 24 hours of immersion (Figure 10 B), TaCaP_Zn2 and TaCaP_Zn2C samples are the ones that show lower values of impedance thus, being the samples less resistant to corrosion. Such fact may be explained by the largest amount of Zn NPs present in these surfaces. On the other hand, as the immersion time increases (Figure 10 C to E), it is possible to see a stable behavior on the TaCaP sample impedance values, and an improvement on the corrosion resistance of the Zn-containing and the Zn-containing with C layer samples. TaCaP_Zn1 sample shows the greatest improvement of all samples, presenting much higher values of impedance from 48h of immersion to 14 days, when compared with the values at 2 and 24 hours of immersion.

.

Experimental
Fitting



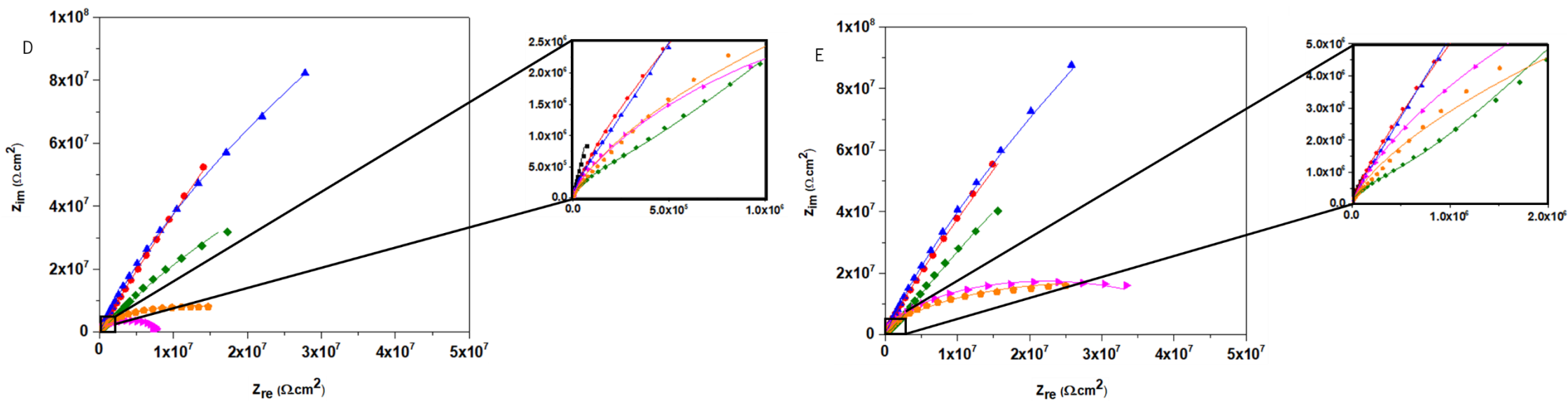


Figure 10 - Nyquist plot of Ta, TaCaP, TaCaP_Zn1, TaCaP_Zn1C, TaCaP_Zn2 and TaCaP_CaP2C samples after A) 2 hours, B) 24 hours, C) 48 hours, D) 7 days, and E) 14 days of immersion in artificial saliva at 37°C.

Figure 11 to 13 show the equivalent circuits (EC) used to fit the EIS results. Figure 11 represents the circuit used to fit the Ta control sample. In this circuit, already reported in the literature by other authors that study tantalum corrosion [22][23] a constant phase element (CPE) is used instead of a capacitance element to consider the roughness and heterogeneities of the surface. In the used EC, the R_{sol} element represents the resistance of the electrolyte, while the polarization resistance element, R_1 , represents the charge transfer resistance. Thus, the parallel connection between the CPE and the R_p elements represents the resistance and capacitance of the passive oxide film formed on the Ta surface. To fit the EIS results of the TaCaP sample, a circuit traditionally used by other authors to model porous surfaces [22] [24][25] (Figure 12) is used. In this case, the R_1 and Q_1 elements in parallel represent the interaction of the oxide layer formed by PEO with the electrolyte, while the R_2 and Q_2 elements, also placed in parallel, illustrate the substrate (Ta sheet). As Zn NPs and the carbon layer are added, it becomes more difficult to represent the behavior of such complex systems, as well as the circuits used to fit results within the same sample that also change throughout the different time-points studied due to the Zn NPs release. Regarding the TaCaP_Zn1 sample, for 2 and 24 hours of immersion, the used circuit (Figure 13) has a Warburg element (W) substituting the second CPE (Q_2) element present in the previously described circuit (Figure 12) to model the diffusion that occurs between the Zn NPs and the electrolyte. Afterwards, the EIS results are fitted using the same circuit as the TaCaP sample, because the diffusion effect of the NPs is no longer determinant, which may indicate that after the first 24 hours of immersion, the surface no longer releases NPs in significant quantities. The adopted approach of two different circuits before and after the first 24 hours of immersion is in good agreement with the ICP-OES results (Figure 4). When the carbon layer is added over the NPs (sample TaCaP_Zn1C), the same two circuits are used to fit the EIS results. However, the circuit from Figure 13 is only used to model the results from the first 2 hours of immersion because the effect of the diffusion between the NPs and the electrolyte is only observed at this time-point, afterwards the circuit used to fit the results is the same as TaCaP sample. EIS results for the first 2 hours of immersion from TaCaP_Zn2 and TaCaP_Zn2C samples are not possible to fit since any of the 3 replicas analyzed shown a constant behavior,

indicating that for these two samples, at this time-point, the system is not stable yet. Regarding the results for the remaining time-points, TaCaP_Zn2 sample shows a similar response as the TaCaP_Zn1 sample's response, with the circuit from Figure 13 being used to model this sample's behavior at 24 hours and the circuit from Figure 12 being used model the remaining time-points. On the other hand, all the EIS results from TaCaP_Zn2C samples are fitted using Figure 13 circuit, once the diffusional effect is observed along every time-point. This behavior indicates again that after 14 days of immersion this sample's surface still has nanoparticles. Thus, the SEM results (Figure 17) prove that after 14 days of immersion the carbon layer is still encapsulating some Zn NPs, controlling its release, which is a possible explanation why this sample shows a lower release of Zn^{2+} ions than the TaCaP_Zn2 sample after 14 days of immersion in PBS on the ICP-OES analysis.

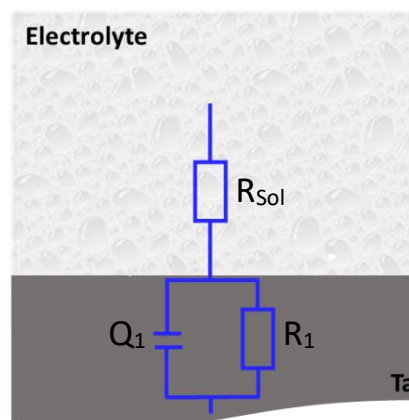


Figure 11 - Equivalent circuit used to fit EIS values of Ta sample.

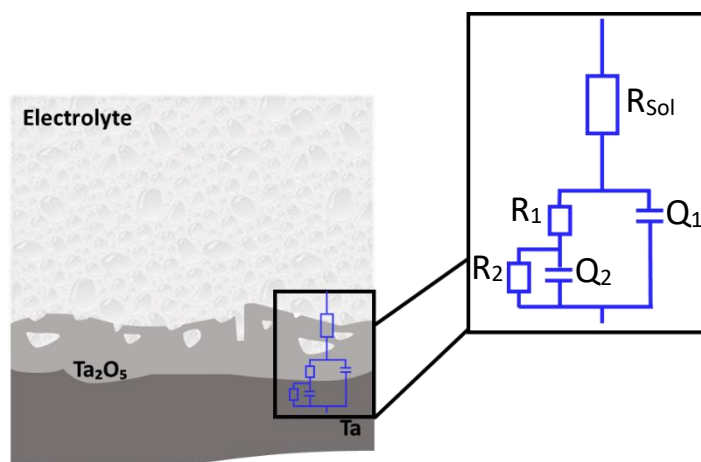


Figure 12 - Equivalent circuit used to fit EIS values of TaCaP sample and some time-points of TaCaP_Zn1, TaCaP_Zn1C and TaCaP_Zn2 samples.

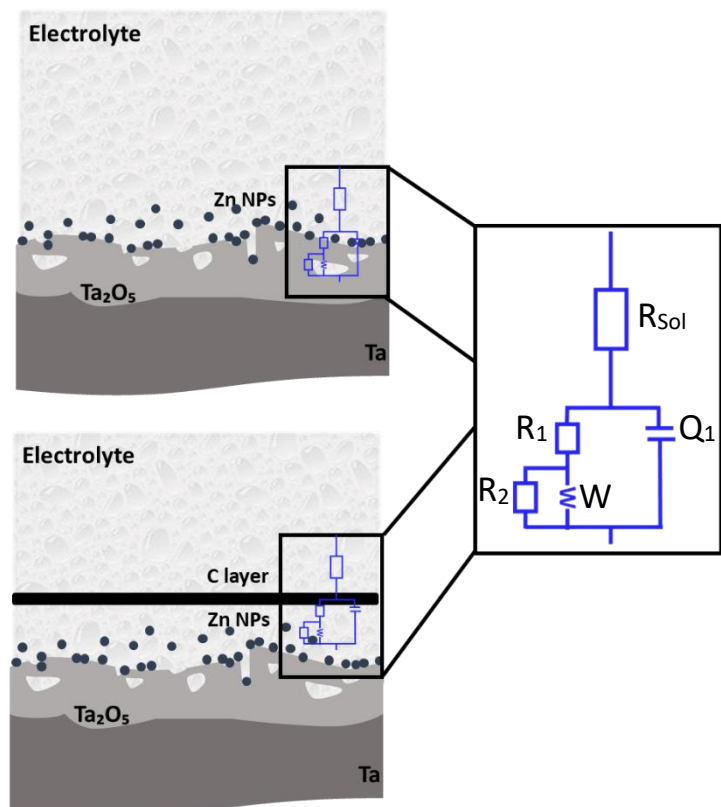


Figure 13 - Equivalent circuit used to fit EIS values of TaCaP_Zn2C sample and some time-points of TaCaP_Zn1, TaCaP_Zn1C and TaCaP_Zn2 samples.

Table 2 to 6, presented in annex 1, present the EIS data fitting results for every time-point studied. All the samples, for every time-point, present a goodness of fit in the order of 10^{-4} , except for the TaCaP_Zn2C sample at 24 hours and 14 days of immersion, which presents values of 2.28×10^{-3} and 1.33×10^{-3} respectively, which are still considered good fitting values. Regarding the resistance of the electrolyte, represented by R_{sol} , it is possible to observe on the tables that, generally, it has the tendency to decrease as the immersion time increases for every studied sample. On the other hand, the polarization resistance (R_p), given by the value of R_1 for the Ta control sample, and by the sum of R_1 with R_2 for all the other samples, shows a tendency to increase as a function of the immersion time, with R_p values from the TaCaP sample standing out when compared to all the other samples' values. This indicates the tendency for the samples' corrosion resistance to improve as a function of the immersion time. Thus, this behavior comes in agreement with what was concluded with the potentiodynamic curves analysis (Figure 6), where the sample with better corrosion behavior is the TaCaP and the Zn-containing and C

layered samples improve their behavior after 14 days of immersion.

To understand the effect of the corrosion tests on the morphology and chemical composition of the samples, SEM and EDS analyses of the TaCaP_Zn2 and TaCaP_Zn2C samples are presented below. Figure 14 A shows SEM micrographs of TaCaP_Zn2 sample after the potentiodynamic test performed immediately after immersion. It is possible to see that the porous morphology does not suffer significant changes after the test, while the nanoparticles seem to have changed morphology and agglomerate, looking very different from what they look like before the corrosion test (Figure 3 B). Furthermore, Furthermore, EDS spectra of Z1 and Z2 (Figure 14 B and C, respectively) prove that the structures observed in the SEM micrographs are Zn structures, since Zn is detected in the spectrum (Z1), and that there is no longer Zn in the porous structures (Z2).

After 14 days of immersion in artificial saliva and after the OCP, EIS, and potentiodynamic tests, TaCaP_Zn2 sample's SEM micrographs (Figure 15) show that this sample returns to its ground state (porous structure without Zn NPs). Thus, these results come in agreement with the results obtained from the potentiodynamic (Figure 6) and EIS (Figure 9 A) tests, where after 14 days of immersion this sample's corrosion behavior become similar to TaCaP sample's behavior.

Regarding the TaCaP_Zn2C sample, after the potentiodynamic test immediately after immersion, SEM micrographs (Figure 16 A) also demonstrate some tendency for the nanoparticles to agglomerate, however, their morphology is completely different from TaCaP_Zn2 sample's morphology (Figure 14 A), which may be due to their encapsulation by the carbon layer that may lead to the constraining of their mobility. Furthermore, EDS spectra from two different zones of this sample's surface (Figure 16 B and C) reveal that there is yet Zn distributed over all the surface, meaning a Carbon layer's partial successful role on the control of the NPs release.

SEM micrographs of a TaCaP_Zn2C sample after 14 days of immersion and the corrosion tests (Figure 17) show the existence of some Zn particles still in this sample's surface. Such fact can explain why this sample presents diffusional behavior on the EIS results

from 2 hours until 14 days of immersion (Figure 9 B), unlike all the other analyzed samples.

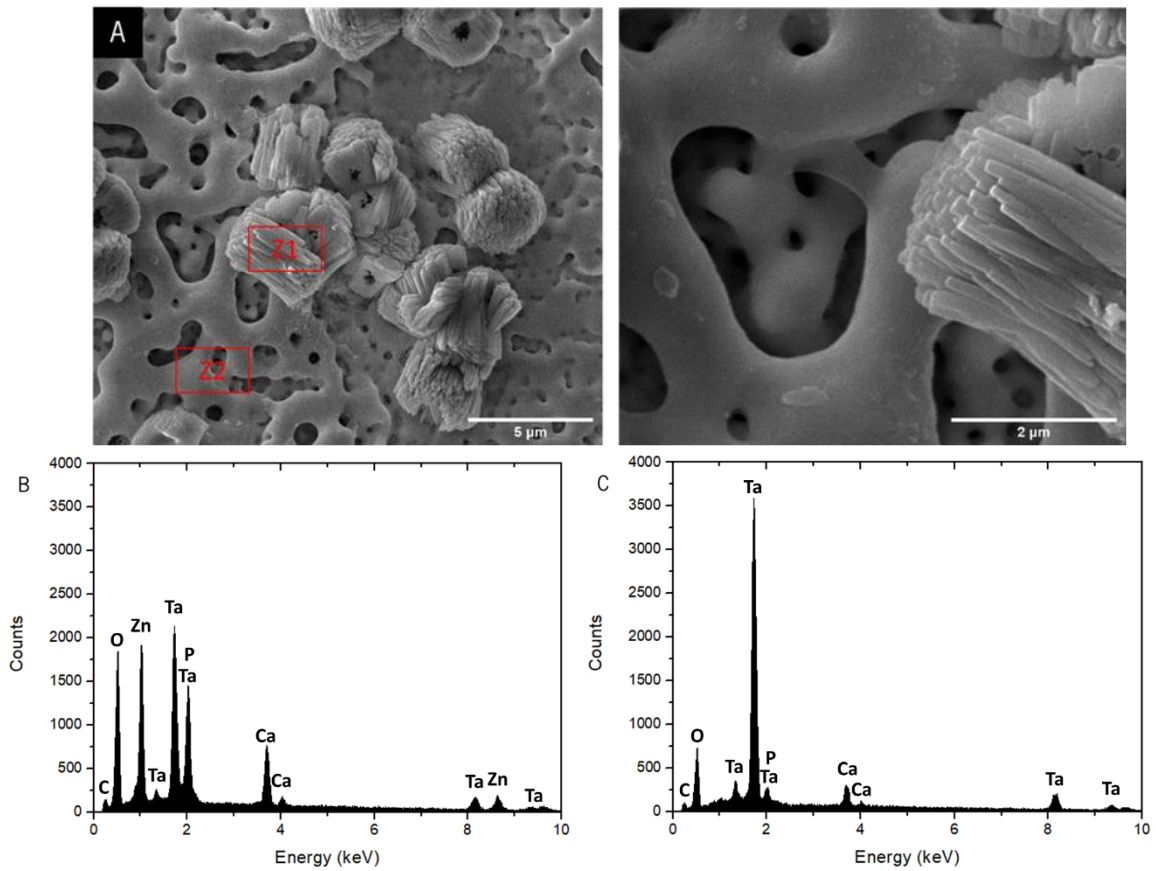


Figure 14 - A) SEM micrographs of TaCaP_Zn2 sample after the potentiodynamic test immediately after immersion (scale: 5 μm on the left and 2 μm on the right), and EDS spectra of B) Z1 and C) Z2.

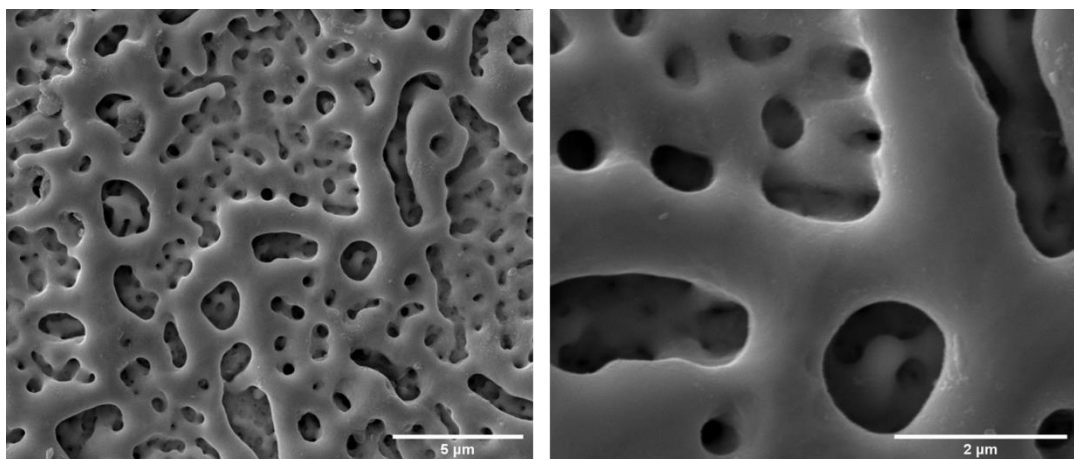


Figure 15 - SEM micrographs of TaCaP_Zn2 sample after the potentiodynamic, OCP and EIS tests 14 days after immersion (scale: 5 μm on the left and 2 μm on the right).

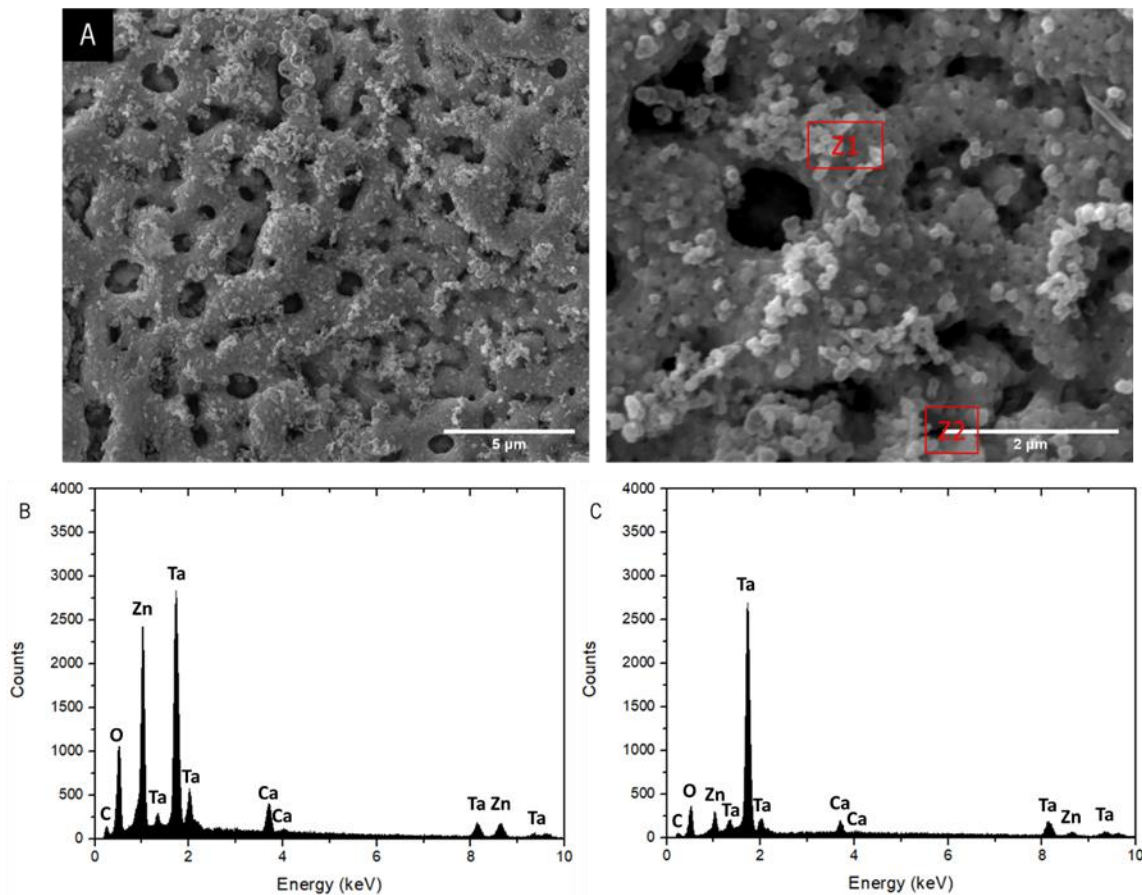


Figure 16 - A) SEM micrographs of TaCaP_Zn2C sample after the potentiodynamic test immediately after immersion (scale: 5 μm on the left and 2 μm on the right), and EDS spectra of B) Z1 and C) Z2.

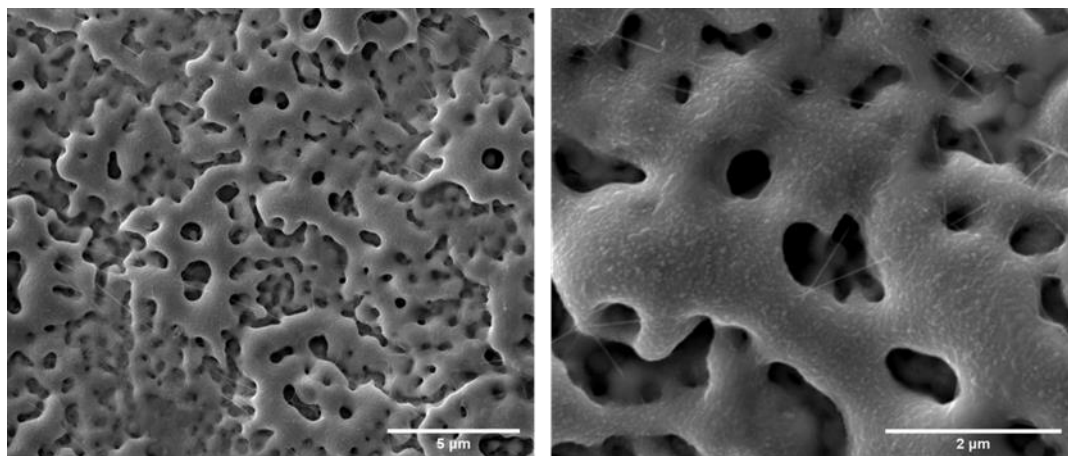


Figure 17 - SEM micrographs of TaCaP_Zn2C sample after the potentiodynamic, OCP and EIS tests 14 days after immersion (scale: 5 μm on the left and 2 μm on the right).

IV – CONCLUSIONS

In this study, different amount of Zn NPs, with and without a thin C layer, were deposited onto micro/nano-porous Ta surfaces, to develop antimicrobial surfaces to be used as biomaterial for

dental implants. The micro/nano-porous Ta surfaces were produced by PEO, performed on high-purity Ta sheets. The Zn NPs were deposited, by magnetron sputtering, onto the porous Ta surfaces, with two different sets of deposition conditions being used to achieve surfaces with different Zn NPs' quantities, and

consequently morphologies and sizes. Posteriorly, a thin C layer was deposited over the two samples, by magnetron sputtering. The samples were characterized by morphological, chemical, and functional techniques, to assess their morphological and chemical properties, as well as their corrosion performances.

PEO technique was proven to be successful, since the morphological and chemical characterization of the developed samples proved the existence of porous structures and incorporation of osteoconductive elements (Ca and P) onto their surfaces. Thus, the PEO allowed the development of surfaces morphological and chemically similar to the human bone. The magnetron sputtering technique, performed under two different deposition conditions, allowed the deposition of Zn NPs in different contents, sizes and morphologies, as it was proven by morphological characterization. ICP-OES technique gave a quantitative characterization of the sputtered samples in terms of Zn²⁺ ions release.

ICP-OES results from both Zn-containing samples covered or not by the C layer showed that the C layer influenced the quantity of Zn²⁺ ions released from the samples, since it acts as barrier layer inhibiting the ions release, comparing with the equivalent sample without C layer.

Corrosion tests demonstrated that, generally, PEO technique positively influenced the corrosion behavior of the anodized samples, due to the formation of the oxide layer. On the other hand, the addition of Zn NPs negatively influenced the corrosion behavior of the studied samples, since the NPs are electrochemical active metallic elements. However, the results also demonstrated the tendency for the Zn-containing and Zn-containing and C layered samples to improve their corrosion response as the immersion time in artificial saliva increased, with their behavior becoming similar to the one demonstrated by the PEO-treated Ta surface.

As future work, the study of the mechanical properties, such as elastic modulus and fracture strength, of the developed samples would be important to guarantee the mechanical resistance of these surfaces. Although the corrosion behavior had already been accessed in this work, the study of the surfaces' tribocorrosion, using a chewing simulation system to simulate the

chewing process with different pH corrosive environments, would also be a good way to better understand the potential of usage of the developed surfaces' modifications on actual dental implants.

ACKNOWLEDGEMENTS

REFERENCES

- [1] S. Pires, "Incorporação de Ca, P e Mg em óxido de Ta nanoestruturado para acelerar a osteointegração em implantes dentários," dissertação apresentada à Universidade do Minho para obtenção do grau de Mestre em Engenharia de Materiais, 2016.
- [2] P. L. Casado, R. R. Guerra, M. A. Da Fonseca, L. C. Costa, J. M. Granjeiro, and E. P. Barboza, "Tratamento das doenças peri-implantares: Experiências passadas e perspectivas futuras - Uma revisão da literatura," *Braz J Periodontol*, vol. 21, no. 02, pp. 25–35, 2011.
- [3] A. Rokn, H. Aslroosta, S. Akbari, H. Najafi, F. Zayeri, and K. Hashemi, "Prevalence of peri-implantitis in patients not participating in well-designed supportive periodontal treatments: a cross-sectional study," *Clin. Oral Implants Res.*, vol. 28, no. 3, pp. 314–319, 2017.
- [4] J. Oliveira, "Deposition of Zn-ZnO nanoparticles by magnetron sputtering onto tantalum substrates," dissertação apresentada à Universidade do Minho para obtenção do grau de Mestre em Engenharia de Materiais, 2017.
- [5] C. F. Almeida Alves, S. V. Calderón, D. Dias, and S. Carvalho, "Influence of Oxygen content on the electrochemical behavior of Ta_{1-x}O_x coatings," *Electrochim. Acta*, vol. 211, pp. 385–394, 2016.
- [6] C. F. Almeida Alves, A. Cavaleiro, and S. Carvalho, "Bioactivity response of Ta_{1-x}O_x coatings deposited by reactive DC magnetron sputtering," *Mater. Sci. Eng. C*, vol. 58, pp. 110–118, 2016.
- [7] S. A. Alves, "A new concept of bio-multifunctional nanotubular surfaces for dental implants: tribocorrosion resistant, antibacterial and osteogenic," tese apresentada à Universidade do Minho para obtenção do grau de Doutora em Engenharia Biomédica, 2017.

- [8] G. Manivasagam, D. Dhinasekaran, and A. Rajamanickam, "Biomedical Implants: Corrosion and its Prevention - A Review," *Recent Patents Corros. Sci.*, vol. 2, no. 1, pp. 40–54, 2010.
- [9] S. Virtanen, I. Milošev, E. Gomez-Barrena, R. Trebše, J. Salo, and Y. T. Kontinen, "Special modes of corrosion under physiological and simulated physiological conditions," *Acta Biomater.*, vol. 4, no. 3, pp. 468–476, 2008.
- [10] J. C. M. Souza *et al.*, "How do titanium and Ti6Al4V corrode in fluoridated medium as found in the oral cavity? An in vitro study," *Mater. Sci. Eng. C*, vol. 47, pp. 384–393, 2015.
- [11] M. A. Khan, R. L. Williams, and D. F. Williams, "The corrosion behaviour of Ti-6Al-4V, Ti-6Al-7Nb and Ti-13Nb-13Zr in protein solutions," *Biomaterials*, vol. 20, no. 7, pp. 631–637, 1999.
- [12] R. Menini, M.-J. Dion, S. K. V. So, M. Gauthier, and L.-P. Lefebvre, "Surface and Corrosion Electrochemical Characterization of Titanium Foams for Implant Applications," *J. Electrochem. Soc.*, vol. 153, no. 1, p. B13, 2006.
- [13] F. Oliveira, "Biofunctionalization of titanium surfaces for dental implants: osteogenic, anti-microbial and tribocorrosion resistant surfaces," tese apresentada à Universidade do Minho para obtenção do grau de Doutor em Engenharia Biomédica, 2015.
- [14] R. Bai *et al.*, "Metallic antibacterial surface treatments of dental and orthopedic materials," *Materials (Basel)*, vol. 13, no. 20, pp. 1–21, 2020.
- [15] A. Sirelkhatim *et al.*, "Review on zinc oxide nanoparticles: Antibacterial activity and toxicity mechanism," *Nano-Micro Lett.*, vol. 7, no. 3, pp. 219–242, 2015.
- [16] V. K. Balla, S. Bodhak, S. Bose, and A. Bandyopadhyay, "Porous tantalum structures for bone implants: Fabrication, mechanical and in vitro biological properties," *Acta Biomater.*, vol. 6, no. 8, pp. 3349–3359, 2010.
- [17] L. Fialho, C. F. Almeida Alves, L. S. Marques, and S. Carvalho, "Development of stacked porous tantalum oxide layers by anodization," *Appl. Surf. Sci.*, vol. 511, no. August 2019, p. 145542, 2020.
- [18] V. K. Balla *et al.*, "Tantalum - A Bioactive Metal for Implants," *JOM*, vol. 62, no. 7, pp. 61–64, 2010.
- [19] C. J. Frandsen, K. S. Brammer, K. Noh, G. Johnston, and S. Jin, "Tantalum coating on TiO₂ nanotubes induces superior rate of matrix mineralization and osteofunctionality in human osteoblasts," *Mater. Sci. Eng. C*, vol. 37, no. 1, pp. 332–341, 2014.
- [20] S. A. Alves *et al.*, "Tribo-electrochemical behavior of bio-functionalized TiO₂ nanotubes in artificial saliva: Understanding of degradation mechanisms," *Wear*, vol. 384–385, no. February, pp. 28–42, 2017.
- [21] L. Fialho, L. Grenho, M. H. Fernandes, and S. Carvalho, "Porous tantalum oxide with osteoconductive elements and antibacterial core-shell nanoparticles: a new generation of materials for dental implants," *Mater. Sci. Eng. C*, vol. 120, no. December 2020, p. 111761, 2020.
- [22] M. Sowa and W. Simka, "Electrochemical impedance and polarization corrosion studies of tantalum surface modified by DC Plasma electrolytic oxidation," *Materials (Basel)*, vol. 11, no. 4, 2018.
- [23] W. T. Huo, L. Z. Zhao, S. Yu, Z. T. Yu, P. X. Zhang, and Y. S. Zhang, "Significantly enhanced osteoblast response to nano-grained pure tantalum," *Sci. Rep.*, vol. 7, pp. 1–13, 2017.
- [24] A. C. Alves, I. Sendão, E. Ariza, F. Toptan, P. Ponthiaux, and A. M. P. Pinto, "Corrosion behaviour of porous Ti intended for biomedical applications," *J. Porous Mater.*, vol. 23, no. 5, pp. 1261–1268, 2016.
- [25] A. C. Alves *et al.*, "Corrosion mechanisms in titanium oxide-based films produced by anodic treatment," *Electrochim. Acta*, vol. 234, pp. 16–27, 2017.

Table 2 - EIS fitting parameters after 2 hours of immersion.

Designation	Ta	TaCaP	TaCaP_Zn1	TaCaP_Zn1C
RSol ($\Omega \cdot \text{cm}^2$)	120 ± 2	122 ± 1	125 ± 3	126 ± 4
R1 ($M\Omega \cdot \text{cm}^2$)	10.5 ± 4.4	8.3 ± 4.4	0.6 ± 0.4	0.7 ± 0.2
Q1 ($\text{nF}/s\alpha \cdot \text{cm}^2$)	17 ± 1	132 ± 37	86 ± 5	93 ± 3
α	0.96 ± 0.00	0.96 ± 0.02	0.97 ± 0.01	0.97 ± 0.00
R2 ($G\Omega \cdot \text{cm}^2$)	-	1.02 ± 0.18	0.0005 ± 0.0001	0.0008 ± 0.0003
Q2 ($\text{nF}/s\alpha \cdot \text{cm}^2$)	-	22 ± 9	-	-
α_2	-	0.71 ± 0.03	-	-
W ($M\Omega \cdot \text{cm}^2/s-0.5$)	-	-	0.26 ± 0.12	0.13 ± 0.05
$< \chi^2 \times 10^{-4}$	1.54	1.47	8.56	9.16
Rp ($M\Omega \cdot \text{cm}^2$)	10.5	1028.3	1.1	1.5

Table 3 - EIS fitting parameters after 24 hours of immersion.

Designation	Ta	TaCaP	TaCaP_Zn1	TaCaP_Zn1C	TaCaP_Zn2	TaCaP_Zn2C
RSol ($\Omega \cdot \text{cm}^2$)	105 ± 3	103 ± 2	100 ± 5	113 ± 4	109 ± 2	105 ± 9
R1 ($M\Omega \cdot \text{cm}^2$)	12.2 ± 1.9	3.9 ± 2.4	0.9 ± 0.3	0.6 ± 0.4	0.2 ± 0.1	0.2 ± 0.1
Q1 ($\text{nF}/s\alpha \cdot \text{cm}^2$)	18 ± 1	138 ± 29	95 ± 11	85 ± 4	92 ± 4	93 ± 6
α	0.96 ± 0.00	0.95 ± 0.01	0.97 ± 0.01	0.98 ± 0.00	0.97 ± 0.01	0.98 ± 0.01
R2 ($G\Omega \cdot \text{cm}^2$)	-	1.30 ± 0.54	0.028 ± 0.001	0.023 ± 0.014	0.003 ± 0.001	1.00 ± 1.00
Q2 ($\text{nF}/s\alpha \cdot \text{cm}^2$)	-	79 ± 16	-	170 ± 84	-	-
α_2	-	0.69 ± 0.02	-	0.66 ± 0.15	-	-
W ($M\Omega \cdot \text{cm}^2/s-0.5$)	-	-	10.71 ± 7.45	-	5.29 ± 5.25	4.10 ± 3.56
$< \chi^2 \times 10^{-4}$	2.57	1.09	5.49	4.03	8.25	22.8
Rp ($M\Omega \cdot \text{cm}^2$)	12.2	1303.9	28.9	23.6	3.2	1000.2

Table 4 - EIS fitting parameters after 48 hours of immersion.

Designation	Ta	TaCaP	TaCaP_Zn1	TaCaP_Zn1C	TaCaP_Zn2	TaCaP_Zn2C
RSol ($\Omega^*\text{cm}^2$)	98 ± 2	85 ± 1	85 ± 6	98 ± 4	63 ± 27	89 ± 11
R1 ($M\Omega^*\text{cm}^2$)	25.5 ± 3.6	4.4 ± 2.1	0.8 ± 0.3	0.8 ± 0.4	0.2 ± 0.2	0.6 ± 0.4
Q1 ($\text{nF}/s\alpha^*\text{cm}^2$)	18 ± 1	139 ± 27	90 ± 9	86 ± 4	70 ± 20	92 ± 5
α	0.96 ± 0.01	0.95 ± 0.01	0.97 ± 0.01	0.98 ± 0.00	0.81 ± 0.17	0.97 ± 0.01
R2 ($G\Omega^*\text{cm}^2$)	-	1.81 ± 0.12	0.11 ± 0.05	0.057 ± 0.002	0.014 ± 0.002	0.014 ± 0.008
Q2 ($\text{nF}/s\alpha^*\text{cm}^2$)	-	73 ± 9	-	141 ± 53	115 ± 46	-
α_2	-	0.69 ± 0.00	-	0.72 ± 0.13	0.89 ± 0.11	-
W ($M\Omega^*\text{cm}^2/\text{s}^{-0.5}$)	-	-	-	-	-	14.11 ± 6.92
$< \chi^2 \times 10^{-4}$	2.75	1.67	1.26	1.65	5.40	7.67
Rp ($M\Omega^*\text{cm}^2$)	25.5	1814.4	110.8	57.8	14.2	14.6

Table 5 - EIS fitting parameters after 7 days of immersion.

Designation	Ta	TaCaP	TaCaP_Zn1	TaCaP_Zn1C	TaCaP_Zn2	TaCaP_Zn2C
RSol ($\Omega^*\text{cm}^2$)	86 ± 4	68 ± 1	101 ± 20	71 ± 12	73 ± 4	78 ± 9
R1 ($M\Omega^*\text{cm}^2$)	36.7 ± 3.9	11.1 ± 0.1	2.0 ± 0.7	1.3 ± 0.2	1.6 ± 1.2	0.8 ± 0.5
Q1 ($\text{nF}/s\alpha^*\text{cm}^2$)	16 ± 1	127 ± 31	88 ± 7	86 ± 3	87 ± 3	88 ± 3
α	0.95 ± 0.00	0.96 ± 0.02	0.97 ± 0.01	0.98 ± 0.00	0.98 ± 0.01	0.97 ± 0.00
R2 ($G\Omega^*\text{cm}^2$)	-	14.96 ± 4.23	0.54 ± 0.40	0.49 ± 0.08	0.004 ± 0.001	0.056 ± 0.025
Q2 ($\text{nF}/s\alpha^*\text{cm}^2$)	-	37 ± 15	59 ± 11	120 ± 39	109 ± 60	-
α_2	-	0.64 ± 0.06	0.68 ± 0.06	0.78 ± 0.07	0.86 ± 0.10	-
W ($M\Omega^*\text{cm}^2/\text{s}^{-0.5}$)	-	-	-	-	-	16.37 ± 7.88
$< \chi^2 \times 10^{-4}$	2.29	6.10	0.57	1.24	5.83	9.66
Rp ($M\Omega^*\text{cm}^2$)	36.7	14971.1	542.0	491.3	5.6	56.8

Table 6 - EIS fitting parameters after 14 days of immersion.

Designation	Ta	TaCaP	TaCaP_Zn1	TaCaP_Zn1C	TaCaP_Zn2	TaCaP_Zn2C
RSol ($\Omega^*\text{cm}^2$)	114 ± 2	114 ± 2	92 ± 18	68 ± 8	113 ± 5	62 ± 11
R1 ($M\Omega^*\text{cm}^2$)	16.6 ± 2.0	11.4 ± 1.1	0.7 ± 0.7	1.3 ± 0.5	0.7 ± 0.1	0.9 ± 0.5
Q1 ($\text{nF}/s\alpha^*\text{cm}^2$)	16 ± 1	127 ± 33	81 ± 2	87 ± 4	84 ± 1	88 ± 2
α	0.95 ± 0.00	0.96 ± 0.02	0.98 ± 0.00	0.98 ± 0.00	0.98 ± 0.00	0.97 ± 0.00
R2 ($G\Omega^*\text{cm}^2$)	-	18.70 ± 0.87	1.44 ± 0.36	1.74 ± 0.87	0.32 ± 0.27	0.14 ± 0.07
Q2 ($\text{nF}/s\alpha^*\text{cm}^2$)	-	28 ± 10	53 ± 9	103 ± 43	86 ± 44	-
α_2	-	0.62 ± 0.02	0.70 ± 0.03	0.80 ± 0.06	0.74 ± 0.09	-
W ($M\Omega^*\text{cm}^2/\text{s}^{-0.5}$)	-	-	-	-	-	20.10 ± 9.96
$< \chi^2 \times 10^{-4}$	3.40	0.78	1.27	1.27	1.05	13.3
Rp ($M\Omega^*\text{cm}^2$)	16.6	18711.4	1440.7	1741.3	320.7	140.9